Wind turbine blade damage detection using aerodynamic noise

Zhang, Y.

DOI
10.4233/uuid:a45acef5-5ef9-4797-be5e-08498566ec8a

Publication date
2024

Document Version
Final published version

Citation (APA)
Zhang, Y. (2024). *Wind turbine blade damage detection using aerodynamic noise*. [Dissertation (TU Delft), Delft University of Technology]. https://doi.org/10.4233/uuid:a45acef5-5ef9-4797-be5e-08498566ec8a

Wind Turbine Blade Damage Detection Using Aerodynamic Noise

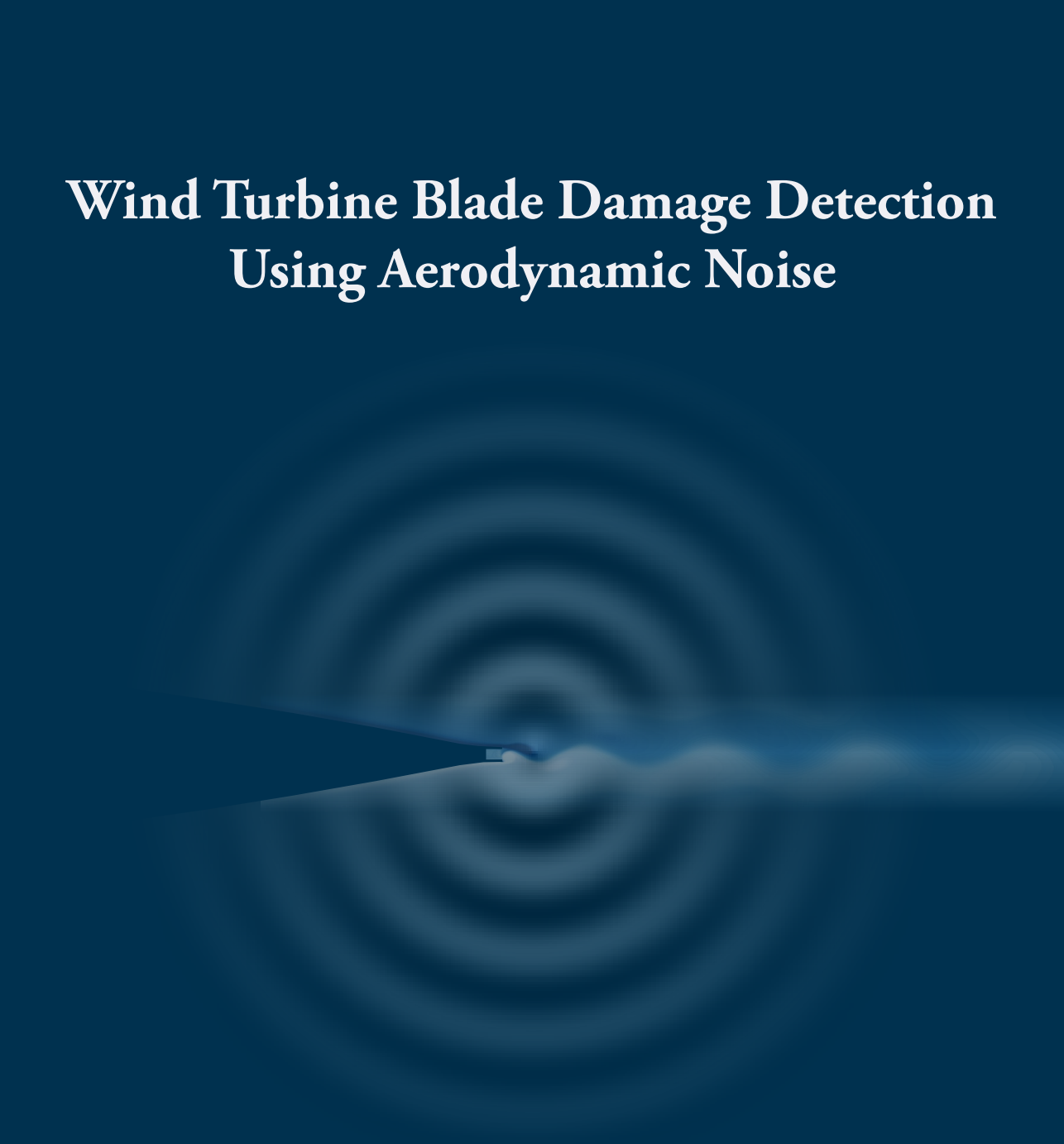

Yanan Zhang

Propositions

accompanying the dissertation

WIND TURBINE BLADE DAMAGE DETECTION USING AERODYNAMIC NOISE

by

Yanan ZHANG

1. A blade trailing edge crack leads to an increase in trailing edge thickness producing a tonal component in the noise spectrum. (Chapter 3)
2. The boundary layer and velocity field around the blade vary in the presence of a turbulent inflow; the prediction of blade damage using aerodynamic noise requires prior knowledge of turbulence properties. (Chapters 4 & 5)
3. Leading edge erosion leads to a reduction in the middle to high-frequency range of the noise spectrum. (Chapter 5)
4. A physical phenomenon is inherently neutral, neither good nor bad; its evaluation is based on human necessities: wind turbine noise is annoying but the information from the noise can be used for wind turbine blade condition monitoring. (This thesis)
5. Individuals are like particles in a flow field; they experience fluctuations and uncertainties in life, however, the general paths and final destinations of their lives are determined by the mainstream of societal development.
6. The principles behind complex things are usually summarized in very simple forms; the philosophy of life is to find fundamental principles from complex phenomena and use them to guide our lives.
7. Education is not only about transferring knowledge and skills but, more importantly, it is about inspiring oneself to discover the meaning of life and one's value to society.
8. Setting and accomplishing staged goals for a long-term task can avoid crying on the last night before the final deadline.
9. Humans are extremely small in the face of natural forces, as a small virus can catch us off guard. We can never dominate nature; the only endeavor we can make is to understand and follow the decree of nature, which is the goal of science.
10. Human intelligence should be used more directly to create a better life rather than to invent trickery or weapons causing conflicts or wars.

These propositions are regarded as opposable and defendable, and have been approved as such by the promotors prof. dr. S. J. Watson and prof. dr. F. Avallone.

Stellingen

behorende bij het proefschrift

WIND TURBINE BLADE DAMAGE DETECTION USING AERODYNAMIC NOISE

door

Yanan ZHANG

1. Een scheur in de trailing-edge van een blad leidt tot een toename in de dikte hiervan, wat een tonale component in het geluidsspectrum veroorzaakt. (Hoofdstuk 3)
2. De grenslaag en het snelheidsveld rond het blad variëren in aanwezigheid van een turbulente instroom; de voorspelling van schade met behulp van aerodynamisch geluid vereist voorkennis van turbulentie-eigenschappen. (Hoofdstuk 4 & 5)
3. Erosie van de leading-edge leidt tot een vermindering van het midden- tot hoogfrequente bereik van het geluidsspectrum. (Hoofdstuk 5)
4. Een fysisch fenomeen is inherent neutraal, noch goed noch slecht; de evaluatie ervan is gebaseerd op menselijke behoeften: windturbinegeluid is hinderlijk, maar de informatie uit het geluid kan gebruikt worden voor het monitoren van de conditie van de bladen. (Dit proefschrift)
5. Individuen zijn als deeltjes in een stromingsveld; ze ervaren fluctuaties en onzekerheden in het leven, maar de algemene paden en eindbestemmingen van hun leven worden bepaald door de hoofdstroom van maatschappelijke ontwikkelingen.
6. De principes achter complexe zaken worden meestal op een eenvoudige manier samengevat; de filosofie van het leven is om fundamentele principes te vinden in complexe verschijnselen en deze te gebruiken om ons leven te sturen.
7. Onderwijs gaat niet alleen over het overdragen van kennis en vaardigheden, maar, nog belangrijker, het gaat erom jezelf te inspireren om de zin van het leven en je waarde voor de samenleving te ontdekken.
8. Het stellen en bereiken van gefaseerde doelen in een groot project kan voorkomen dat er gehuild wordt op de laatste avond voor de uiteindelijke deadline.
9. Mensen zijn extreem klein tegenover natuurkrachten, zoals een klein virus ons kan overrompelen. We kunnen de natuur nooit overheersen; het enige dat we kunnen doen is te proberen de wetten van de natuur te begrijpen en te volgen, wat het doel is van de wetenschap.
10. Menselijke intelligentie zou directer gebruikt moeten worden om een beter leven te creëren in plaats van misleidingen te verzinnen of wapens uit te vinden die conflicten of oorlogen veroorzaken.

Deze stellingen worden opponeerbaar en verdedigbaar geacht en zijn als zodanig goedgekeurd door de promotoren prof. dr. S. J. Watson en prof. dr. F. Avallone.

WIND TURBINE BLADE DAMAGE DETECTION USING AERODYNAMIC NOISE

WIND TURBINE BLADE DAMAGE DETECTION USING AERODYNAMIC NOISE

Proefschrift

ter verkrijging van de graad van doctor
aan de Technische Universiteit Delft,
op gezag van de Rector Magnificus prof. dr. ir. T.H.J.J van der Hagen,
voorzitter van het College voor Promoties,
in het openbaar te verdedigen op woensdag 03 april 2024 om 17:30 uur

door

Yanan ZHANG

Master of Science in Marine Mechanical and Electrical Equipment,
Ocean University of China, Qingdao, China,
geboren te Shandong, China.

Dit proefschrift is goedgekeurd door de

Promotor: prof. dr. S.J. Watson
Promotor: prof. dr. F. Avallone

Samenstelling promotiecommissie:

Rector Magnificus	voorzitter
Prof. dr. S. J. Watson	Technische Universiteit Delft, promotor
Prof. dr. F. Avallone	Politecnico di Torino, Italië, promotor
Onafhankelijke leden:	
Prof. dr. ir. M. Snellen	Technische Universiteit Delft
Prof. dr. A. Fischer	Universität Bremen, Duitsland
Prof. dr. E. Chatzi	ETH Zürich, Zwitserland
Dr. D. Ragni	Technische Universiteit Delft
Prof. dr. M. Kotsonis	Technische Universiteit Delft, reservelid

Keywords: Wind turbine blade damage, aerodynamic noise, trailing edge crack, leading edge erosion, damage detection
Printed by: Ipskamp Printing | https://www.ipskampprinting.nl/
Front & Back: Illustrations of aerodynamic noise generation for a damaged airfoil with trailing edge crack and leading edge erosion
Cover designed by Y. Zhang

ISBN 978-94-6384-556-4

An electronic version of this dissertation is available at
http://repository.tudelft.nl/.

Instead of waiting for the wind,
better to chase where it may come.

CONTENTS

SUMMARY

Wind energy is one of the most important renewable energy sources, effectively addressing climate change issues and promoting sustainable development on a global scale. Blade failures may cause long shut-down times and may present a safety hazard. Continuous and real-time monitoring of the blade conditions is helpful for finding blade damage at an early stage and for predicting its development. Non-contact damage detection methods have the advantage of easy and flexible installation and deployment, especially for current in-service wind turbines, where the blade structures do not need to be modified for installing sensors on or inside the blade.

This thesis aims to investigate and develop a new non-contact method for wind turbine blade damage detection based on measurements of aerodynamic noise. The principle of the proposed method relies on the fact that damage to the blade may modify the boundary layer over the blade surface and the flow field around the blade, and, as a consequence, alter the noise generated aerodynamically. This noise should propagate into the far-field and if measured by microphones could provide a remote way to detect blade damage.

The research on this damage detection method is presented in this thesis as a proof of concept, so the investigations are performed in a controlled environment in the anechoic wind tunnel (A-tunnel) of Delft University of Technology. Two types of damage, trailing edge crack and leading edge erosion, are focused on in this thesis. In order to mimic the turbulent flow environments as in a real wind farm, two turbulence-generating grids are designed to provide turbulent inflows at intensities of 4.0% and 7.1% and integral length scales of 7.9 mm and 10.2 mm respectively. The noise measurements are carried out using a microphone array. With the help of beamforming and source power integration techniques, the noise scattered from the trailing edge or leading edge is identified.

For the trailing edge crack detection, a NACA 0018 airfoil is tested with four configurations of trailing edge cracks. The crack is designed as a rectangular gap at the trailing edge, which leads to increasing the total trailing edge thickness. The experiment is conducted at different inflow velocities and angles of attack. The spectral differences in sound pressure level between the damaged cases and the baseline (without any damage) are compared. The experimental results show that for the clean or low turbulence intensity conditions ($I = 4.0\%$), the relative sound pressure level, ΔL_p, peaks at trailing-edge-thickness-based Strouhal number,St_h, approximatively equal to 0.1. When the inflow turbulence intensity increases to $\sim 4.0\%$, the amplitudes of the relative sound pressure levels to the baseline decrease. Furthermore, when the turbulence intensity of the inflow increases to $\sim 7.1\%$, the spectral differences between the damaged cases and the baseline case disappear. This suggests that the inflow turbulence may have a negative effect on the trailing edge crack detection and the proposed method may not be valid for high turbulence inflow conditions. When the angle of attack increases, the amplitudes of the

relative pressure level also decrease but the inflow velocity does not affect significantly the amplitudes of the relative pressure level.

Regarding the frequency of the crack-induced tones, as the damage level increases, the peak shifts to a higher St_h. Also, compared with the same configuration with the clean inflow, the tone shifts to a higher frequency as the turbulent inflow is present. It was suggested in the previous studies that the frequency of the tone induced by a blunt trailing edge depends on the ratio of the trailing edge thickness, h, and the average boundary layer displacement thickness of the pressure and suction sides, $\bar{\delta}^*$, i.e., $h/\bar{\delta}^*$. Therefore, it is motivated to look into the boundary layer properties and their subsequent effect on the vortex shedding from the damaged trailing edge thus the crack-induced tone. For this purpose, the measurements of the velocity fields near the trailing edge and in the near wake are performed using the particle image velocimetry (PIV) technique. Proper orthogonal decomposition (POD) of the velocity fields is performed to identify the contribution of the coherent vortex structures that are associated with tones observed in the trailing edge noise spectra. The experimental results indicate that the velocity gradient near the wall region at the trailing edge location increases as the size of the crack increases, both for clean and turbulent conditions. This determines stronger coherent vortices shedding with respect to the baseline configuration with consequent louder tonal noise at higher frequencies. It is confirmed that the normalized frequencies of the tones induced by the crack still agree with the tonal prediction model proposed by Brooks, Pope and Marcolini. For a turbulent condition, the length scale of the coherent vortex structures shed from the trailing edge slightly decreases with respect to the clean inflow case, with a consistent increase in the frequency of the tonal component. This suggests that when using this prediction model to estimate the crack size or trailing edge thickness, the impact of the turbulent inflow cannot be neglected.

For the leading-edge erosion detection, a DU96 W180 airfoil with different eroded leading edges is investigated. The leading edge erosion features are scaled from the erosion damage of real blades. In the absence of inflow turbulence, because of the low Reynolds number at which the experiments are carried out, the case with minor erosion severity shows similar far-field noise spectra as the clean leading-edge cases, i.e., the presence of tonal peaks caused by laminar boundary layer instability noise through a self-sustained feedback loop but with higher tonal amplitudes. Increasing the damage level (considered as moderate erosion), the spectra of the noise scattered from the suction side show that the tonal peaks shift to higher frequencies and have lower amplitudes, thus suggesting that the damage alters the flow features responsible for the acoustic feedback loop; whereas, the spectra from the pressure side show a broadband noise distribution. For heavy erosion, the far-field noise spectra show broadband features from both airfoil sides, thus suggesting that the damage has fully forced the transition to turbulent flow; in which case, an increase in the low-frequency content is observed. Conversely, in the presence of turbulent inflow, when comparing the noise scattered at the trailing edge, no difference is found. However, leading edge impingement noise decreases at medium-high frequency compared with the baseline case at a chord-length-based Strouhal number, $St_C \sim 10$. The experimental results also suggest that the delamination feature is the one that is the most easily detectable and the approach is valid for a wide range of angles of attack and inflow velocity.

In conclusion, this thesis presents that the aeroacoustics-based method may be one of the promising ways for wind turbine blade damage detection. It should be noted that the study of this thesis is performed with 2-D airfoil models in controlled wind tunnel environments. However, for an application in the real world, further investigations regarding the engineering aspects, for example, the validations for rotational systems and real wind turbines, are still necessary to be carried out in the future.

SAMENVATTING

Windenergie is een van de belangrijkste hernieuwbare energiebronnen, die de problemen van klimaatverandering effectief aanpakt en duurzame ontwikkeling op wereldschaal bevordert. Defecten van turbinebladen kunnen echter stilstand veroorzaken en een veiligheidsrisico vormen. Continue en realtime bewaking van de toestand van het blad kan gebruikt worden om schade aan het blad in een vroeg stadium op te sporen en de ontwikkeling ervan te voorspellen. Contactloze schadedetectiemethoden hebben het voordeel dat ze gemakkelijk en flexibel te installeren en in te zetten zijn, vooral voor windturbines die al in bedrijf zijn, zonder dat de de bladconstructie aangepast hoeft te worden of sensoren op of in het blad hoeven te worden geïnstalleerd.

Dit proefschrift onderzoekt en ontwikkelt een nieuwe contactloze methode voor de detectie van schade aan bladen van windturbines, gebaseerd op metingen van aerodynamisch geluid. Het principe van de voorgestelde methode is gebaseerd op het feit dat schade aan het blad de grenslaag over het bladoppervlak en het stromingsveld rond het blad kan veranderen, en als gevolg daarvan ook het aerodynamisch gegenereerde geluid. Als dit geluid zich voortplant door de lucht en daarna gemeten wordt met microfoons, voorziet dit mogelijk in een manier om op afstand schade aan het blad detecteren.

Het onderzoek naar deze schadedetectiemethode wordt in dit proefschrift gepresenteerd als een proof of concept, en is daarom uitgevoerd in een gecontroleerde omgeving in de anechoïsche windtunnel (A-tunnel) van de Technische Universiteit Delft. In dit proefschrift ligt de nadruk op twee soorten schade, namelijk scheuren in de trailing-edge en erosie van de leading-edge. Om de turbulente stromingscondities na te bootsen zoals in een echt windmolenpark, zijn twee turbulentie-genererende roosters ontworpen om turbulente instromingen te leveren met intensiteiten van 4,0% en 7,1% en geïntegreerde lengteschalen van respectievelijk 7,9 mm en 10,2 mm. De geluidsmetingen worden uitgevoerd met behulp van een microfoonarray. Met behulp van beamforming en technieken om het vermogen van geluidsbronnen te integreren wordt het verstrooide geluid van de trailing-edge of leading-edge geïdentificeerd.

Voor de detectie van scheuren in de trailing-edge wordt een NACA 0018 vleugelprofiel getest met vier configuraties van scheur. De scheur is ontworpen als een rechthoekige opening aan de trailing-edge, waardoor de totale dikte van de trailing-edge toeneemt. Het experiment wordt uitgevoerd bij verschillende instroomsnelheden en invalshoeken. De spectrale verschillen in de geluidsdruk tussen de beschadigde gevallen en de onbeschadigde worden vergeleken. De experimentele resultaten tonen aan dat voor de schone of lage turbulentie condities ($I = 4,0\%$), de relatieve geluidsdruk, ΔL_p, piekt bij een Strouhal-getal, gebaseerd op de dikte van de trailing-edge, St_h, van ongeveer 0,1. Wanneer de intensiteit van de instroomturbulentie toeneemt tot 4,0%, nemen de amplitudes van geluidsruk van de beschadigde bladen ten opzichte van de onbeschadigde af. Wanneer de turbulentie-intensiteit van de instroom toeneemt tot 7,1%, verdwijnen de spectrale verschillen tussen de beschadigde gevallen en het basisgeval.

Dit suggereert dat de turbulentie van de instroom een negatief effect kan hebben op de detectie van scheuren in de trailing-edge en dat de voorgestelde methode niet geldig is voor instroomcondities met hoge turbulentie. Wanneer de invalshoek toeneemt, nemen de amplitudes van de relatieve geluidsdruk ook af, maar de instroomsnelheid heeft geen significante invloed op de amplitudes van het relatieve drukniveau.

Wat betreft de frequentie van de door scheurvorming geïnduceerde tonen, verschuift de piek naar een hogere St_h naarmate het schadeniveau toeneemt. Ook verschuift de toon, in vergelijking met dezelfde configuratie met schone instroming, naar een hogere frequentie naarmate de turbulentie-intensiteit van instroom toeneemt. In eerdere studies is gesuggereerd dat de frequentie van de toon veroorzaakt door een stompe trailing-edge afhangt van de verhouding tussen de dikte van de achterkant, h, en de gemiddelde dikte van de grenslaagverplaatsing aan de beide zijden van het vleugelprofiel, $h/\bar{\delta}^*$. Daarom is het nodig om te kijken naar de eigenschappen van de grenslaag en het daaropvolgende effect op de afscheiding van wervels aan de beschadigde trailing-edge, dus de door de scheur veroorzaakte toon. Voor dit doel worden metingen van de snelheidsvelden nabij de trailing-edge en in het nabije zog uitgevoerd met door middel van PIV (Particle Image Velocimetry). Proper Orthogonal Decomposition (POD) van de snelheidsvelden wordt uitgevoerd om de bijdrage van de coherente vortexstructuren te identificeren die geassocieerd kunnen worden met de tonen die waargenomen worden in de geluidsspectra van de trailing-edge. De experimentele resultaten geven aan dat de snelheidsgradiënt nabij de wand op de plaats van de trailing-edge toeneemt naarmate de scheur groter wordt, zowel voor schone als turbulente omstandigheden. Dit leidt tot sterker samenhangende wervels ten opzichte van de onbeschadigde configuratie, met als gevolg een luider tonaal geluid bij hogere frequenties. Dit bevestigt dat de genormaliseerde frequenties van de tonen die door de scheur worden geïnduceerd nog steeds overeenkomen met het tonale model dat is voorgesteld door Brooks, Pope en Marcolini. Voor een turbulente situatie neemt de lengteschaal van de coherente wervelstructuren die van de achterrand afkomen iets af ten opzichte van het geval met een schone instroom, met een consistente toename in de frequentie van de tonale component. Dit suggereert dat bij het gebruik van dit model voor het schatten van de scheurwijdte of de dikte van de trailing-edge, de invloed van de turbulente instroming niet kan worden verwaarloosd.

Voor de detectie van erosie van de leading-edge is een DU96 W180-airfoil met verschillende geërodeerde voorranden onderzocht. De erosie-eigenschappen zijn geschaald op met de erosieschade van echte bladen. In de afwezigheid van instroomturbulentie, vanwege het lage Reynoldsgetal waarbij de experimenten worden uitgevoerd, vertoont het geval met lichte erosie dezelfde geluidspectra als de gevallen zonder erosie, d.w.z. de aanwezigheid van tonale pieken veroorzaakt door een laminaire grenslaaginstabiliteit als gevolg van een terugkoppelingslus, maar met hogere tonale amplitudes. Als het schadeniveau toeneemt (beschouwd als matige erosie), laten de spectra van het geluid dat verspreid wordt vanaf de lage-druk zijde (bovenrug) zien dat de tonale pieken verschuiven naar hogere frequenties en een lagere amplitude hebben, wat suggereert dat de schade de stromingseigenschappen verandert die verantwoordelijk zijn voor de akoestische terugkoppelingslus; tegelijkertijd laten de spectra van de hoge-druk zijde (onderrug) een breedbandige geluidsdistributie zien. Voor zware erosie vertonen

de geluidspectra breedbandige kenmerken van beide zijden van het vleugelprofiel, wat suggereert dat de schade een volledige overgang naar een turbulente stroming heeft geforceerd; hierdoor wordt in dit geval een toename in het laagfrequente gehalte waargenomen. Omgekeerd, met een turbulente instroom, wordt er bij het vergelijken van het verstrooide geluid aan de trailing-edge geen verschil geobserveerd. Het geluid aan de leading-edge veroorzaakt door inkomende wervels neemt echter af bij middelhoge frequentie vergeleken met een onbeschadigd profiel met een op de koordlengte gebaseerd Strouhalgetal, $St_C \sim 10$. De experimentele resultaten suggereren ook dat het delaminatiekenmerk het gemakkelijkst te detecteren is en dat de benadering geldig is voor een groot bereik van invalshoeken en instroomsnelheden.

Concluderend kan in dit proefschrift worden gesteld dat de op aeroakoestiek gebaseerde methode een veelbelovende manier is om schade aan windturbinebladen op te sporen. Opgemerkt moet worden dat het onderzoek in dit proefschrift is uitgevoerd met 2D-modellen in gecontroleerde condities in een windtunnel. Voor een toepassing in de echte wereld zijn verdere onderzoeken met betrekking tot de technische aspecten, bijvoorbeeld de validaties voor rotatiesystemen en echte windturbines, in de toekomst nog steeds noodzakelijk.

PREFACE

When it comes to *noise*, it always seems to bring annoyance. Since Lighthill first proposed acoustic analogy in the 1950s, *aeroacoustics* has become an independent discipline of science. The strategies for mitigation of airflow-induced noise, such as noise generated by aircraft and wind turbines, have been widely proposed and investigated in the past decades. This also, in turn, advanced the development of the theory in noise reduction and the understanding of mechanisms for noise generation in aeroacoustics.

The noise generated from the interaction between the flow and the wind turbine blade can contain abundant information indicating the operational conditions of the blade. Based on this principle, the work of this thesis, drawing on conventional aeroacoustics research methodology, aims to develop and investigate a new non-contact method for blade damage detection based on the measurements of aerodynamic noise.

Since the purpose of this work is for blade damage detection, at the beginning of the thesis (in Chapter 1), the development of wind energy and state-of-the-art techniques for wind turbine blade damage detection and monitoring are reviewed. Afterward, Chapter 2 introduces the fundamentals of aeroacoustics and tools for measurements as well as the detailed experimental setup for this work. Chapters 3, 4, 5 focus on the detection of two types of blade damage, trailing edge crack and leading edge erosion. Not only the noise spectral differences from the healthy blade are present (which is more interesting for readers of the damage detection field), but the mechanisms that lead to the noise changes are analyzed and discussed (which may be more attractive to researchers in aeroacoustics). Finally, the last chapter concludes the key findings and provides some recommendations for future work.

It should be noted that the research of this thesis is still at a very preliminary stage, where not all the associated scopes are fully investigated. However, the author hopes this thesis contributes to advancing the field of wind turbine blade condition monitoring and damage detection and inspires further exploration of aerodynamic noise analysis as a promising tool for new applications in wind energy.

The work of this thesis was supported by the China Scholarship Council (CSC, under Grant 201906330095) and supervised by Prof. dr. Simon Watson and Prof. dr. Francesco Avallone. The author would like to acknowledge the support from all the parties involved.

Enjoy your reading!

Yanan Zhang

Yanan Zhang
Delft, September 2023

1

INTRODUCTION

Wind energy is one of the most important renewable sources. In recent years people have witnessed a boom in the wind energy industry. With the growth of installations of wind turbines, damage detection and condition monitoring of the wind turbine blade are increasingly important and crucial for safe operation and steady power output of a wind farm. However, damage detection for a real wind turbine blade is challenging because of the peculiarities of turbine operation and the blade design. The geometry and surface roughness of a blade may change due to the presence of damage thus affecting the aerodynamics and the consequent noise emission. In this thesis, in order to further advance the non-contact approaches for wind turbine blade damage detection, a new method based on far-field measurements of aerodynamic noise is investigated.

1

1.1. ENERGY AND SOCIETY

All major progress in human society has been accompanied by the drive of the energy technology revolution. In ancient times, the use and control of fire led to early humans achieving unprecedented development and taking a completely different evolutionary path from that of animals. In modern times, the use of steam power pushed humans into the *Age of Stream* (the First Industrial Revolution), in which machine production began to gradually replace manual labor and the productivity of society greatly improved. Later, the invention of electric generators and internal combustion engines further promoted the development of human society, which led to the Second Industrial Revolution. In particular, the use of electricity brought innovations in electrical appliances, lighting, and radio technology; humans entered into the *Age of Electricity*. Now we are experiencing the Third Industrial Revolution, in which the demand for energy is unprecedented. Traditional fossil fuel energy cannot satisfy the development goals of society in cleanliness and sustainability. This means that renewable energy technologies are becoming increasingly important. It is no exaggeration to say that we are now in the *Age of Renewable Energy*.

1.2. DEVELOPMENT OF THE WIND ENERGY INDUSTRY

Wind energy is one of the most important renewable energy sources and plays a crucial role in reducing carbon emissions, mitigating climate change, and advancing the transition towards a more environmentally responsible energy future [1].

More and more wind turbines are being installed onshore and offshore. Figure 1.1 shows cumulative global installed wind power capacity over the years since 2011 according to statistics from the International Renewable Energy Agency (IRENA) [2]. It can be seen that the capacity has increased rapidly, in particularly offshore. By 2022, global wind power capacity reached 9×10^5 MW, of which approximately 7% was from offshore wind turbines. However, this figure was only 2.2×10^5 MW in 2011 with the proportion offshore being 1.7%.

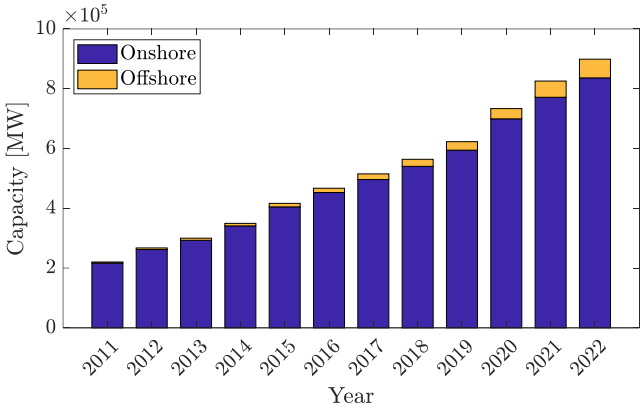

Figure 1.1: Cumulative global wind power capacity by year since 2011. [2].

According to a report from the International Energy Agency (IEA) in 2013 [3], the average rotor diameter of mainstream commercial wind turbines in 2000-2005 was 70 m, which increased to 130 m in 2022 [4]. Average rated capacity increased from 1.5 MW to 5 MW during the period 2000 to 2022. The rotor size will become larger in the future, as shown in Figure 1.2. It is expected to be 174 m for onshore wind turbines and 250 m for offshore machines in 2035 [5].

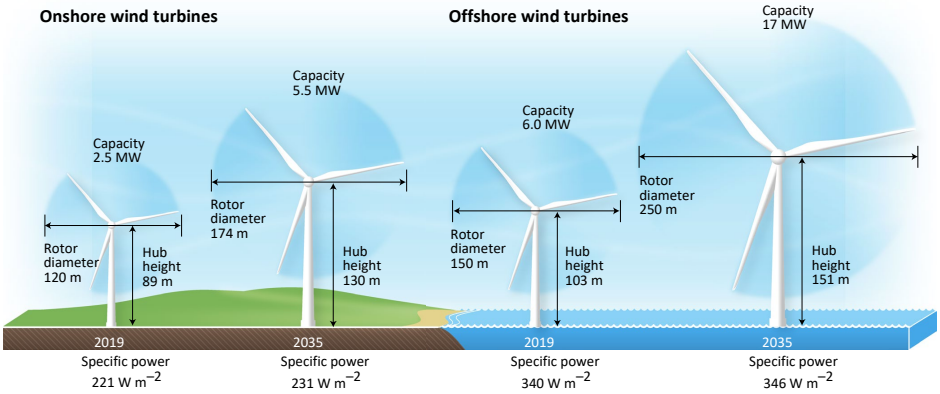

Figure 1.2: Expected average rotor size in 2035 for onshore and offshore wind turbines compared with that in 2019 [5].

1.3. WIND TURBINE BLADE DAMAGE

1.3.1. AN OVERVIEW

With the increase in the scale of the wind energy industry and the size of wind turbines, there is an increasing number of ever longer wind turbine blades. On the one hand, as the number of in-service blades increases, the instances of blade damage or failures increase. On the other hand, a larger, damaged blade may cause more serious accidents and bring more financial loss. This means that blade damage or failures are an increasing concern for the wind energy industry.

Wind turbine blades are particularly susceptible to damage due to a combination of factors. These include the continuous load they endure, the effects of aging, and the direct impact of the challenging operating conditions in which they are working. It was reported that until 2020, there were approximately 700,000 blades in operation globally; on average, 3,800 blades experienced damage or failures each year [6]. Each blade suffered from 0.456 minor repairs (cost below 1,000 EUR), 0.010 major repairs (cost of 1,000 - 10,000 EUR), and 0.001 major replacements per year [7]. The failure rate of an offshore wind turbine blade is about 4 times higher than that of an onshore one [8]. Some reports have indicated that wind turbine blades suffer from damage with a higher probability than other wind turbine components, such as gearboxes and generators [9–11]. For example, according to a survey of over 700 onshore wind turbines in Sweden from 1997 to 2005, wind turbine blades contribute 13.4% of total failures, which is higher than that of

gearboxes (9.8%) or generators (5.5%) [9].

Wind turbine blade damage or failures can lead to significant downtime and therefore a reduction in electrical production during the lifetime of a wind turbine. This consequently brings significant financial loss. Figure 1.3 shows the statistics for the proportion of downtime due to failures of critical components of onshore and offshore wind turbines reported in Reference [8]. Blade and hub damage contributes approximately 20% of the total downtime of a wind turbine, which ranks third after gearbox and generator for both onshore and offshore wind turbines. The failure rate of an offshore wind turbine blade (22.2%) is slightly higher than the onshore one (18.2%).

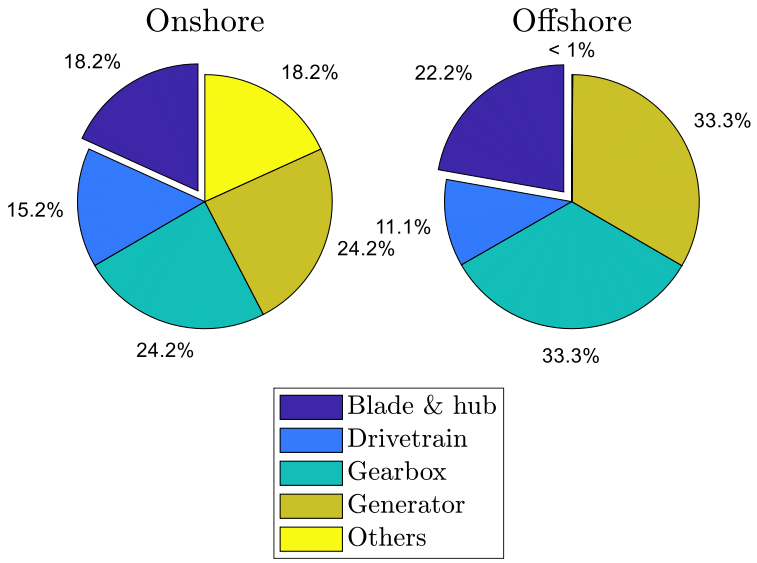

Figure 1.3: The proportion of downtime due to failures of critical components of onshore and offshore wind turbines [8].

The structural repair of a damaged wind turbine blade costs up to 3,000 USD, while a replacement with a new blade may cost on average 20,000 USD [6]. Out-of-service turbines do not produce electricity, which may cause an indirect financial loss of 800 - 1,600 USD per day; most of the repair work takes 1 - 3 days [6]. Figure 1.4 shows two application scenarios for the inspection and repair of wind turbine blades in wind farms.

The above statistics show the importance of continuous and real-time condition monitoring and damage detection for a blade. An ideal condition monitoring system should detect damage or failures at an early stage and track their development over time, making it possible to avoid costly breakdowns and serious accidents [14, 15]. Additionally, monitoring data can be useful to improve maintenance planning, which can reduce unnecessary manual inspections and maintenance costs for a wind farm.

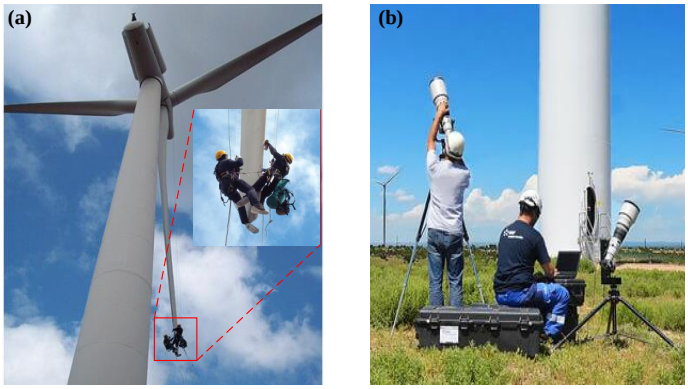

Figure 1.4: Inspection and repair of wind turbines: (a) inspection and repair of the blade surface [12]; (b) visual inspection on the ground [13].

1.3.2. BLADE STRUCTURE AND DAMAGE TYPES

Modern wind turbine blades are usually made of fibre composite structures which can provide the necessary strength and durability for their weight. As shown in Figure 1.5, a wind turbine blade typically consists of a top layer, a bottom layer, supporting web structures (spar) and load-carrying flanges [16]. The top and bottom layers are glued together at the leading edge and trailing edge of the blade. The supporting web structures can withstand longitudinal deformation and the flanges are responsible for resisting the compression loads on the top layer and tension loads on the bottom layer, respectively. The structural configuration of a blade inherently makes it prone to damage at adhesive joints and points with high periodic forces. The structural damage of a blade on the surface and at the supporting spar, as shown in Figure 1.6, is categorized into a few types in Reference [16].

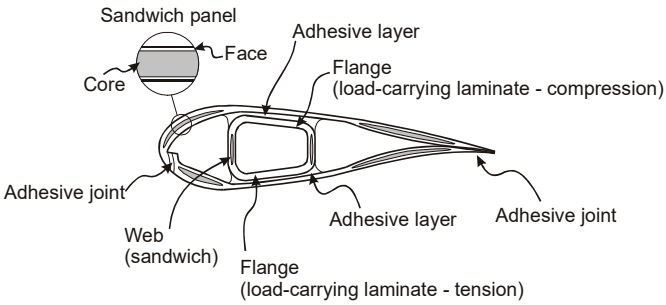

Figure 1.5: The composite structure of a wind turbine blade [16].

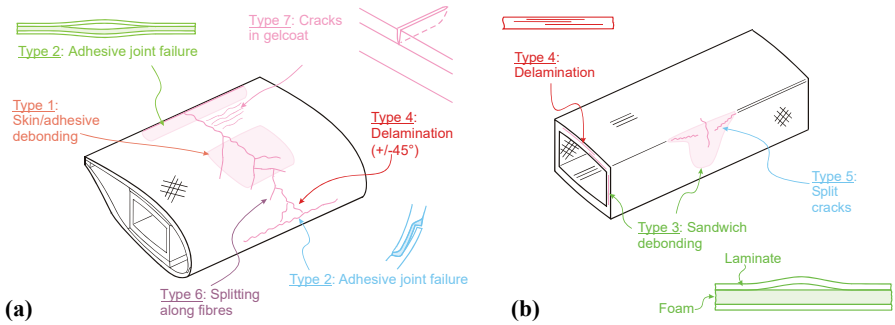

Figure 1.6: The damage types of a wind turbine blade: (a) on the skin or surface and (b) at the main supporting spar [16].

1.3.3. LEADING EDGE DAMAGE

The adhesive joints between the top and bottom layers are typically vulnerable to the impact of periodic loads and the effects of aging. Damage can often be found in these locations. Structural adhesive joint failures might occur at the leading edge of a blade, for example, given rise to a leading edge crack, as shown in Figure 1.7(a). The leading edge of a wind turbine blade is the foremost part of the blade facing the incoming flow. Consequently, it suffers from the impingement or impact of airborne hard particles (sand particles) or raindrops during operation. Over time the effects of these seemingly insignificant impacts will accumulate and eventually lead to erosion of the leading edge [17–20], as shown in Figure 1.7(b). Impacts from flying animals such as birds and bats can contribute to leading edge damage [21, 22].

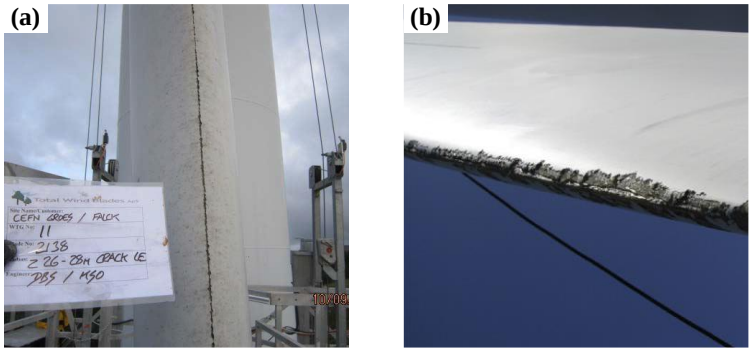

Figure 1.7: Leading edge damage: (a) leading edge crack [23] and (b) leading edge erosion [20].

1.3.4. TRAILING EDGE DAMAGE

Adhesive joint failure can also happen at the trailing edge of the blade. This will consequently lead to a crack at the trailing edge, as shown in Figure 1.8(a) [23]. When the blade operates in an environment with high temperatures, there is a possibility of heightened spanwise stress. This can, in turn, result in deformation occurring at the trailing edge of the blade, as shown in Figure 1.8(b) [24].

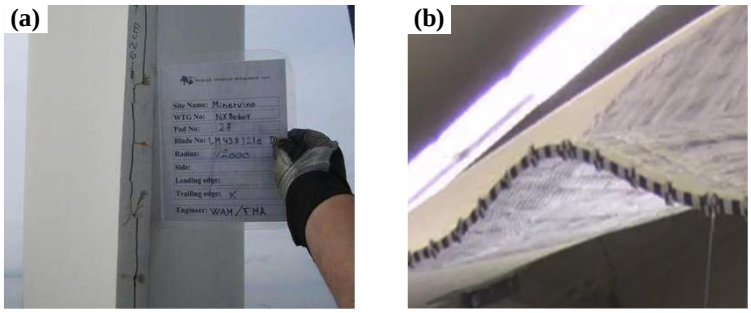

Figure 1.8: Trailing edge damage: (a) trailing edge crack [23] and (b) trailing edge deformation [24].

1.3.5. SURFACE DAMAGE

During the long-term operation of a blade, certain environmental factors, such as temperature variation and UV radiation, may contribute to material wear and aging [25]. This will consequently raise the risk of the presence of surface coating delamination, as shown in Figure 1.9(a) [23]. For some extreme weather conditions, such as lightning, strikes can cause burns and damage on the protective coatings, as shown in Figure 1.9(b) [23]. This can accelerate material degradation if the exposed sections are not dealt with properly [26].

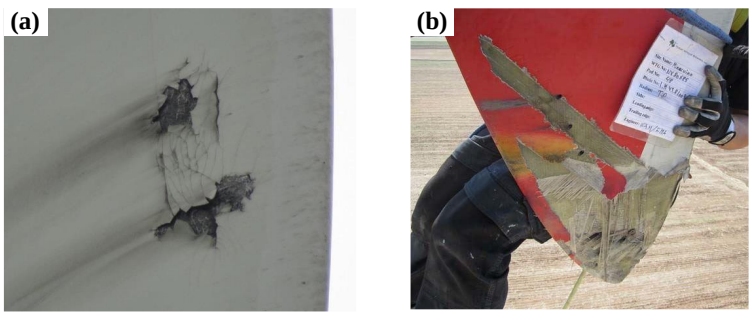

Figure 1.9: Surface damage: (a) surface delamination and (b) lightning damage [23].

1

1.4. BLADE DAMAGE DETECTION TECHNIQUES

The established state-of-the-art blade damage detection techniques can be divided into two categories: contact and non-contact methods. The former relies on the sensors installed on the blades that can measure the signals altered by blade damage. These methods are based on measurements of quantities like structural vibrations, strain or elastic waves (Acoustic Emission, AE). The non-contact methods frequently utilize fixed, often ground-based, remote instruments, such as infrared thermography cameras, laser scanners or microphones. Sensors can also be carried on Unmanned Aerial Vehicles (UAVs, like drones) for inspections in wind farms [27, 28].

1.4.1. CONTACT METHODS

VIBRATION MEASUREMENT

Vibration measurement is one of the most common damage detection methods, and has been widely used for the health monitoring of mechanical components [29–31] and structures [32–35]. The vibration-based approach relies on measurements from displacement sensors, velocity sensors or accelerometers [36]. When damage is present in a blade, structural parameters, for example, damping and stiffness, might change. As a result, the response signal to the external excitation will change correspondingly. By analyzing the spectral or modal properties of the response signal, damage detection can be achieved. In principle, vibration-based analysis has been demonstrated for blade health monitoring [37, 38] showing that it is possible to find the locations of failure by using multiple sensors.

However, there are still some key technical limitations that need to be overcome. For example, installing and integrating vibration sensors into in-service wind turbines might be tricky and costly. Furthermore, since wind turbine blades are made of fiberglass composite material with a high damping coefficient, vibrations may be absorbed by the material attenuating the signal. This means that only those sensors located near damaged regions might work effectively for the detection of damage, which suggests that the layout of the sensors needs to be carefully determined. Figure 1.10 shows a vibration measurement system for blade health monitoring mounted on an in-service wind turbine.

Figure 1.10: A vibration measurement system for blade health monitoring [39].

STRAIN MEASUREMENT

Strain gauges are commonly used to measure the deformation or strain in materials when they are subjected to external forces or loads. This deformation provides valuable information about the stress that the material is experiencing, which, in turn, can offer insights into the health condition of the material. The use of strain gauges can provide an economically feasible solution for wind turbine blade condition monitoring [40–42]. Conventional strain gauges, for example, those made of copper, need to be calibrated frequently, which might limit their applications for long-term monitoring of wind turbine blades. In recent years, a new way to measure the strain has been developed by using optical Fibre Bragg Grating (FBG) sensors. FBG sensors can convert strain variables into optical wavelength parameters [43, 44]. The usage of FBG sensors overcomes the disadvantage of frequent calibration requirements but the establishment of the monitoring system on a blade is still expensive.

ACOUSTIC EMISSION

When external loads act on the material, the local deformation position of the material rapidly releases energy in the form of elastic waves. The frequency of the elastic waves is usually in the ultrasonic range, which cannot be measured by microphones sensitive to the audible sound range. The setup for an acoustic-emission-based approach requires special high-frequency acoustic transducers on the surface of the material [45, 46]. Acoustic emission elastic waves are essentially vibration waves in the material. The energy of such high frequency acoustic waves dissipates rapidly during propagation in the material. Therefore, the locations of transducers require careful consideration for a damage detection system. Figure 1.11 shows an acoustic emission detection system for wind turbine blade failures.

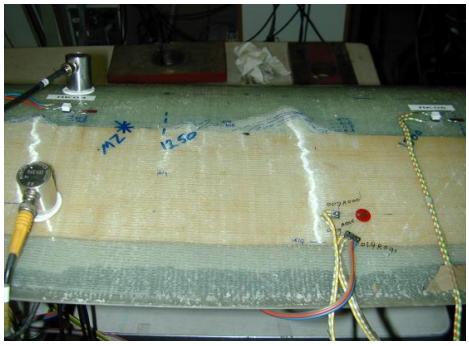

Figure 1.11: An acoustic emission detection system of wind turbine blade damage[47].

1.4.2. NON-CONTACT METHODS

INFRARED THERMOGRAPHY CAMERAS

Damage to a blade may change thermal properties at the damaged location, therefore changing its heat transfer properties. When applied to wind turbine blade damage detection, this involves the use of an infrared camera to capture thermal images of the

blades [48–50]. The captured thermal images are analyzed using image processing and analysis techniques [51, 52]. The damaged parts of the blade appear as regions with different temperatures compared to the surrounding areas making it possible to identify the potential damage locations. The use of infrared thermography cameras can provide a remote and portable method for wind turbine blade damage detection. However, the effectiveness of an infrared thermography camera for blade damage detection can be influenced by the operating conditions of the wind turbine and the limitation of the camera sensitivity; the temperature differences caused by damage might not easily be identified when damage is at a very early stage. Figure 1.12 shows an example of damage detection based on an infrared thermography cameras for a wind turbine blade.

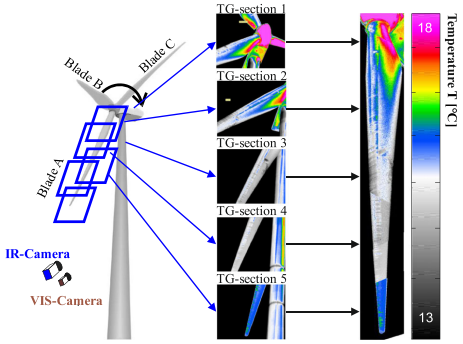

Figure 1.12: An example of blade damage detection based on infrared thermography cameras [52].

LASER SCANNERS

A laser scanner emits laser beams in the direction of a wind turbine blade and the reflection of the beam is measured by a camera. As the laser scanner moves, it can capture cloud data from surface reflection at different scanning points, and then a 3-D blade geometry can be created [53, 54]. The acquired 3-D model can be compared with a reference blade model without any damage. Variations in surface normals, curvature, and other geometric properties between the scanned model and the reference model can indicate potential damage. The laser-scanner-based approach offers several advantages, such as non-contact measurement and high precision in capturing complex geometries [55]. However, high-quality laser scanning equipment is still rather expensive.

MICROPHONES

In recent years, blade monitoring approaches based on audible sound measurements have been developed. They can be divided into two types: active and passive methods. The former places audio speakers inside the blade structure and microphones are used to measure the sound emitted in the far-field [56, 57], as shown in Figure 1.13(a). This approach relies on the fact that the sound from the speakers can pass more easily through the damaged location (crack, hole or defect) of the blade and the emitted sound will be louder than if no damage were present. By using a microphone array on

the ground and beamforming technique [58, 59], the damaged location can be identified. The latter (passive method) relies on measurements of the acoustic response of the blade structural cavities [60–62]. The sound is produced from the interactions between the flow and damage (such as holes, cracks and splits) and then propagates to the microphones in the blade cavities. For this type of method, microphones are usually placed in the blade, as shown in Figure 1.13(b), and there is no need for additional sound sources from speakers.

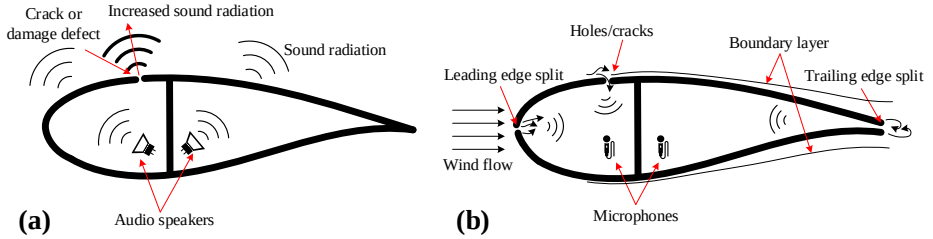

Figure 1.13: Audible-sound-based damage detection for a wind turbine blade: (a) active method [57] and (b) passive method [62].

Apart from the audible sound sources used in the above methods, another sound source, aerodynamic noise [63–66], can also used for blade damage detection. Studies by [67–70] have used data-driven analysis of the measured sound data. The physics behind the generation of the sound measured following damage is not sufficiently investigated in these studies.

1.4.3. CHALLENGES FOR BLADE DAMAGE DETECTION

Previous discussions in this section addressed the importance of damage detection for wind turbine blades and summarized some contact and non-contact methods that are commonly employed in real applications. However, so far there are still many challenges to the development of an accurate, flexible, low-cost and reliable solution. Some key challenges and considerations for real-world applications are briefly summarized as follows:

- **Integration with the blade structure.**

  The sensors for contact methods need to be directly placed on or in the blade structure to ensure accurate measurements of damage-induced variations. For some non-contact methods, sensors are also required to be placed inside the blade cavities. However, how to install and integrate the required sensors in the blade is still a concern, especially for those wind turbines that are already operating. Furthermore, wind turbine blades are directly exposed to harsh environments with a wide range of temperatures, humidity levels and weather conditions [38, 71]. The replacement of broken integrated sensors is rather difficult. This requires careful design of the integration and installation of the damage detection system at the beginning to ensure its reliability and durability.

- **Spatial resolution of detection.**

  Non-contact methods usually use remote measurements with, for example, optical and acoustic sensors. The spatial resolution reduces as the distance between the sensor and the rotor increases. As a consequence, some small damage might be very difficult to identify.

- **Detection of early-stage damage.**

  When damage occurs on a blade at a very early stage, the damage-induced features in the signals are usually not significant, and historical information about the damage is limited. In this case, the sensors used for damage detection might not be sensitive enough to capture minor changes and the identification of damage may be less accurate [72, 73]. As a consequence, this may cause a misjudgment and raise false alarms about the condition of the blade.

- **Long-term and real-time monitoring.**

  A well-established blade damage detection system requires long-term and real-time monitoring of blade conditions to track the occurrence and development of the damage and then provide a prognosis. Continuous monitoring generates a significant amount of data over time, especially for those methods using imaging or sound information. Storing, managing, and processing a large volume of data efficiently can be challenging, especially in remote or offshore locations.

- **Cost of detection**.

  Detection systems normally require advanced high-precision devices with associated data processing systems. Their prices are still rather high, which limits their usage where a low-cost system is required [74, 75]. Furthermore, wind turbine blade damage and failure types are various and one single type of damage detection technique is usually limited in its ability to find all types of damage. Therefore, various techniques need to be used together for a wide range of damage detection and the cost will increase.

Damage detection techniques for a wind turbine blade have seen increasing interest in both academia and industrial applications. However, a universal method that can satisfy all the application scenarios with low cost and high performance is not yet available.

1.5. OBJECTIVES AND STRUCTURE OF THE THESIS

The previous sections highlighted the importance and challenges of wind turbine blade damage detection. To further advance the development of novel non-contact approaches for wind turbine blade damage detection, this thesis investigates a new aeroacoustics-based concept based on far-field aerodynamic noise measurements. As a first stage, a fundamental understanding of the associated physics and mechanisms of aerodynamic noise generation in the presence of damage on a blade is crucial. Based on this focus, this thesis investigates two types of blade damage, trailing edge crack and leading edge erosion based on airfoil models tested in a wind tunnel. The research goals of this thesis are as follows:

1. **To identify the spectral differences in sound generated by a damaged blade and by a healthy one.**

2. **To investigate the physics of the change in blade noise in the presence of damage.**

3. **To investigate how the operating conditions, such as inflow turbulence, velocity, and angle of attack, affect the noise spectra and damage detection.**

4. **To determine the aerodynamic and aeroacoustic parameters that can be used for damage prediction.**

The thesis is structured as follows and a brief illustration of the framework of this thesis is shown in Figure 1.14:

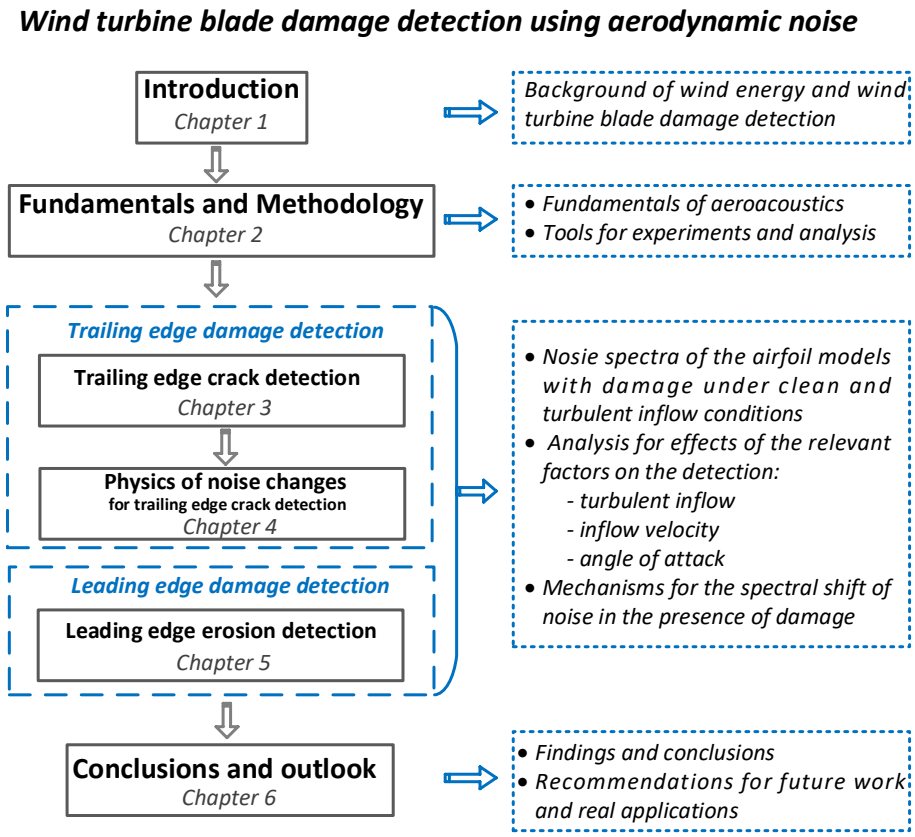

Figure 1.14: Framework of this thesis.

- **Chapter 1** has introduced the background to wind energy development and the state-of-the-art techniques for wind turbine blade damage detection. The importance and the challenges of wind turbine blade damage detection were also discussed in this chapter. At the end of the chapter, the research objectives and the structure of the thesis are presented.

- **Chapter 2** provides the fundamentals of aeroacoustics and the experimental and analytical tools used in this thesis. The first part of this chapter explains the mechanisms of sound generation for different aerodynamic noise sources. It also outlines the theory of conventional frequency domain beamforming and the associated source power integration and background subtraction algorithms. The second part of the chapter presents the detailed experimental setup and design of the facilities and test airfoil models. The characterizations of the flow and background noise levels are also reported.

- **Chapter 3** investigates how a trailing edge crack affects the trailing edge noise spectrum for different clean and turbulent inflow conditions; the effects of the inflow velocity and angle of attack on the trailing edge crack detection are also discussed.

- **Chapter 4** further investigates the impact of the trailing edge crack and inflow turbulence on the boundary layer properties at the trailing edge and the consequent effects on the coherent vortex shedding and tones in trailing edge noise; a comparison between the measured results and the current prediction models is reported and usability and limitations of the prediction models for damage detection are also discussed in this chapter.

- **Chapter 5** describes the work to detect leading edge erosion. In this chapter, the spectral differences between the damaged cases and the baseline case (without any damage) are compared both for leading edge noise and trailing edge noise. The physical mechanism that leads to the change in the noise spectra is explored. Similarly to the trailing edge crack detection, the effects of the operational conditions, such as inflow turbulence, velocity, and airfoil angle of attack on damage detection are investigated.

- Finally, **Chapter 6** summarizes the main findings and conclusions of this thesis. Some brief recommendations for the next step in research and application in a real wind farm are also provided at the end of this chapter.

REFERENCES

[1] "Paris agreement". In: *Report of the Conference of the Parties to the United Nations Framework Convention on Climate Change (21st Session, 2015: Paris). Retrived December*. Vol. 4. HeinOnline. 2015, p. 2017.

[2] International Renewable Energy Agency (IRENA). Wind energy. *IRENA.org* (2023).

[3] F. Gagliardi. Wind energy technology roadmap. *International Energy Agency (IEA)* (2013), 1–58.

[4] Office of Energy Efficiency & Renewable Energy (US). Wind Turbines: the Bigger, the Better. *Energy.gov* (2023).

[5] R. Wiser, J. Rand, J. Seel, et al. Expert elicitation survey predicts 37% to 49% declines in wind energy costs by 2050. *Nature Energy* **6** (2021), 555–565.

[6] L. Mishnaevsky and K. Thomsen. Costs of repair of wind turbine blades: Influence of technology aspects. *Wind Energy* **23** (2020), 2247–2255.

[7] J. Carroll, A. McDonald, and D. McMillan. Failure rate, repair time and unscheduled O&M cost analysis of offshore wind turbines. *Wind Energy* **19** (2016), 1107–1119.

[8] C. Dao, B. Kazemtabrizi, and C. Crabtree. Wind turbine reliability data review and impacts on levelised cost of energy. *Wind Energy* **22** (2019), 1848–1871.

[9] J. Ribrant and L. Bertling. Survey of failures in wind power systems with focus on Swedish wind power plants during 1997-2005. *2007 IEEE Power Engineering Society General Meeting, PES* (2007), 1–8.

[10] B. Hahn and M. Durstewitz. Reliability of wind turbines - Experiences of 15 years with 1500 WTs. *EUROMECH Colloquium 464b: Wind Energy* (2005).

[11] W. Yang, Z. Peng, K. Wei, and W. Tian. Structural health monitoring of composite wind turbine blades: Challenges, issues and potential solutions. *IET Renewable Power Generation* **11** (2017), 411–416.

[12] G. Marsh. Meeting the challenge of wind turbine blade repair. *Reinforced Plastics* **55** (2011), 32–36.

[13] Dmiyares. Webinar: Blade Maintenance: Observations from the Field and Practical Solutions (2016).

[14] M. A. S. Shohag, E. C. Hammel, D. O. Olawale, and O. I. Okoli. Damage mitigation techniques in wind turbine blades: A review. *Wind Engineering* **41** (2017), 185–210.

[15] X. Pan, Z. Liu, R. Xu, et al. Early warning of damaged wind turbine blades using spatial–temporal spectral analysis of acoustic emission signals. *Journal of Sound and Vibration* **537** (2022), 117209.

[16] B. F. Sørensen, E. Jørgensen, C. Debel, et al. *Improved design of large wind turbine blades of fibre composites (Phase 1) - Summary Report*. Tech. rep. 2004, pp. 1–36.

[17] W. Han, J. Kim, and B. Kim. Effects of contamination and erosion at the leading edge of blade tip airfoils on the annual energy production of wind turbines. *Renewable Energy* **115** (2018), 817–823.

[18] A. Sareen, C. A. Sapre, and M. S. Selig. Effects of leading edge erosion on wind turbine blade performance. *Wind Energy* **17** (2014), 1531–1542.

[19] H. M. Slot, E. R. Gelinck, C. Rentrop, and E. Van der Heide. Leading edge erosion of coated wind turbine blades: Review of coating life models. *Renewable Energy* **80** (2015), 837–848.

[20] M. H. Keegan, D. H. Nash, and M. M. Stack. On erosion issues associated with the leading edge of wind turbine blades. *Journal of Physics D: Applied Physics* **46** (2013).

[21] P. M. Cryan, P. M. Gorresen, B. R. Straw, S. Thao, and E. Degeorge. Influencing activity of bats by dimly lighting wind turbine surfaces with ultraviolet light. *Animals* **12** (2022), 1–23.

[22] A. S. Verma, J. Yan, W. Hu, et al. A review of impact loads on composite wind turbine blades: Impact threats and classification. *Renewable and Sustainable Energy Reviews* **178** (2023), 113261.

[23] A. Branner Kim; Ghadirian. *Database about blade faults*. Tech. rep. 2014, pp. 8–13.

[24] P. U. Haselbach and K. Branner. Initiation of trailing edge failure in full-scale wind turbine blade test. *Engineering Fracture Mechanics* **162** (2016), 136–154.

[25] J. S. Chou, C. K. Chiu, I. K. Huang, and K. N. Chi. Failure analysis of wind turbine blade under critical wind loads. *Engineering Failure Analysis* **27** (2013), 99–118.

[26] T. Naka, N. J. Vasa, S. Yokoyama, et al. Study on Lightning Protection Methods for Wind Turbine Blades. *IEEJ Transactions on Power and Energy* **125** (2005), 993–999.

[27] Y. Wang, R. Yoshihashi, R. Kawakami, et al. Unsupervised anomaly detection with compact deep features for wind turbine blade images taken by a drone. *IPSJ Transactions on Computer Vision and Applications* **11** (2019), 0–6.

[28] C. Galleguillos, A. Zorrilla, A. Jimenez, et al. Thermographic non-destructive inspection of wind turbine blades using unmanned aerial systems. *Plastics, Rubber and Composites* **44** (2015), 98–103.

[29] H. G. Chen, Y. J. Yan, and J. S. Jiang. Vibration-based damage detection in composite wingbox structures by HHT. *Mechanical Systems and Signal Processing* **21** (2007), 307–321.

[30] C. Bujoreanu, V. Horga, and B. Drăgan. Vibration analysis methods in bearing damage detection. *Applied Mechanics and Materials* **371** (2013), 622–626.

[31] J. Wodecki, A. Michalak, and R. Zimroz. Local damage detection based on vibration data analysis in the presence of Gaussian and heavy-tailed impulsive noise. *Measurement: Journal of the International Measurement Confederation* **169** (2021), 108400.

[32] H. Hao and Y. Xia. Vibration-based Damage Detection of Structures by Genetic Algorithm. *Journal of Computing in Civil Engineering* **16** (2002), 222–229.

[33] Y. J. Yan, L. Cheng, Z. Y. Wu, and L. H. Yam. Development in vibration-based structural damage detection technique. *Mechanical Systems and Signal Processing* **21** (2007), 2198–2211.

[34] S. Das, P. Saha, and S. K. Patro. Vibration-based damage detection techniques used for health monitoring of structures: a review. *Journal of Civil Structural Health Monitoring* **6** (2016), 477–507.

[35] O. Abdeljaber, O. Avci, S. Kiranyaz, M. Gabbouj, and D. J. Inman. Real-time vibration-based structural damage detection using one-dimensional convolutional neural networks. *Journal of Sound and Vibration* **388** (2017), 154–170.

[36] Y. Du, S. Zhou, X. Jing, et al. Damage detection techniques for wind turbine blades: A review. *Mechanical Systems and Signal Processing* **141** (2020), 106445.

[37] A. Joshuva and V. Sugumaran. A study of various blade fault conditions on a wind turbine using vibration signals through histogram features. *Journal of Engineering Science and Technology* **13** (2018), 102–121.

[38] K. F. Abdulraheem and G. Al-Kindi. A Simplified wind turbine blade crack identification using Experimental Modal Analysis (EMA). *International Journal of Renewable Energy Research* **7** (2017), 715–722.

[39] D. Tcherniak and L. L. Mølgaard. Active vibration-based structural health monitoring system for wind turbine blade: Demonstration on an operating Vestas V27 wind turbine. *Structural Health Monitoring* **16** (2017), 536–550.

[40] K. Papadopoulos, E. Morfiadakis, T. Philippidis, and D. Lekou. Assessment of the strain gauge technique for measurement of wind turbine blade loads. *Wind Energy* **3** (2000), 35–65.

[41] Peter Bjoern Andersen, L. Henriksen, M. Gaunaa, C. Bak, and T. Buhl. Deformable trailing edge fl aps for modern megawatt wind turbine controllers using strain gauge sensors. *Wind Energy* **13** (2010), 193–206.

[42] K. Lee, A. Aihara, G. Puntsagdash, et al. Feasibility study on a strain based deflection monitoring system for wind turbine blades. *Mechanical Systems and Signal Processing* **82** (2017), 117–129.

[43] K. Schroeder, W. Ecke, J. Apitz, E. Lembke, and G. Lenschow. A fibre Bragg grating sensor system monitors operational load in a wind turbine rotor blade. *Measurement Science and Technology* **17** (2006), 1167–1172.

[44] T. Verbruggen. Load monitoring for wind turbines. Fibre optic sensing and data processing. *Wind Energy* (2013).

[45] P. A. Joosse, M. J. Blanch, A. G. Dutton, et al. Acoustic emission monitoring of small wind turbine blades. *Journal of Solar Energy Engineering, Transactions of the ASME* **124** (2002), 446–454.

[46] J. Tang, S. Soua, C. Mares, and T. H. Gan. An experimental study of acoustic emission methodology for in service condition monitoring of wind turbine blades. *Renewable Energy* **99** (2016), 170–179.

[47] W. Yang. Testing and condition monitoring of composite wind turbine blades. *Recent advances in composite materials for wind turbines blades* (2013), 147–169.

[48] A. Manohar, J. Tippmann, and F. Lanza di Scalea. Localization of defects in wind turbine blades and defect depth estimation using infrared thermography. *Sensors and Smart Structures Technologies for Civil, Mechanical, and Aerospace Systems 2012* **8345** (2012), 83451O.

[49] R. Yang, Y. He, A. Mandelis, et al. Induction infrared thermography and thermal-wave-radar analysis for imaging inspection and diagnosis of blade composites. *IEEE Transactions on Industrial Informatics* **14** (2018), 5637–5647.

[50] D. Yang, J. Tang, and F. Zeng. Blade imbalance fault diagnosis of doubly fed wind turbine based on current coordinate transformation. *IEEJ Transactions on Electrical and Electronic Engineering* **14** (2019), 185–191.

[51] A. Manohar and F. Lanza di Scalea. Detection of defects in wind turbine composite blades using statistically enhanced Lock-In Thermography. *Structural Health Monitoring* **12** (2013), 566–574.

[52] M. Doroshtnasir, W. Tamara, K. Rainer, and R. Mathias. On-site inspection of potential defects in wind turbine rotor blades with thermography. *Wind Energy* **19** (2016), 1407–1422.

[53] M. Grosse-Schwiep, J. Piechel, and T. Luhmann. Measurement of rotor blade deformations of wind energy converters with laser scanners. *Journal of Physics: Conference Series* **524** (2014).

[54] A. U. Dilek, A. D. Oguz, F. Satis, Y. D. Gokdel, and M. Ozbek. Condition monitoring of wind turbine blades and tower via an automated laser scanning system. *Engineering Structures* **189** (2019), 25–34.

[55] F. P. García Márquez and A. M. Peco Chacón. A review of non-destructive testing on wind turbines blades. *Renewable Energy* **161** (2020), 998–1010.

[56] K. Aizawa, P. Poozesh, C. Niezrecki, et al. An acoustic-array based structural health monitoring technique for wind turbine blades. *Structural Health Monitoring and Inspection of Advanced Materials, Aerospace, and Civil Infrastructure 2015* **9437** (2015), 94371P.

[57] P. Poozesh, K. Aizawa, C. Niezrecki, et al. Structural health monitoring of wind turbine blades using acoustic microphone array. *Structural Health Monitoring* **16** (2017), 471–485.

[58] P. Sijtsma and M. Snellen. Inverse integration method for distributed sound sources. *BeBeC* (2018), 9–17.

[59] R. Merino-Martínez, P. Sijtsma, A. R. Carpio, et al. Integration methods for distributed sound sources. *International Journal of Aeroacoustics* **18** (2019), 444–469.

[60] C. Traylor, M. DiPaola, D. J. Willis, and M. Inalpolat. A computational investigation of airfoil aeroacoustics for structural health monitoring of wind turbine blades. *Wind Energy* **23** (2020), 795–809.

[61] J. Solimine, C. Niezrecki, and M. Inalpolat. An experimental investigation into passive acoustic damage detection for structural health monitoring of wind turbine blades. *Structural Health Monitoring* **19** (2020), 1711–1725.

[62] C. Beale, M. Inalpolat, and C. Niezrecki. Active acoustic damage detection of structural cavities using internal acoustic excitations. *Structural Health Monitoring* **19** (2020), 48–65.

[63] M. Lighthill. On Sound Generated Aerodynamically . I . General Theory. *Proceedings of the Royal Society of London A, Mathematical and Physical Sciences* **211** (1952), 564–587.

[64] M. Lighthill. On Sound Generated Aerodynamically . II . Turbulence as a Source of Sound. *Proceedings of the Royal Society of London A, Mathematical and Physical Sciences* **222** (1953), 1–32.

[65] N. Curle. The influence of solid boundaries upon aerodynamic sound. *Proceedings of the Royal Society of London. Series A, Mathematical and Physical Sciences* **231** (1955), 505–514.

[66] J. E. Ffowcs Williams and D. L. Hawkings. Sound generation by turbulence and surfaces in arbitrary motion. *Philosophical Transactions of the Royal Society of London. Serie A, Mathematical and Physical Sciences* **264** (1969), 321–342.

[67] B. M. Fazenda and D. Comboni. Acoustic condition monitoring of wind turbines: Tip faults. *9th International Conference on Condition Monitoring and Machinery Failure Prevention Technologies 2012, CM 2012 and MFPT 2012* **1** (2012), 109–123.

[68] B. Chen, S. Yu, Y. Yu, and Y. Zhou. Acoustical damage detection of wind turbine blade using the improved incremental support vector data description. *Renewable Energy* **156** (2020), 548–557.

[69] C. Q. Zhang, Z. Y. Gao, Y. Y. Chen, et al. Locating and tracking sound sources on a horizontal axis wind turbine using a compact microphone array based on beamforming. *Applied Acoustics* **146** (2019), 295–309.

[70] T. H. Tu, F. C. Lo, C. C. Liao, C. F. Chung, and R. C. Chen. Using wind turbine noise to inspect blade damage through portable device. *INTER-NOISE 2019 MADRID - 48th International Congress and Exhibition on Noise Control Engineering* (2019), 1–5.

[71] C. Hochart, G. Fortin, J. Perron, and A. Ilinca. Wind turbine performance under icing conditions. *Wind Energy* **11** (2008), 319–333.

[72] J. Tang, S. Soua, C. Mares, and T. H. Gan. An experimental study of acoustic emission methodology for in service condition monitoring of wind turbine blades. *Renewable Energy* **99** (2016), 170–179.

[73] C. Devriendt, F. Magalhães, W. Weijtjens, et al. Structural health monitoring of offshore wind turbines using automated operational modal analysis. *Structural Health Monitoring* **13** (2014), 644–659.

[74] A. Stetco, F. Dinmohammadi, X. Zhao, et al. Machine learning methods for wind turbine condition monitoring: A review. *Renewable Energy* **133** (2019), 620–635.

[75] F. P. García Márquez, A. M. Tobias, J. M. Pinar Pérez, and M. Papaelias. Condition monitoring of wind turbines: Techniques and methods. *Renewable Energy* **46** (2012), 169–178.

2

FUNDAMENTALS AND METHODOLOGY

The aerodynamic noise scattered from a blade might change as damage is present and thus it can be an indicator for damage detection and condition monitoring. The first section of this chapter presents the fundamentals of aeroacoustics, in which the mechanisms of noise generation present in an airfoil or a wind turbine blade are summarized. In the second section, Conventional Frequency Domain Beamforming (CFDBF) is introduced together with the source power integration technique and background noise subtraction. The third section presents the experimental facilities and setup; the characterizations of inflow turbulence and background noise levels are also reported.

Parts of this chapter have been published in *Applied Acoustics* **191** (2022) [1], *Journal of Physics: Conference Series* **2265** (2022) [2] and *Applied Acoustics* **207** (2023) [3].

2.1. AERODYNAMIC NOISE

Aerodynamic noise is generated from the motion of turbulence in the free field [4, 5] or produced by the interaction between airflow and solid boundaries [6, 7]. For a wind turbine, as the blade is usually working at low Mach numbers, the noise produced by turbulence in the free field is less effective [8, 9]. A lifting surface rotating in airflow may produce loading noise and thickness noise, of which the frequencies are related to the rotating frequency; however, for a large wind turbine, the loading noise and the thickness noise are less important due to the low rotating frequency of the rotor. Therefore, the considered aerodynamic noise of a wind turbine blade mainly results from the interaction of inflow turbulence impinging on the blade or vortices in the boundary layers crossing the trailing edge or tip of the blade (airfoil self-noise).

This section presents several basic noise sources for wind turbine applications. The spectral features and the noise generation mechanisms are explained. Furthermore, at the end of this section, the potential effects of blade damage on the aerodynamic noise changes are briefly discussed.

2.1.1. FUNDAMENTAL MECHANISM

Considering that the length scale of the vortex interacting with an airfoil is Λ and convective velocity is U_c, vortex disturbances happen at a frequency of $f = U_c/\Lambda$; from the acoustic aspect, turbulence noise will be emitted at the same frequency $f = c/\lambda$, where c is sound speed and λ is the wavelength. Depending on the relative size of the vortex to the chord length, C, the turbulence noise at low frequency and high frequency can present different properties.

Low-frequency noise. If the length scale of the vortex is much larger than the chord length, the fluctuating forces caused by the vortex can be considered to act on the airfoil globally. In this case, the sound wavelength of the emitted turbulence noise is also much larger than the chord length, i.e., $C/\lambda \ll 1$, and the airfoil is considered to be acoustically compact, as shown in Figure 2.1. The energy of acoustic pressure is proportional to $\sin^2\theta$ (θ is the sound scattering angle with respect to inflow direction as shown in Figure 2.1) and 6th power of inflow velocity, U, more specifically [6],

$$p'^2 \sim \frac{\rho_0 U^6 C^2}{R^2 c^3} \sin^2\theta \tag{2.1}$$

where ρ_0 is the medium density; R is the distance between the source and the observer. Consequently, the low-frequency noise is scatted as a standard dipole directivity pattern as shown in Figure 2.1.

High-frequency noise. When the length scale of the vortex is comparable to or smaller than the chord length, the vortex only affects the local aerodynamic forces on the airfoil surface. In this case, the sound wavelength of the emitted turbulence noise is smaller than the chord length, i.e., $C/\lambda \gg 1$, where the airfoil is acoustically non-compact. The energy of acoustic pressure changes with a 5th power law of the inflow velocity, U, and is proportional to $\sin^2(\theta/2)$ [7], i.e.,

$$p'^2 \sim \frac{\rho_0 U^5 C\delta}{R^2 c^2} \sin^2\frac{\theta}{2} \tag{2.2}$$

where δ is the characteristic length associated with the length scale of the vortex. The emission directivity of high-frequency noise is of a cardioid pattern as shown in Figure 2.1).

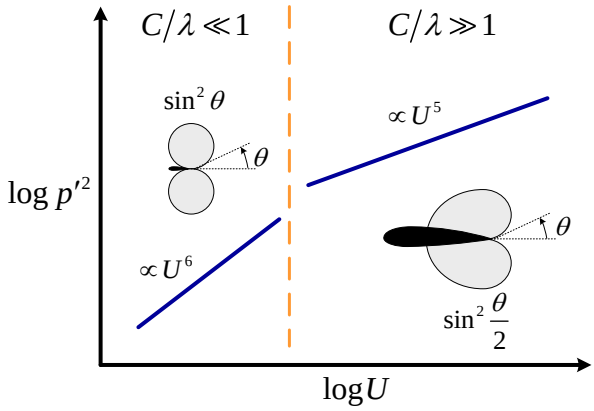

Figure 2.1: Illustration of airfoil turbulence noise and its directivity [6, 7].

2.1.2. INFLOW TURBULENCE LEADING EDGE INTERACTION NOISE

When a wind turbine blade encounters atmospheric turbulence or the wakes shed by upstream turbines, the interaction between the blade and inflow turbulence will produce noise scattered from the airfoil leading edge. This is because inflow turbulence will induce unsteady pressure on the blade surface and the pressure disturbances create an unsteady lift, which consequently provides a source term for noise generation [6]. Theoretical prediction for the leading edge noise assumes the solid body is a thin flat plate and uses a transfer function between the turbulent flow spectrum and the resulting lift fluctuations [10, 11]. Then the unsteady lift is converted to the far-field noise spectrum [6].

The airfoil geometrical properties, such as airfoil thickness and leading edge radius, also affect the leading edge noise. The increase in the thickness and the leading edge radius of an airfoil leads to a significant reduction in acoustic power levels in the high-frequency range. This is because the airfoil with a larger thickness or with a larger leading edge radius will produce a larger stagnation region [12] in front of the leading edge. As a consequence, the magnitudes of the turbulent fluctuations colliding with the airfoil are eventually reduced, which causes a reduction in the unsteady lift of the airfoil and therefore the leading edge noise [12–14].

2.1.3. AIRFOIL SELF-NOISE

LAMINAR BOUNDARY LAYER INSTABILITY NOISE

When at low Reynolds number conditions, such as at the root section of a blade or for small wind turbines, the boundary layer is laminar or transitional. The laminar bound-

ary layer may be separated due to an adverse pressure gradient. The separated shear layer is unstable and undergoes laminar-to-turbulent transition downstream causing the flow reattachment [15]. As a consequence, a separation bubble may be formed near the trailing edge, as shown in Figure 2.2. In this case, the noise scattered from the trailing edge is usually characterized by a spectral hump and a series of tones (harmonics) in the spectrum [16–20]. Figure 2.3(a) shows a typical laminar boundary layer instability noise spectrum of an airfoil. The spectrum is typically composed of a broadband spectral hump with a centered frequency of f_s, and a series of discrete tones with frequencies of f_n. Figure 2.3(b) shows the frequency variations of the spectral hump and the tones as the velocity increases [16]. It was found that the central frequency of the spectral hump is proportional to the 1.5th power of the velocity while the frequencies of tones show a $U^{0.8}$ dependence; as the velocity increases, the tones show a "ladder" distribution [16–20].

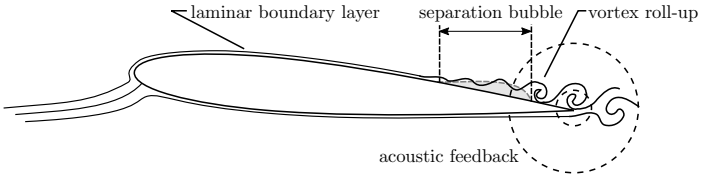

Figure 2.2: Vortex shedding and noise emission for laminar boundary layer instability noise [15, 21].

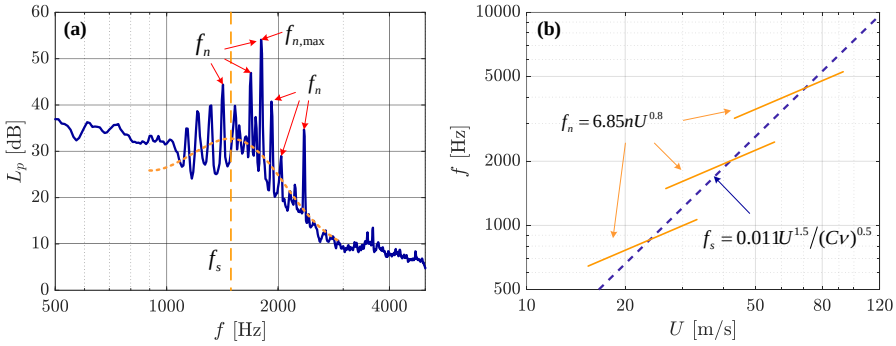

Figure 2.3: Illustrations of laminar boundary layer instability noise: (a) a typical noise spectrum [3]; and (b) the scaling law of frequencies of the tones [16]

Recent studies [15, 20] revealed that the spectral hump is attributed to the amplification effect of the boundary layer separation bubble on the T-S waves and the resulting coherent vortex shedding. The amplified T-S waves lead to a coherent vortex shedding from the trailing thus generating a tonal component as a hump in the spectrum. The presence of discrete tones is ascribed to the acoustic feedback loop mechanism: vor-

tices shed at the trailing edge emit the acoustic waves that travel upstream at a certain distance in the boundary layer and trigger new instabilities; as a consequence, these excited instabilities create new vortices shed from the trailing edge and eventually create new tonal noise; the frequencies of the harmonics can be determined by the total phase change of acoustic waves going around the feedback loop [15, 16, 20]. The "ladder" structure with an increasing velocity is caused by the frequency lag [20] between the hump (proportional to $U^{1.5}$) and the discrete tones (proportional to $U^{0.8}$).

TURBULENT BOUNDARY LAYER TRAILING EDGE NOISE

For current commercial wind turbines, the blades usually work at high Reynolds numbers [8]. The turbulent boundary layer develops on the blade surface and remains attached to the trailing edge. In this case, the vortices with different length scales in the boundary layer produce unsteady pressure fluctuations on the surface and these fluctuations are scattered from the sharp trailing edge, as shown in Figrue 2.4. This will consequently produce broadband content in the far-field noise spectrum. The turbulent boundary layer trailing edge noise is considered to be the most important noise source for a modern commercial wind turbine [8].

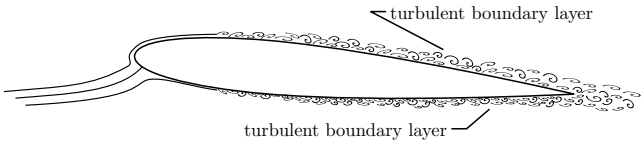

Figure 2.4: Vortex shedding from a sharp trailing edge [21].

Though the turbulent boundary layer trailing edge noise shows broadband spectral features, it has a distinct hump in the spectrum where noise intensity becomes maximum [22, 23]. Experimental studies suggested the spectral hump is located at the boundary-layer-displacement-thickness-based Strouhal number, $St_{\text{peak}} = f_{\text{peak}}\delta^*/U \sim 0.06-0.08$ [22], where f_{peak} is the central frequency of broadband hump, δ^* the boundary layer displacement thickness and U the inflow velocity.

TRAILING EDGE BLUNTNESS VORTEX SHEDDING NOISE

When the flow passes over a blunt body, von Kármán vortex street might occur in the wake. When the trailing edge of the airfoil is 0.3 times thicker than the displacement thickness of the turbulent boundary layer, coherent vortex structures might shed from the trailing edge to the near wake [8], as shown in Figure 2.5. As a result, a tonal component will be observed in the trailing edge noise spectrum [21, 24–26].

From the experimental observations [21], the amplitude and the frequency of the tone rely on the ratio of $h/\bar{\delta}^*$, where h is the trailing edge thickness; $\bar{\delta}^*$ is the averaged displacement thickness between the pressure side and suction side at the trailing edge, i.e., $\bar{\delta}^* = (\delta_s^* + \delta_p^*)/2$. The frequency can be scaled with the trailing-edge-thickness-based Strouhal number, $St_h = fh/U$, where f is the frequency and U is the inflow velocity. The

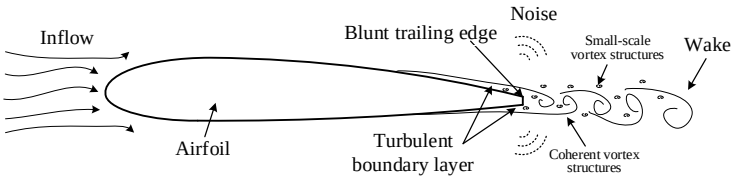

Figure 2.5: Vortex shedding from a blunt trailing edge and the associated tonal noise emission.

nondimensional frequency of the tone, $St_{h,\text{peak}}$, fits with the following empirical model developed by Brooks, Pope and Marcolini (BPM) [21]:

$$St_{h,\text{peak}} = \begin{cases} 0.1\left(h/\bar{\delta}^*\right) + 0.095 - 0.00243\Psi & h/\bar{\delta}^* < 0.2 \\ \dfrac{0.212 - 0.0045\Psi}{1 + 0.235\left(h/\bar{\delta}^*\right)^{-1} - 0.0132\left(h/\bar{\delta}^*\right)^{-2}} & h/\bar{\delta}^* \geq 0.2 \end{cases} \tag{2.3}$$

where Ψ is the solid angle (in degrees), between the sloping surfaces at the trailing edge. As the ratio of $h/\bar{\delta}^*$ increases, the location of the tonal peak, $St_{h,\text{peak}}$, shifts to a higher value.

SEPARATION AND STALL NOISE

When a blade is operating at a high angle of attack, the boundary layer on the suction side might tend to separate from the blade surface caused by the adverse pressure gradient [27–29]. In this case, large-scale vortices will be formed in the boundary layer, as shown in Figure 2.6 (top). As a consequence, these vortices will produce low-frequency noise (separation noise) when they interact with the trailing edge [30, 31].

As the angle of attack increases further over the critical angle of attack, where the coefficient of lift exceeds the maximum and decreases, the separation point of the boundary layer moves forward upstream and the separation region on the suction side becomes more considerable. The vortices will be formed with larger scales, as shown in Figure 2.6 (bottom). As a result, a lower frequency content (stall noise) will be observed in the noise spectrum [30, 32].

TIP NOISE

For a 3D blade of a realistic wind turbine, the vortex shedding will be formed at the very tip section because of the pressure difference between the pressure and suction side resulting in a cross flow over the tip of the blade [8]. The mechanism of the noise generation for the tip noise is very similar to the one of trailing edge noise [21]. Tip noise is affected by the blade load distribution, the strength of the tip vortex and the shape of the blade tip [33]. Tip noise is typically broadband and distributed at high-frequency range and is not considered to be the most important noise source for modern large wind turbines [8].

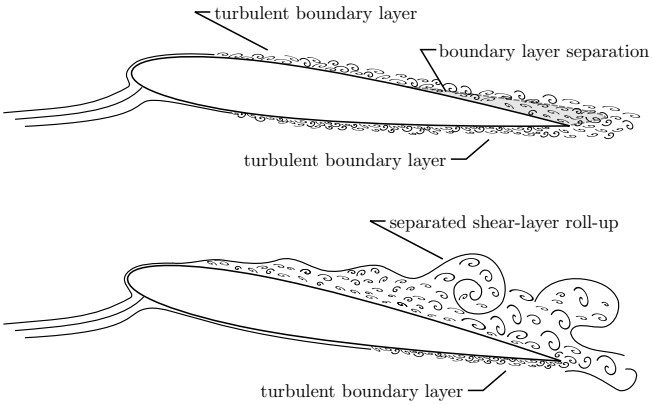

Figure 2.6: Vortex shedding from the trailing edge for separation (top) and stall (bottom) cases [21].

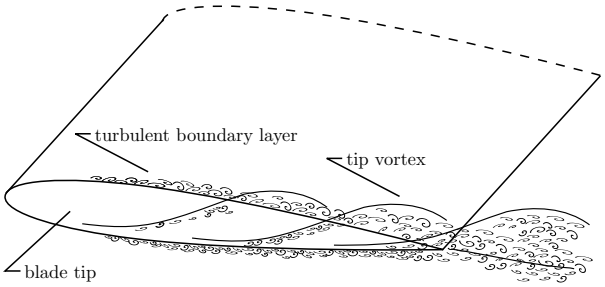

Figure 2.7: Formation of vortices at the tip of a blade [21].

2.1.4. EFFECTS OF BLADE DAMAGE ON AERODYNAMIC NOISE

When damage occurs on the blade, the shape or the surface roughness of the blade might change. This will consequently affect the velocity and pressure fields near the blade or on the surface thus leading to the changes in the far-field aerodynamic noise. For example, as leading edge erosion [34–36] occurs on a blade, the leading edge might have a reduced radius; there might be a step between the eroded part and the undamaged surface due to the surface delamination, and the eroded surface will become rougher. These changes in blade geometrical properties might cause a different velocity field near the leading edge and different development progress of the boundary layer thus different vortex shedding at the trailing edge. As a consequence, this will possibly affect both leading edge noise and trailing edge noise.

Another example of application for wind turbine blade condition monitoring using aerodynamic noise might be that: a modern pitch-controlled wind turbine usually works at low angles of attack far away from separation and stall conditions; therefore, if the spectral features of separation or stall noise are observed, the wind turbine might be working in an abnormal condition.

2.2. BEAMFORMING

A microphone array is a typical instrument for noise measurement for the wind turbines [37–39]or aircraft [39, 40] to assess their sound levels. By using the microphone array and beamforming, the noise source of interest can be separated from other sources and the environmental noise. This section will briefly introduce the algorithm of Conventional Frequency Domain Beamforming (CFDBF) [40, 41] and the associated post-processing for acoustic measurements in the wind tunnel tests.

2.2.1. CONVENTIONAL FREQUENCY DOMAIN BEAMFORMING

Assuming there is a 2-D planar microphone array with N microphones, as shown in 2.8, for each narrow band frequency, f, a complex vector with the dimension of $\mathbb{C}^{N\times 1}$ containing the Fourier transforms for all the signals of N microphones is defined as:

$$\mathbf{p} = \begin{pmatrix} p'_{\mathrm{FT},1}(f) \\ \vdots \\ p'_{\mathrm{FT},i}(f) \\ \vdots \\ p'_{\mathrm{FT},N}(f) \end{pmatrix} \tag{2.4}$$

where $p'_{\mathrm{FT},i}(f)$ is the Fourier transforms for the signal of the i microphone. The Cross-Spectral Matrix (CSM), $\mathbf{C} \in \mathbb{C}^{N\times N}$, is calculated as

$$\mathbf{C} = \frac{1}{2}\mathbf{p}\mathbf{p}^{*} \tag{2.5}$$

where $(\cdot)^{*}$ denotes the complex conjugate transpose. The diagonal elements of CSM are the auto power spectra of the microphone signals and the off-diagonal elements are the cross power spectra between signals of different two microphones.

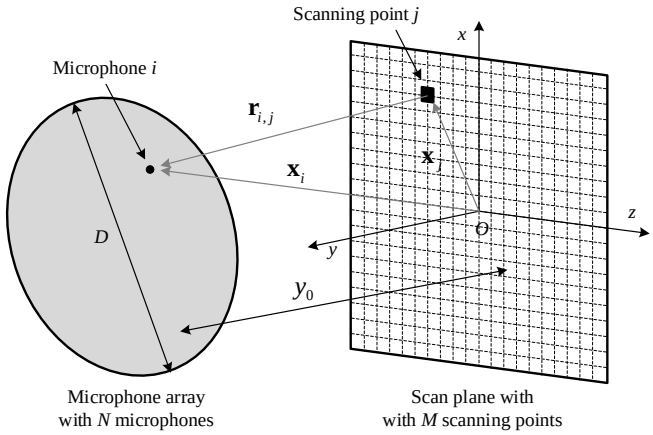

Figure 2.8: Schematic of the microphone array and the scan plane.

A scan plane is defined parallel to the microphone array, as shown in Figure 2.8, with M scanning points. A right-hand coordinate system is set at the center of the scan plane. Assuming there is a sound source with unit strength at $\mathbf{X}_j$ on the scan plane propagating to the i-th microphone at $\mathbf{X}_i$, the steering function, $g_{i,j}$, corresponding to the transfer function in the frequency domain from the sound source to the signal acquired by the microphone [37], is defined as

$$g_{i,j} = \frac{1}{\left\|\mathbf{r}_{i,j}\right\|} e^{-2\pi \mathrm{i} f \Delta t_e} \tag{2.6}$$

where the relative position of the ith microphone to the jth scanning point is calculated as $\mathbf{r}_{i,j} = \mathbf{X}_i - \mathbf{X}_j$; i is the imaginary unit, $\mathrm{i} = \sqrt{-1}$; Δt_e is the delayed time, $\Delta t_e = \left\|\mathbf{r}_{i,j}\right\| / c$ (c is the sound speed). The above equation is the representation of an omnidirectional monopole source from Green's function of Helmholtz equation, in which the division by the denominator term $\left\|\mathbf{r}_{i,j}\right\|$ considers the decay of the amplitude because of the distance between the sound source and the microphone [37].

For all N microphones, the steering vectors $\mathbf{g}_j \in \mathbb{C}^{N\times 1}$ are built containing N elements of $g_{i,j}$. The purpose of beamforming is to estimate the complex amplitudes, a_j, of the sound source at $\mathbf{X}_j$ using the measured spectra from the microphones, $\mathbf{p}$. The problem can be solved through solving the minimization of

$$J = \left\|\mathbf{p} - a_j \mathbf{g}_j\right\| \tag{2.7}$$

The solution is

$$a_j = \frac{\mathbf{g}_j^* \mathbf{p}}{\left\|\mathbf{g}_j\right\|^2} \tag{2.8}$$

Then the auto-power spectrum at the scanning point j is calculated as

$$A_j = \frac{1}{2} a a^* = \frac{\mathbf{g}_j^* \mathbf{C} \mathbf{g}_j}{\|\mathbf{g}_j\|^4} \tag{2.9}$$

The sound pressure level, $L_{p,j}$, at $\mathbf{X}_j$ of the scan plane is calculated as

$$L_{p,j} = 10 \log \frac{A_j}{p_0^2} \tag{2.10}$$

where p_0 is the reference pressure, 2×10^{-5} Pa in air. Finally, the above procedure is applied to each scanning point to get a beamforming map at a given narrow band frequency.

CORRECTION FOR THE PRESENCE OF FLOW

When the flow is present, such as the test in a wind tunnel, the sound propagating path will be changed, as shown in 2.9. Assuming the measurement is carried out in an infinite flow with the Mach number vector Figure $\mathbf{M} = [M_x, M_y, M_z]$, the relative position of the microphone to the scanning point is corrected as [37, 39]

$$\mathbf{r}'_{i,j} = \sqrt{\left(\mathbf{M}\mathbf{r}_{i,j}\right)^2 + \beta^2 \left\|\mathbf{r}_{i,j}\right\|^2} \tag{2.11}$$

where $\beta = \sqrt{1 - \|\mathbf{M}\|^2}$. And the delayed time of the sound emitted to the microphone becomes

$$\Delta t_e = \frac{-\mathbf{M}\mathbf{r}_{i,j} + \mathbf{r}'_{i,j}}{c\beta^2} \tag{2.12}$$

The corrected $\mathbf{r}'_{i,j}$ and Δt_e replace the original ones in Equation 2.6.

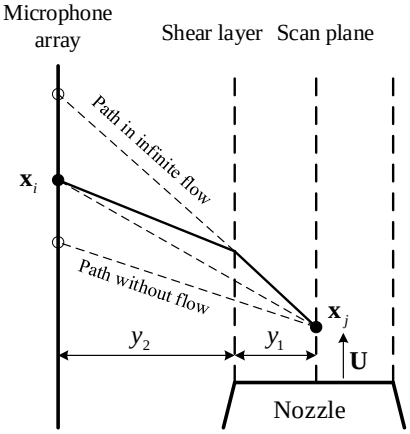

Figure 2.9: Schematic of measurement in an open-jet wind tunnel with flow shear layer.

For an open-jet wind tunnel, like A-tunnel [42] in this thesis, the microphone array is put out of the flow. In this case, the sound propagates through a moving medium and the stationary medium, where a shear layer is in between, as shown in Figure 2.9. The effect on the sound propagation of the shear layer is needed to be considered. In this thesis, a simple correction is adopted as reported in [37] for open-jet wind tunnel applications when the Mach number is below 0.25 and the angle between the shear layer and the sound emitted path is greater than 45°. Assuming that the wind tunnel velocity is only in x direction, i.e., $\mathbf{U} = [U_x, 0, 0]$ and $\mathbf{M} = [M_x, 0, 0]$, and the distances of the shear layer to the scan plane and the microphone array are y_1 and y_2, respectively, a corrected Mach number for M_x is taken as

$$M_x' = \frac{y_1}{y_1 + y_2} M_x \tag{2.13}$$

The above Equation 2.13 also works for other cases if the microphone array is put parallel to xoy plane or any other locations by calculating other two components, M_y and M_z. Then the corrected Mach number $\mathbf{M}' = [M_x', M_y', M_z']$ replaces the original one in the Equations 2.11 and 2.12.

RESOLUTION LIMIT AND SIDELOBES

Because of the limited size of the microphone array, although a monopole source assumption is applied, in a beamforming map, the obtained sound source pattern is always spread with a mainlobe of a certain width and a series of sidelobes. This mapping relationship from the monopole source to the beamforming map is determined by the Point Spread Function (PSF) of the microphone array [43, 44].

Due to the spread width of the mainlobe, the resulting sound source in a beamforming map might be partially overlapping with neighbors, making it difficult to separate them. The spatial resolution, which means the minimum distance of two sources able to be separated on the beamforming map, relies on the array diameter, D, the distance between the array and the scan plane, y_0, and the sound wavelength, λ. This is determined by Rayleigh limit [45, 46],

$$\Delta l = y_0 \tan\left(1.22\frac{\lambda}{D}\right) \approx 1.22 y_0 \frac{\lambda}{D} = 1.22 y_0 \frac{c}{fD} \tag{2.14}$$

The spatial resolution is proportional to the distance between the microphone array and the scan plane and inversely proportional to the diameter of the microphone array. This suggests that a larger array or placing the array closer to the sound sources can improve spatial resolution. On the other hand, for a fixed setup of the microphone array in practice, the low-frequency contributions of the spectra are usually with the worse spatial resolution. Fine-tuning for the location of the array can provide an acceptable resolution applicable to the lowest frequency band of interest.

On the other hand, as mentioned previously, the accompanying high-level sidelobes of a strong sound source may hide other real sound sources (for example the secondary sound sources) on the beamforming maps. This effect becomes especially significant for high-frequency sound sources.

2.2.2. BACKGROUND NOISE SUBTRACTION

For the measurement in the wind tunnel, the microphone measures not only the sound signal of interest but also the background noise. And the interference of the electronic noise will also affect the measurement. The measured signal of time t from the microphone i, $p'_i(t)$ can be decomposed as

$$p'_i(t) = p'_{s,i}(t) + p'_{BG,i}(t) + n_i(t) = p'_{s,i}(t) + p'_{d,i}(t) \tag{2.15}$$

where $p'_{s,i}(t)$, $p'_{BG,i}(t)$ and $n_i(t)$ denote the components of the real sound signal of interest, background noise and the electronic noise, respectively; the undesirable terms $p'_{BG,i}(t)$ and $n_i(t)$ are merged as $p'_{d,i}(t)$. Considering all three components are stochastic stationary and uncorrelated, the Cross-Spectral Matrix (CSM) for N microphones is

$$\mathbf{C} = \mathbf{C}_s + \mathbf{C}_d \tag{2.16}$$

where $\mathbf{C}_s$ and $\mathbf{C}_d$ are the CSMs for the component of interest and the undesirable terms of the background and electronic noise.

In this thesis, Eigenvalue Identification and Subtraction (EIS) [47] is applied to mitigate the undesirable noise. CSM is actually a covariance matrix of narrow-band Fourier coefficients which makes it a positive semidefinite Hermitian matrix. The CSM of undesirable terms can be decomposed as

$$\mathbf{C}_d = \mathbf{X}_d \Lambda_d \mathbf{X}_d^* \tag{2.17}$$

where $\Lambda_d \in \mathbb{R}^{N\times N}$ is a diagonal matrix containing the eigenvalues $\lambda_{i,d}$; $\mathbf{X}_d$ is a Hermitian matrix of eigenvectors with the property $\mathbf{X}_d\mathbf{X}_d^* = \mathbf{X}_d^*\mathbf{X}_d = \mathbf{I}$. Defining operator terms $\mathbf{B}_d = \mathbf{X}_d\Lambda_d^{-1/2}$ and $\mathbf{B}_d^*(\cdot)\mathbf{B}_d = \widehat{(\cdot)}$, Equation 2.17 is therefore simplified as

$$\mathbf{B}_d^*\mathbf{C}_d\mathbf{B}_d = \widehat{\mathbf{C}}_d = \mathbf{I} \tag{2.18}$$

And the operator terms are applied to Equation 2.16, which yields

$$\widehat{\mathbf{C}} = \widehat{\mathbf{C}}_s + \mathbf{I} \tag{2.19}$$

On the other hand, it can be proved that the eigenvectors of $\widehat{\mathbf{C}}$ are also the ones of $\widehat{\mathbf{C}}_s$ [47], because of the eigenvalue decomposition for Equation 2.19

$$\widehat{\mathbf{C}} = \widehat{\mathbf{X}}\widehat{\Lambda}\widehat{\mathbf{X}}^* = \widehat{\mathbf{X}}_s\widehat{\Lambda}_s\widehat{\mathbf{X}}_s^* + \mathbf{I} = \widehat{\mathbf{X}}_s\left(\widehat{\Lambda}_s + \mathbf{I}\right)\widehat{\mathbf{X}}_s^* \tag{2.20}$$

Additionally it is suggested that the eigenvalues of $\widehat{\mathbf{C}}$ relies on the ones of $\widehat{\mathbf{C}}_s$, with $\widehat{\lambda}_i = \widehat{\lambda}_{i,s} + 1$. The eigenvalues greater than the unity correspond to the eigenvalue-eigenvector pairs of $\widehat{\mathbf{C}}_s$, and those equal to the unity are associated with the undesirable noise. Therefore, subtraction is established by performing eigenvalue decomposition for $\widehat{\mathbf{C}}$ and then subtracting the identity matrix from $\widehat{\Lambda}$, i.e., $\widehat{\Lambda}_s = \widehat{\Lambda} - \mathbf{I}$. The CSM is reconstructed only considering the reduced space with the eigenvalues greater than zero. Finally, the estimation for $\mathbf{C}_s$ is converted back by

$$\mathbf{C}_s = \left(\mathbf{B}_d^{-1}\right)^* \widehat{\mathbf{C}}_s \mathbf{B}_d^{-1} \tag{2.21}$$

where $\mathbf{B}_d^{-1} = \Lambda_d^{1/2}\mathbf{X}_d^*$.

2.2.3. SOURCE POWER INTEGRATION TECHNIQUE

The noise scattered from an airfoil is usually distributed as line sources, for example, the trailing edge noise and the leading edge noise. In this case, it is challenging to quantify the sound levels for such sound sources by just selecting one point on the beamforming map. In order to quantify the sound levels for distributed sources, Source Power Integration (SPI) technique [39, 40] is applied.

The purpose of SPI is to integrate the source power within the Region of Integration (ROI) and then to scale the source power to a simulated unit monopole source. The scaling factor represents the total sound power within the ROI. A ROI of interest with J points on the beamforming map is selected, on which the power of each point j is $A_{j,\text{exp}}$. On the other hand, a unit monopole source is set on the center of the ROI (assuming it is the kth point on the ROI), and the source power spread to the points of ROI due to the PSF is $A_{j,\text{sim}}$. The SPI method assumes the following relationship holds

$$\frac{\sum_j^J A_{j,\text{exp}}}{P_{\text{exp}}} = \frac{\sum_j^J A_{j,\text{sim}}}{P_{\text{sim}}} \tag{2.22}$$

where P_{exp} is the total sound power source power; P_{sim} is the power for the simulated monopole source and $P_{\text{sim}} = 1$. Then P_{exp} can be solved as by

$$P_{\text{exp}} = \frac{P_{\text{sim}} \sum_j^J \mathbf{g}_j^* \mathbf{C} \mathbf{g}_j}{\sum_j^J \mathbf{g}_j^* \left(\mathbf{g}_k \mathbf{g}_k^*\right) \mathbf{g}_j} \tag{2.23}$$

where $\mathbf{g}_k$ is the steering vector to the kth point on the ROI where the simulated monopole source is located; $\left(\mathbf{g}_k \mathbf{g}_k^*\right)$ is actually the CSM of the simulated sound signals of the monopole source acquired by the microphone array.

In practice, the ROI should be set large enough to capture the potential main-lobe broadening due to coherence loss [37] for frequencies of interest. However, the ROI should avoid containing the contributions of other noise sources and their sidelobes [40].

2.3. EXPERIMENTAL FACILITIES AND SETUP

The experiments involved in this thesis were mainly carried out in the A-tunnel (anechoic wind tunnel) of Delft University of Technology [42]. In wind farms, the atmospheric turbulence and wakes induced by the upstream wind turbines lead to turbulent inflow conditions for the downstream wind turbines. To mimic such turbulent inflows, two grids were designed and mounted on the nozzle of the wind tunnel to generate turbulent flows. Two airfoils, with NACA 0018 and DU96 W180 profiles, were investigated. The selection of these two types of airfoils is for comparison with previous studies on trailing-edge noise [21] and leading-edge erosion [48]. These two airfoils are modular with changeable trailing edge and leading edge parts, thus allowing the testing of different types and severities of damage. A 2-D planner phased microphone array is used for the acoustic measurements. To understand how damage changes the flow fields and boundary layer properties associated with the noise emission, flow field measurements are carried out using a Particle Image Velocimetry (PIV) technique, and the development

and transition of the boundary layer transition are visualized by a surface oil flow visualization technique. This section presents the detailed experimental setup in the wind tunnel, the design of the turbulence-generating grids, and characterizations for the aerodynamic and acoustic measurements.

2.3.1. WIND TUNNEL FACILITY

A schematic illustration of the A-tunnel is shown in Figure 2.10(a). The A-tunnel is a vertical open-jet wind tunnel within an anechoic room. The absorbent foam wedges are furnished on the walls of the test room. The height of foam wedges is 0.49 m which provides an acoustic cutoff frequency of 173.5 Hz [42]. The rectangular test section of the wind tunnel, as shown in 2.10(b), is 40 cm × 70 cm, allowing experiments up to 45 m/s free stream velocity below 0.1% turbulence intensity. The uniformity of the mean flow velocity within the entire test section is below 0.5% with respect to the center velocity of the outlet [42, 49].

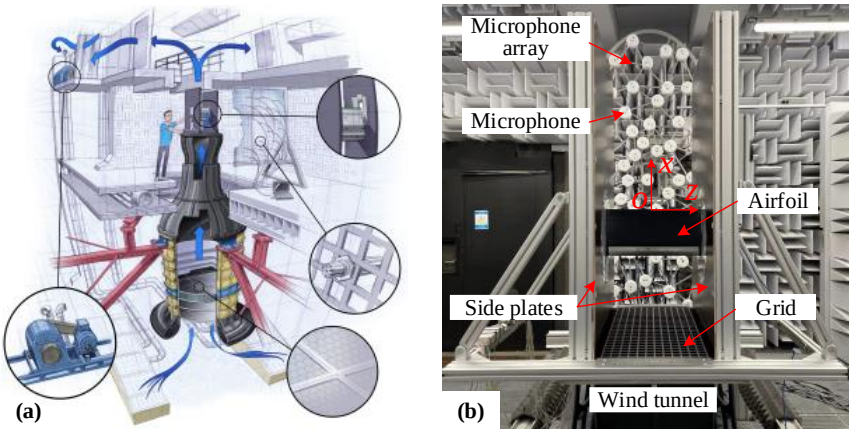

Figure 2.10: A-tunnel facility: (a) a schematic illustration [42] and (b) test section [1].

The test section is equipped with two side plates to hold the tested airfoil model by two round panels thus providing a 2-D flow in the airfoil spanwise direction. The angle of attack of the airfoil can be accurately controlled by rotating the round panels with a stepper motor. The round panels are made of transparent acrylic material making it possible for optical measurements of the flow fields around the airfoil, such as the Particle Image Velocimetry (PIV) technique. The horizontal aluminum frame beams of the test section structure have screw slots, on which the turbulence-generating grid can be easily mounted.

A right-hand *o-xyz* coordinate system is established taking the mid-span of the airfoil trailing edge as the origin and free-stream direction as the *x*-axis to describe the experimental setup in this thesis as shown in Figure 2.10.

2.3.2. TURBULENCE-GENERATING GRIDS

DESIGN FOR THE GRIDS

When a grid is mounted on the nozzle, in the region near the grid, the flow is disturbed by the grid and transits to be turbulent rapidly due to the presence of the grid and the turbulence is inhomogeneous and anisotropic due to the wake effect of the grid. After a certain distance downstream, the turbulence is fully developed and flow tends to approach homogeneity and local isotropy, where the turbulence energy decays with a power law. At the region far from the grid, the viscous effect predominates and the flow becomes anisotropic. The identification of the regions of the grid-generated turbulence is shown in Figure 2.11 [50]. For better quantification and control of turbulence characteristics, the experiments are ideally operating under isotropic turbulent conditions.

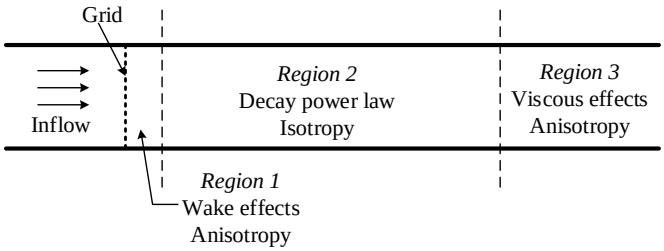

Figure 2.11: The regions of identification in grid generated turbulence.

The characteristics of the turbulence (turbulence intensity, I, and the integral length scale, Λ_f) downstream depend on the geometry of the grid and the measurement location [50–52]. The grid space, M_u, and the beam size, d, are the main parameters to define a squared grid [50], as shown in Figure 2.12(a). In the experiments of this thesis, the airfoils are mounted over the nozzle at a fixed height of 300 mm (measured from the leading edge) to the nozzle plane where the grid is located.

The design for the grids is based on the desired turbulence intensities. In the power decay region, the energy of the turbulence decay law holds [50, 51], i.e.,

$$I^2 = \left(\frac{u'}{U}\right)^2 = A_I \left(\frac{x - x_0}{M_u}\right)^n \tag{2.24}$$

where u' is the root-mean-square of the turbulent velocity fluctuation; x is the relative location downstream to the grid; x_0 is a virtual origin of the grid usually close to the actual position of the grid, which relies on grid-space-based Reynolds number, $Re_M = \rho U M_u / \mu$ (ρ and μ are density and dynamic viscosity of the air, respectively) and the solidity of the grid ($\sigma_g = d\,(2M_u - d)\,/\,M_u^2$); A_I is a universal constant depending on Re_M, which is around 0.04 for large Reynolds number, $Re_M > 2000$ [50]; n is a decay exponent which is -1.2 if x_0 is assumed to be 0.

The typical turbulence intensity at wind turbine hub height is 6 – 8% offshore and 10 – 12% onshore [53]. In this thesis, two turbulent inflow conditions are designed for the turbulence intensities at 5% and 11%. Based on Equation 2.24 and the relevant require-

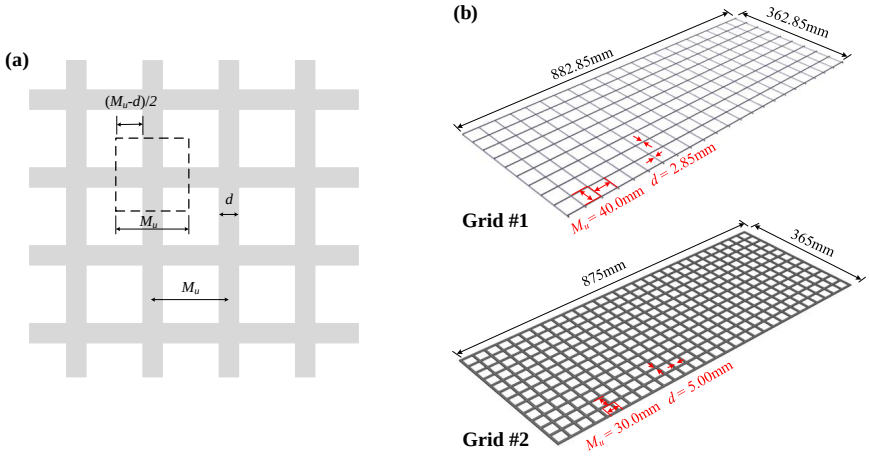

Figure 2.12: Turbulence generating grids used in the experiments: (a) the geometric definition for the grid (b) grids #1 and #2.

ments of setup and the desired turbulence intensities, two grids are designed as shown in 2.12 (b) and their geometric dimensions are listed in Table 2.1.

Table 2.1: Dimensions of the two turbulence generating grids.

Grid No.	Beam type	Grid space, M_u (mm)	Beam size, d (mm)	Length (mm)	Width (mm)
#1	Rod	40.0	2.85	882.85	362.85
#2	Flat	30.0	5.00	875	365

CHARACTERIZATION FOR TURBULENT INFLOW

Turbulence downstream of the grid was characterized using hotwire anemometry. Data were sampled at a frequency of 51.2 kHz. The characterization was carried out without the airfoil installed in the test section. To check the uniformity of the turbulence, data were collected at 5 points along the x-axis upstream of the airfoil leading edge and 11 points in the spanwise direction as shown in Figure 2.13; the spacing between two points was 20 mm. For each measurement, data were recorded for 20 s.

The measurements for mean velocity were calibrated by referring to the measured mean velocity using the Prandtl tube. To avoid the influence of the measurements on each other, the hotwire probe and the Prandtl tube were placed at the same height but symmetrical positions regarding the center line of the wind tunnel nozzle, where the mean velocities can be considered to be the same. A series of mean velocities, U, and the corresponding output voltages of the hot-wire anemometer, V, were recorded and a fourth-order poly-fit was performed to fit the relationship

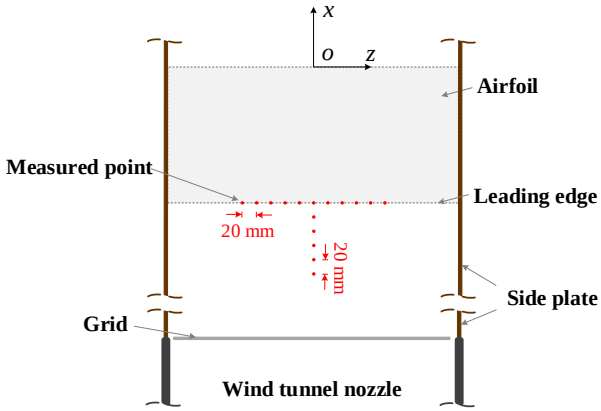

Figure 2.13: Turbulence characterization positions.

$$U = C_0 + C_1 V + C_2 V^2 + C_3 V^3 + C_4 V^4 \tag{2.25}$$

where C_0 to C_4 are the fitting coefficients. Figure 2.16 shows the calibration results for the mean flow velocity and the calibration uncertainty, σ_U, which is calculated as

$$\sigma_U = \frac{|U - \hat{U}|}{U} \times 100\% \tag{2.26}$$

where $\hat{U}$ is the calculated velocity from the fitting Equation 2.25. The results show that the relationship between the mean velocity and the hotwire output voltage agrees well with a fourth-order poly-fit and the uncertainty among the entire velocity range is below 1%, which suggests a fine calibration is established.

To confirm if the airfoil is located in the isotropic turbulence region, the power decay of turbulence upstream of the airfoil leading edge is analyzed, as shown in Figure 2.15. For both grids under different inflow velocities, U_∞, of interest, the turbulence power decays by a power law with the exponent, $n = -1.2$, which agrees with the previous findings [50] and suggests the turbulence at the location of the airfoil leading edge is already homogeneous and locally isotropic. Turbulence intensities of flow at the leading edge of the airfoil without and with the grids under different mean flow velocities are listed in Table 2.2. The power spectral densities (PSDs), S_{uu}, of the turbulent fluctuations under different mean flow velocities are shown in Figure 2.16. Results show the broadband characteristics of the spectral content and the spectra in the middle and high frequency (inertial subrange) agree well with Kolmogorov's law of the turbulence energy cascade [54].

From the time series, the turbulence integral time scale, Λ_t, can be calculated from the autocorrelation function

$$R_{\tau\tau}(\tau) = \frac{u'(t)\,\bar{u}'(t+\tau)}{u'^2} \tag{2.27}$$

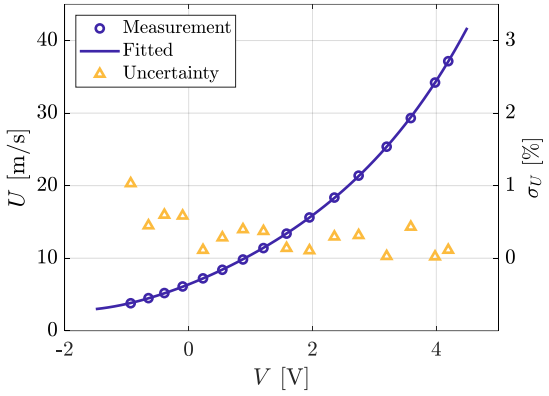

Figure 2.14: Calibration for the mean velocity and the calibration uncertainty.

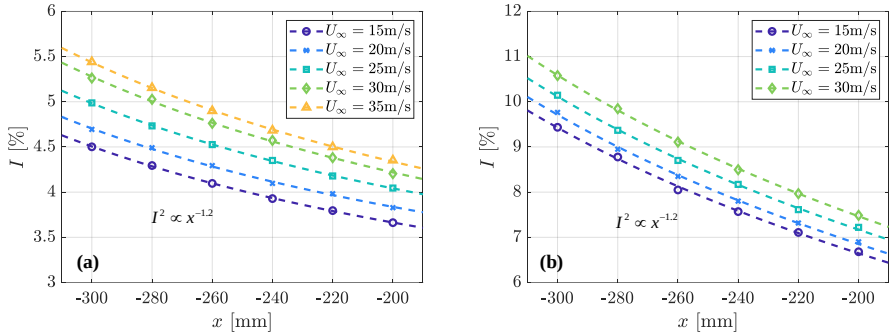

Figure 2.15: Turbulence intensity downstream when the grid is mounted: (a) grid #1 and (b) grid #2.

Table 2.2: Turbulence intensities (%) of the flow without and with the grids under different mean flow velocity conditions.

U_∞ (m/s)	15	20	25	30	35
No Grid	0.17	0.18	0.18	0.20	0.18
#1	3.71	3.90	4.10	4.21	4.32
#2	6.77	7.03	7.30	7.49	-

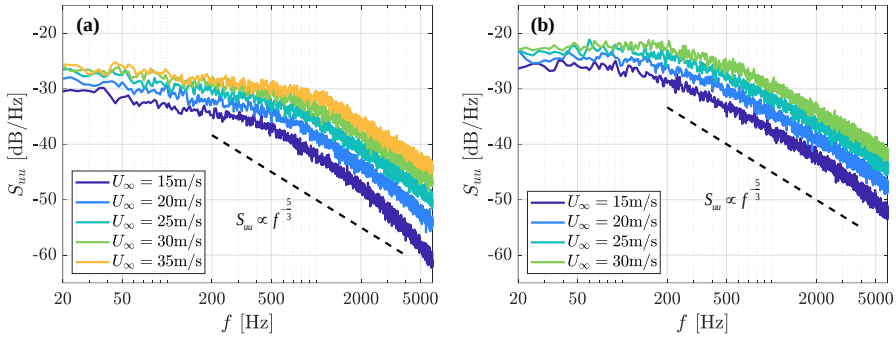

Figure 2.16: The spectra of the turbulent flow under different mean flow velocities when the grid is mounted: (a) grid #1 and (b) grid #2.

where $(\bar{\cdot})$ denotes the time average and

$$\Lambda_t = \int_0^\infty R_{\tau\tau}(\tau)\,\mathrm{d}\tau \tag{2.28}$$

Then the integral length scale, Λ_f, can be calculated as follows, where Taylor's hypothesis of frozen turbulence is applied

$$\Lambda_f = \Lambda_t U_\infty \tag{2.29}$$

Also, Equations 2.28 and 2.29 can be written in the form of an autocorrelation function based on the displacement of the vortex (R_{xx}, where $x = \tau U_\infty$)

$$\Lambda_f = \int_0^\infty R_{xx}(x)\,\mathrm{d}x \tag{2.30}$$

In Figure 2.17, the measured autocorrelation for each grid is plotted as a function of displacement from the center of the leading edge together with an exponential fit of the form $R_{xx} = e^{-x/\Lambda_f}$. The resulting turbulence length scale for each grid is given in Table 2.3.

Table 2.3: The turbulence integral length scale of the flow with the grids.

Grid No.	Turbulence integral length scale (mm)
#1	7.9
#2	10.2

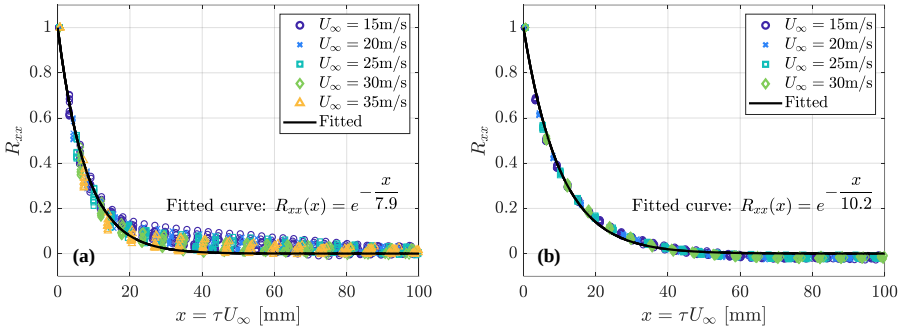

Figure 2.17: The autocorrelation function for different inflow velocities: (a) grid #1 and (b) grid #2.

2.3.3. AIRFOIL MODELS

BASELINE AIRFOILS

The airfoil profiles used in the experiments were NACA 0018 and DU96 W180, as shown in Figure 2.18. NACA 0018 is a symmetrical airfoil profile and is widely used for fundamental studies on aeroacoustics [49, 55, 56] and aerodynamics [57–59]. DU96 W180 is a cambered airfoil profile that was designed by Delft University of Technology and has been applied to wind energy applications [60–62]. Both airfoil profiles have a maximum thickness of 18%. In this thesis, the NACA 0018 airfoil is used for the trailing edge crack detection, while the DU96 W180 one is for the leading edge erosion detection.

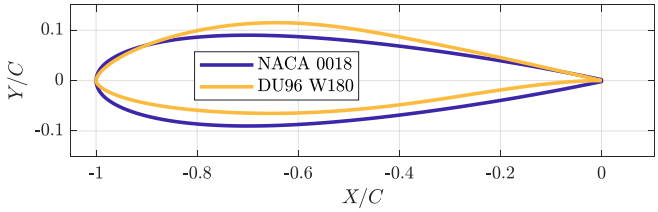

Figure 2.18: Airfoil profiles for NACA 0018 and DU96 W180.

The test airfoil models were made from solid aluminum using computer numerical control (CNC) machining (surface roughness of 0.05 mm), as shown in Figure 2.19. Both airfoil models have a chord length, C, of 200 mm and a span length, L, of 400 mm ($L/C = 2$). The NACA 0018 airfoil model has exchangeable trailing edges which allows the tests for different trailing edge configurations with different cracks. For the DU96 W180 airfoil model, both the leading edge and the trailing edge are modular, which is flexible to change the different eroded leading edge inserts for this research and also provides the possibility for trailing edge studies in the future. In this thesis, an *O-XYZ* coordinate system is established for describing the geometry of the airfoil models taking the geometric

center of the trailing edge as an origin, as shown in Figures 2.18 and 2.19.

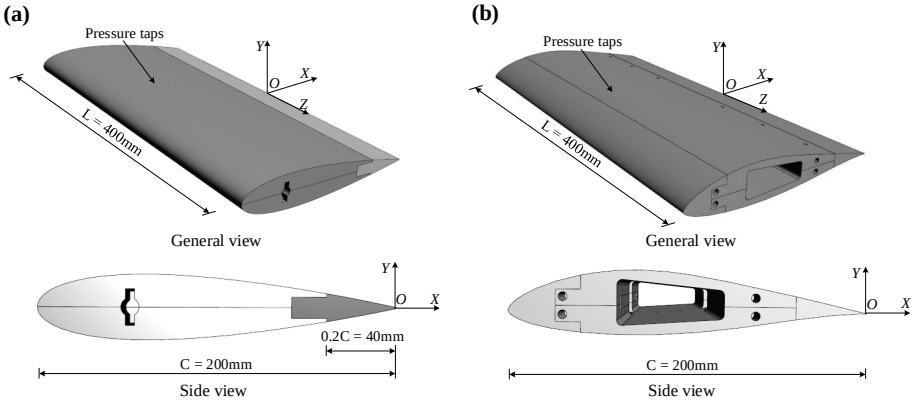

Figure 2.19: Geometry for the airfoils : (a) NACA 0018 and (b) DU96 W180.

CALIBRATION FOR THE ANGLE OF ATTACK

The effective angle of attack α^* of the airfoil is usually smaller than the geometrical one, α, accounting for the deflection of the incident flow due to the finite size of the open jet [21]. To obtain the effective angle of attack, surface pressure measurements were acquired and the results were compared with XFOIL [63]. A total of 15 (for NACA 0018 airfoil model) or 16 (for DU96 W180 airfoil model) pressure taps with a diameter of 0.4 mm on both the pressure side and suction side were used for this purpose, as shown in Figure 2.19. The pressure taps are distributed in the range of $-0.99 \leq X \leq -0.34$ and $-0.99 \leq X \leq -0.175$ for NACA 0018 and DU96 W180 airfoil models, respectively. The pressure tapes are tilted 15° with respect to the centerline to avoid near wake interference from the upstream taps. The pressure taps were connected to pressure transducers with a measurable range of ±2.5 kPa and an accuracy of 12.5 Pa. Pressure data were recorded for a period of 2 s with a sampling frequency of 100 Hz and then averaged.

The differential pressure coefficient, $\Delta C_{p,i}$, at location X_i can be calculated from differential pressure between the pressure side and suction side, $\Delta p_i = p_{i,\mathrm{p}} - p_{i,\mathrm{s}}$, i.e.,

$$\Delta C_{p,i} = \frac{\Delta p_i}{0.5\rho U_\infty^2} \tag{2.31}$$

where $p_{i,\mathrm{p}}$ and $p_{i,\mathrm{s}}$, can be measured with the paired pressure taps on the pressure side and suction side located at X_i, respectively; U_∞ is the inflow velocity. Then the coefficient of lift, C_l, can be integrated along the chordwise for all the pressure taps, as

$$C_l = \frac{1}{C}\sum_{i=1}^{N-1}\frac{\Delta C_{p,i} + \Delta C_{p,i+1}}{2}\Delta X_i \tag{2.32}$$

where $\Delta C_{p,i}$ denotes the pressure coefficient of the ith paired tapes; ΔX_i is the chordwise distance between the ith and $i+1$th pressure tapes; N is the number of the pressure taps,

15 for NACA 0018 airfoil model and 16 for DU96 W180 one.

The calibration for the angle of attack was conducted under an inflow velocity of U_∞ = 20 m/s and the corresponding chord-length-based Reynolds number of $Re_C = 2.7\times10^5$. As shown in Figure 2.20, the relationships between the coefficient of lift, C_l, and the angle of attack for both airfoil models are plotted with a series of geometric angles of attack, α. The $C_l - \alpha$ data from XFOIL are plotted for reference and are fitted in first-order functions in the linear region. The slopes of the fitting curves, which are 0.1130 and 0.1073 for NACA 0018 and DU96 W180 airfoils, respectively, are very close to the theoretical value of a thin flat plate which is $(2\pi)^2/360 \approx 0.110$ (with α in degrees). Then the effective angle of attack, α^*, can be calibrated and deduced from the measured C_l referring to the one from XFOIL.

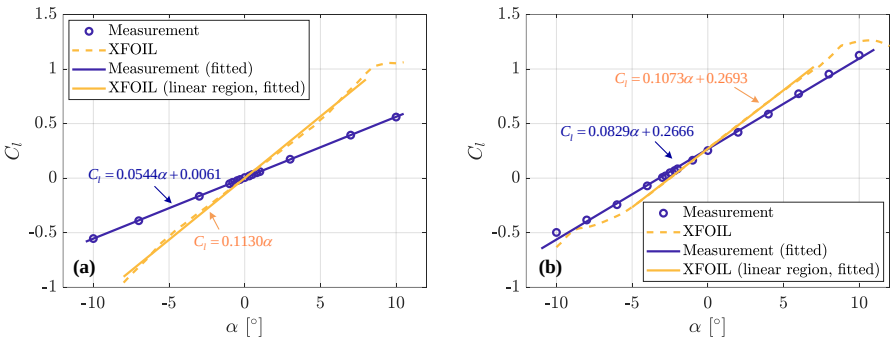

Figure 2.20: Calibration for angle of attack: (a) NACA 0018 and (b) DU96 W180.

The difference between the constant terms of the fitting curves for the measured and XFOIL data is small enough and can be negligible. Therefore effective angle of attack can be simply corrected by the geometrical one by considering a factor of

$$\eta = \frac{\alpha^*}{\alpha} \tag{2.33}$$

which is $\eta = 0.0544/0.1130 = 0.48$ and $\eta = 0.0829/0.1073 = 0.77$ for NACA 0018 and DU96 W180 airfoil models, respectively. Unless otherwise specified, for the remainder of this thesis, angle of attack refers to the geometrical one.

AIRFOILS WITH DAMAGE

The trailing edge crack happens when the adhesive joint fails. The forces act on the damage point in the spanwise direction and consequently, the top layer and bottom layer are separated to be a crack, as shown in Figure 2.21(a), thus making the trailing edge thicker than the healthy one. At the moment, there is no geometry and measurements about the trailing crack in the literature. In this thesis, a trailing edge crack is designed as a rectangular slot at the trailing edge through the whole span. Compared to the baseline trailing edge (healthy airfoil with a tailing edge thickness of h_{Baseline}), the total thickness of the trailing edge with damage, h, is increased by the width of the crack, W, i.e.,

$h = h_{\text{Baseline}} + W$. The detailed measurements for the trailing edge crack are reported in Chapter 3.

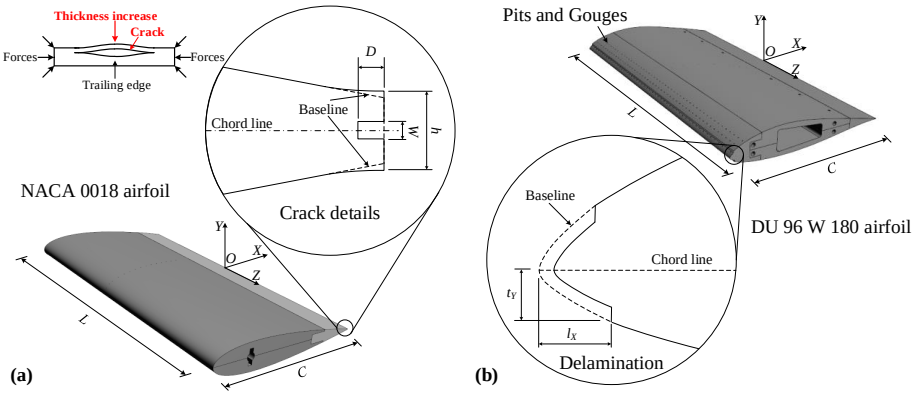

Figure 2.21: Airfoil profiles for NACA 0018 and DU96 W180.

The geometry and dimension of the leading edge erosion are scaled using the measurements of real eroded wind turbine blades from 3M [48]. The leading edge erosion is characterized by the combination of pits, gouges and coating delamination, as shown in Figure 2.21(b). The detailed design for leading edge inserts with erosion is reported in Chapter 5.

2.3.4. MICROPHONE ARRAY AND ACOUSTIC MEASUREMENTS

The microphone array used in this thesis contains 64 *G.R.A.S. 40PH* free-field microphones. The distribution of the microphones on the array is shown in Figure 2.22. The frequency response of the microphone is within ±1 dB from 50 Hz to 5 kHz and within ±2 dB from 5 k to 20 kHz and the maximum output is 135 dB (reference pressure 20 μPa). The microphone array was placed at 1 m parallel to the airfoil chord line (at zero angle of attack). The array diameters in x direction and z direction are $D_x = 1.875$ m and $D_z = 0.930$ m, respectively. This results in spatial resolutions in these two directions of Δl_x and Δl_z for different frequencies which are calculated using Equation 2.14 and shown in Figure 2.23.

The sampling frequency of each microphone, f_S, was 51.2 kHz. For each measurement, the signal was recorded for 20 s. The signal was separated into time blocks of 5120 samples for each Fourier transform thus giving a frequency resolution of 10 Hz. A scan plane for beamforming is taken in *xoz* plane within $-0.5\text{m} \leq x \leq 0.5\text{m}$, $-0.5\text{m} \leq z \leq 0.5\text{m}$ with a grid space of 2 mm. In this thesis, for the validation of the wind tunnel background noise and trailing edge crack detection, the sound power was integrated within a 0.2m × 0.2m region centered at the trailing edge mid-point. For the leading edge erosion detection, there were two integrated regions with a size of 0.1m × 0.2m centered at the leading edge and trailing edge mid-points to investigate the noise scattered at both

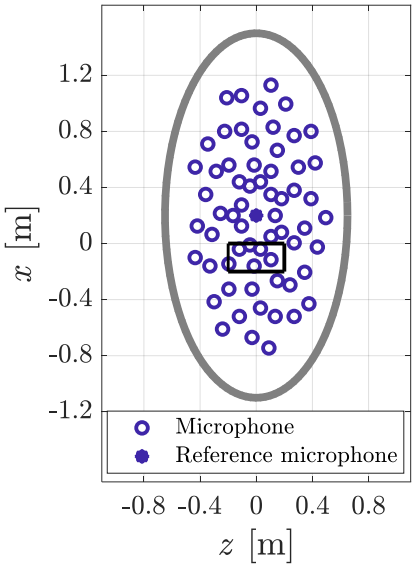

Figure 2.22: The distributions of the microphones on the array (the rectangular box is the projection of the airfoil on the array plane).

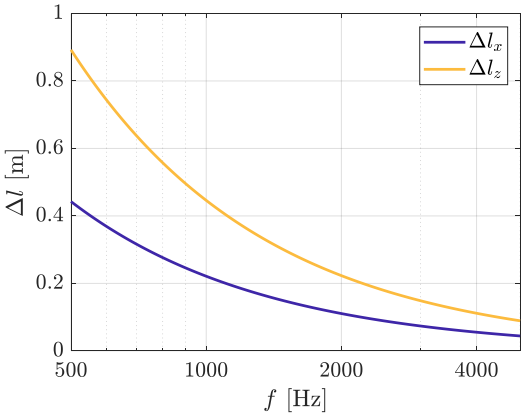

Figure 2.23: The spatial resolutions in x and z directions for different frequencies.

locations respectively.

The background noise was measured both for the clean inflow and turbulent inflow conditions. Further, to mitigate the effect of background noise on the measurements for the airfoil noise, EIS is employed to subtract the incoherent background noise sources for all the test cases. Figure 2.24 shows an example of background noise subtraction for NACA 0018 baseline airfoil with grid #1 mounted. The beamforming map is integrated within a 1/3 octave band with a central frequency of 1250 Hz. Due to the presence of the turbulent inflow, the leading edge noise is dominant in the beamforming map in this frequency band. It shows that the beamforming map with EIS is cleaner to identify the leading edge noise, which suggests EIS is valid and helpful for the applications in this thesis.

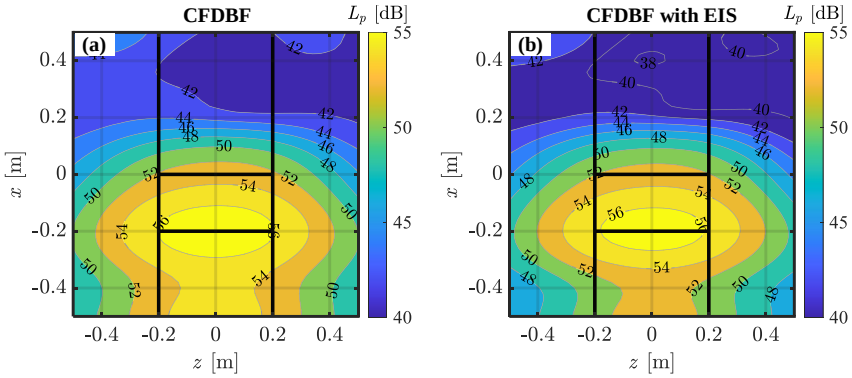

Figure 2.24: An example for background noise subtraction: (a) original beamforming map and (b) same beamforming map with EIS applied.

In order to assess background noise levels for different test velocities and turbulence conditions, the relative sound pressure levels (signal-to-noise ratios, SNRs), ΔL_p, are defined for the characterization of the background noise levels as

$$\Delta L_p = 10\log\left(\frac{p'^2_{\text{Baseline}}}{p'^2_{\text{BG}}}\right) = L_{p,\text{Baseline}} - L_{p,\text{BG}} \tag{2.34}$$

where p'_{Baseline} and p'_{BG} are root-mean-square of of sound pressure fluctuations for the cases with a baseline airfoil and without the airfoil mounted, respectively; $L_{p,\text{Baseline}}$ and $L_{p,\text{BG}}$ are sound pressure levels for both cases. Figure 2.25 shows the sound pressure levels and relative sound pressure levels for clean and turbulent inflow conditions, of which the sound power is integrated within a 0.2 m × 0.2 m square centered at the midspan of NACA 0018 airfoil. The left column shows examples of the sound pressure levels for different cases. For the clean inflow and grid #2 (flat beam) mounted cases, the spectra of the noise show broadband characteristics while for grid #1, there is a significant tonal component in the spectrum which is due to the coherent vortex shedding after the rod beams of the grid [64]. The right column shows the relative sound pressure levels for

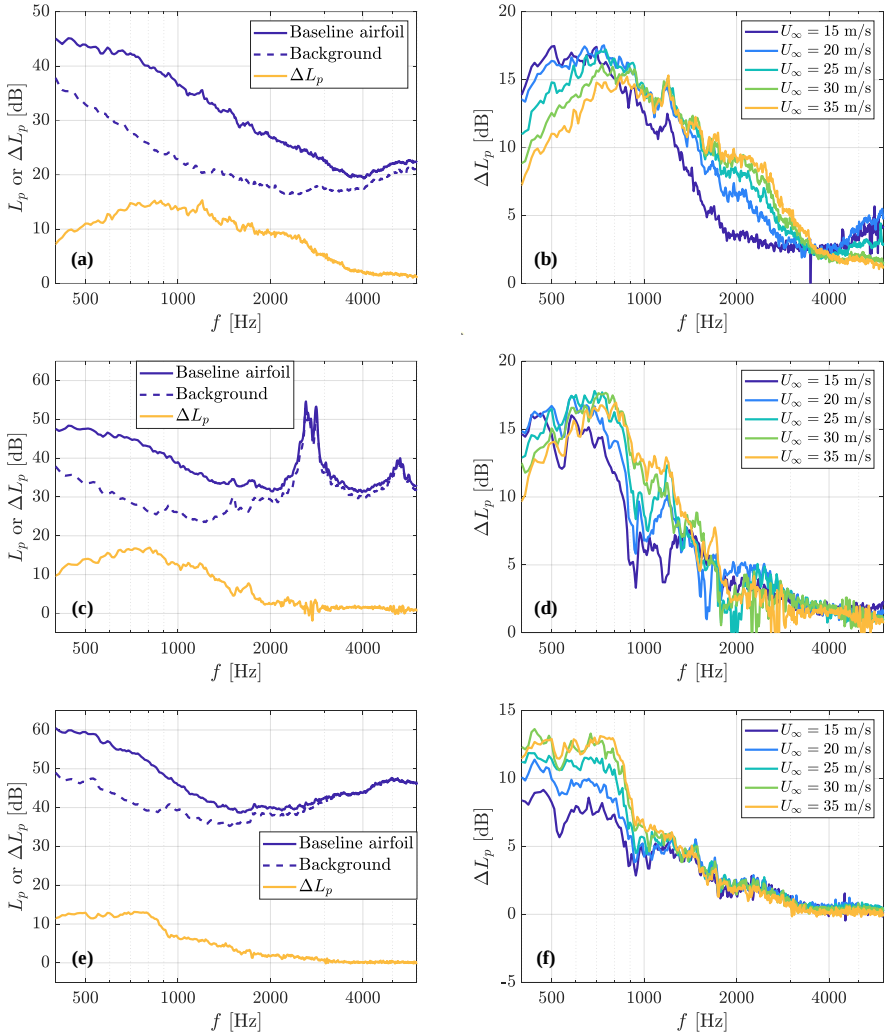

Figure 2.25: Signal-to-noise ratios for the clean and turbulent inflow cases: (a), (c) and (e) are the sound pressure levels and relative sound pressure levels at inflow velocity of 35 m/s for clean inflow, with grid #1 and grid #2 mounted, respectively; (b), (d), (f) are the relative sound pressure levels under different inflow velocities for clean inflow, with grid #1 and grid #2 mounted, respectively.

different velocities. For the clean inflows, for all the tested velocities, the relative sound pressure levels are higher than 10 dB between 500 and 1500 Hz which suggests excellent SNRs for acoustic measurements. However, when the grids were mounted, this range was reduced up to 1000 Hz, and the SNRs within 1000 Hz to 1500 Hz were reduced to 5 dB. The limitation of background noise should be considered when looking into the spectral features of the airfoil noise in the corresponding frequency bands.

2.3.5. FLOW FIELD MEASUREMENTS AND VISUALIZATIONS

To understand the physics of how damage affects the aerodynamic properties and thus how it changes the spectra of noise, flow field measurements and visualizations are also carried out in the work of this thesis.

PARTICLE IMAGE VELOCIMETRY

For trailing edge crack detection, the measurements of the velocity fields near the trailing edge and in the near wake were performed using particle image velocimetry (PIV). The setup for PIV measurements is shown in Figure 2.26(a). The seeding particles were produced by the SAFEX Twin-Fog Double Power fog generator which provided a mean droplet diameter of 1 μm (it is integrated into the wind tunnel and not shown in the figure). An EverGreen 200 laser was used as the light source. It provided a dual-pulsed beam of 532 nm wavelength with a maximum pulse frequency of 15 Hz and a maximum pulse energy of 200 mJ. The pulse frequency was set to 10 Hz and the energy was set to 55% of the maximum. The laser beam was turned into a 2 mm thick sheet by three lenses.

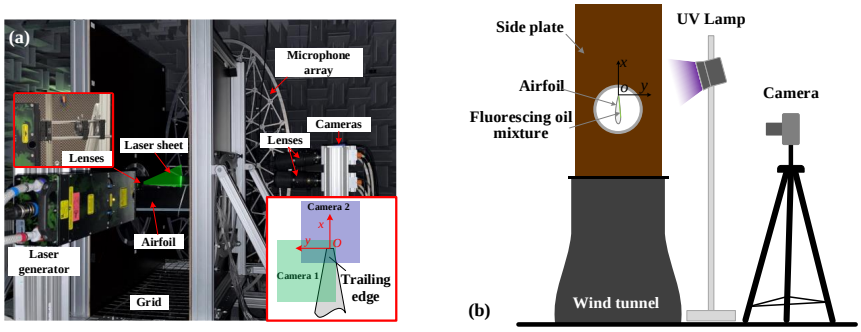

Figure 2.26: Setup of flow field measurements and visualizations; (a) PIV and (b) surface oil flow visualization.

Two LaVision sCMOS cameras were used to record the particle images. One was used to measure the velocity field and the boundary layer near the trailing edge while the other one for the near-wake velocity field. Each camera has a sensor with a size of 2560 × 2160 pixels and the pixel pitch of 6.5 μm. A Nikon NIKKOR prime lens with a focal length $f' = 200$ mm was mounted on each camera. The focus plane was adjusted to the middle span of the airfoil which was illuminated by the laser sheet. The aperture was set to $f'/8.0$ which provided the proper depth of field for this experiment. The field of view for

each camera is approximately 32mm × 27mm. The two fields of view are shown in Figure 2.26 (a) and a right-hand *xoy* coordinate system was established at the middle span of the trailing edge. The exposure time for each frame was 10 μs and the double shutter time was configured differently which leads to approximately the same particle displacement in the free stream of 210 μm (16.8 pixels) for different inflow velocities; statistics were computed by recording 300 pairs of images.

The velocity field calculation was carried out using the software LaVision DaVis 10.2. A standard multi-pass 2D cross-correlation algorithm was performed for the vector calculation. Two initial passes and two final passes were applied with deformable windows; the sizes of the windows are 128 × 128 pixels and 24 × 24 pixels, respectively, and the window overlaps are 50% and 75%, respectively. This provides a spatial resolution of 0.3 mm and a vector spacing of 0.075 mm. The uncertainty of the mean velocity is estimated as $\varepsilon_U = \sigma_U/\sqrt{N}$ and the uncertainty of the root mean square velocity is estimated as $\varepsilon_{u'} = \sigma_U/\sqrt{2(N-1)}$ [65], where $\sigma_U$is the typical maximum magnitude of the velocity fluctuations normalized by the inflow velocity ($\sigma_U \sim 20\%$ in the boundary layer in this study), and N is the number of the paired snapshots ($N = 300$ in this study). This yields the uncertainty of the mean velocity and root mean square velocity of 1.15% and 0.82%, respectively.

SURFACE OIL FLOW VISUALIZATION

To investigate how trailing edge erosion changes the boundary layer development and transition on the airfoil surface and to interpret its impact on the noise emission, a surface oil flow visualization technique [66] was applied, of which the setup is shown in Figure 2.26(b). A fluorescing oil mixture made of paraffin oil and petroleum was brushed on the airfoil. Fluorescence was excited with an ultra-violet (UV) lamp. Surface oil flow visualization can provide a qualitative visualization for the boundary layer development and transition since the oil film can be affected and changed by the shear forces and velocity gradient.

REFERENCES

[1] Y. Zhang, F. Avallone, and S. Watson. Wind turbine blade trailing edge crack detection based on airfoil aerodynamic noise: An experimental study. *Applied Acoustics* **191** (2022), 108668.

[2] Y. Zhang, F. Avallone, and S. Watson. An aeroacoustics-based approach for wind turbine blade damage detection. *Journal of Physics: Conference Series* **2265** (2022), 022088.

[3] Y. Zhang, F. Avallone, and S. Watson. Leading edge erosion detection for a wind turbine blade using far-field aerodynamic noise. *Applied Acoustics* **207** (2023), 109365.

[4] M. Lighthill. On Sound Generated Aerodynamically . I . General Theory. *Proceedings of the Royal Society of London A, Mathematical and Physical Sciences* **211** (1952), 564–587.

[5] M. Lighthill. On Sound Generated Aerodynamically . II . Turbulence as a Source of Sound. *Proceedings of the Royal Society of London A, Mathematical and Physical Sciences* **222** (1953), 1–32.

[6] N. Curle. The influence of solid boundaries upon aerodynamic sound. *Proceedings of the Royal Society of London. Series A, Mathematical and Physical Sciences* **231** (1955), 505–514.

[7] J. E. Ffowcs Williams and D. L. Hawkings. Sound generation by turbulence and surfaces in arbitrary motion. *Philosophical Transactions of the Royal Society of London. Serie A, Mathematical and Physical Sciences* **264** (1969), 321–342.

[8] S. Oerlemans. Wind turbine noise : primary noise sources (2011), 1–57.

[9] M. Ghasemian and A. Nejat. Aero-acoustics prediction of a vertical axis wind turbine using Large Eddy Simulation and acoustic analogy. *Energy* **88** (2015), 711–717.

[10] R. K. Amiet. Acoustic radiation from an airfoil in a turbulent stream. *Journal of Sound and Vibration* **41** (1975), 407–420.

[11] R. K. Amiet. Noise due to turbulent flow past a trailing edge. *Journal of Sound and Vibration* **47** (1976), 387–393.

[12] D. Kim, G. S. Lee, and C. Cheong. Inflow broadband noise from an isolated symmetric airfoil interacting with incident turbulence. *Journal of Fluids and Structures* **55** (2015), 428–450.

[13] P. D. Lysakn, D. E. Capone, and M. L. Jonson. Prediction of high frequency gust response with airfoil thickness effects. *Journal of Fluids and Structures* **39** (2013), 258–274.

[14] J. Gill, X. Zhang, and P. Joseph. Symmetric airfoil geometry effects on leading edge noise. *The Journal of the Acoustical Society of America* **134** (2013), 2669–2680.

[15] S. Pröbsting and S. Yarusevych. Laminar separation bubble development on an airfoil emitting tonal noise. *Journal of Fluid Mechanics* **780** (2015), 167–191.

[16] C. K. Tam. Discrete tones of isolated airfoils. *Journal of the Acoustical Society of America* **55** (1974), 1173–1177.

[17] H. Arbey and J. Bataille. Noise generated by airfoil profiles placed in a uniform laminar flow. *Journal of Fluid Mechanics* **134** (1983), 33–47.

[18] A. V. Dovgal, V. V. Kozlov, and A. Michalke. Laminar boundary layer separation: Instability and associated phenomena. *Progress in Aerospace Sciences* **30** (1994), 61–94.

[19] E. C. Nash, M. V. Lowson, and A. McAlpine. *Boundary-layer instability noise on aerofoils*. Vol. 382. 1999, pp. 27–61.

[20] T. P. Chong and P. Joseph. "Ladder" structure in tonal noise generated by laminar flow around an airfoil. *The Journal of the Acoustical Society of America* **131** (2012), EL461–EL467.

[21] T. F. Brooks, D. S. Pope, and M. A. Marcolini. *Airfoil self-noise and prediction*. Vol. 1218. National Aeronautics and Space Administration, 1989.

[22] T. Colonius and S. K. Lele. Computational aeroacoustics: Progress on nonlinear problems of sound generation. *Progress in Aerospace Sciences* **40** (2004), 345–416.

[23] S. Lee, L. Ayton, F. Bertagnolio, et al. Turbulent boundary layer trailing-edge noise: Theory, computation, experiment, and application. *Progress in Aerospace Sciences* **126** (2021), 100737.

[24] T. Kim and S. Lee. Aeroacoustic simulations of a blunt trailing-edge wind turbine airfoil. *Journal of Mechanical Science and Technology* **28** (2014), 1241–1249.

[25] W. Arias Ramírez and W. R. Wolf. Effects of trailing edge bluntness on airfoil tonal noise at low Reynolds numbers. *Journal of the Brazilian Society of Mechanical Sciences and Engineering* **38** (2016), 2369–2380.

[26] S. M. Hasheminejad, T. P. Chong, G. Lacagnina, et al. On the manipulation of flow and acoustic fields of a blunt trailing edge aerofoil by serrated leading edges. *The Journal of the Acoustical Society of America* **147** (2020), 3932–3947.

[27] R. L. Simpson. Turbulent boundary-layer separation. *Annual Review of Fluid Mechanics* **21** (1989), 205–34.

[28] J. M. Turner and J. W. Kim. Effect of spanwise domain size on direct numerical simulations of airfoil noise during flow separation and stall. *Physics of Fluids* **32** (2020).

[29] A. Dróżdż, P. Niegodajew, M. Romańczyk, and W. Elsner. Effect of Reynolds number on turbulent boundary layer approaching separation. *Experimental Thermal and Fluid Science* **125** (2021).

[30] S. Moreau, M. Roger, and J. Christophe. Flow features and self-noise of airfoils near stall or in stall. *15th AIAA/CEAS Aeroacoustics Conference (30th AIAA Aeroacoustics Conference)* (2009), 11–13.

[31] B. Zang, Y. D. Mayer, and M. Azarpeyvand. Experimental Investigation of Near-Field Aeroacoustic Characteristics of a Pre- and Post-Stall NACA 65-410 Airfoil. *Journal of Aerospace Engineering* **34** (2021), 1–10.

[32] G. Lacagnina, P. Chaitanya, T. Berk, et al. Mechanisms of airfoil noise near stall conditions. *Physical Review Fluids* **4** (2019), 123902.

[33] O. Fleig, M. Iida, and C. Arakawa. Wind turbine blade tip flow and noise prediction by large-eddy simulation. *Journal of Solar Energy Engineering, Transactions of the ASME* **126** (2004), 1017–1024.

[34] H. M. Slot, E. R. Gelinck, C. Rentrop, and E. Van der Heide. Leading edge erosion of coated wind turbine blades: Review of coating life models. *Renewable Energy* **80** (2015), 837–848.

[35] H. M. Slot, E. R. Gelinck, C. Rentrop, and E. Van der Heide. Leading edge erosion of coated wind turbine blades: Review of coating life models. *Renewable Energy* **80** (2015), 837–848.

[36] L. Mishnaevsky, C. B. Hasager, C. Bak, et al. Leading edge erosion of wind turbine blades: Understanding, prevention and protection. *Renewable Energy* **169** (2021), 953–969.

[37] S. Oerlemans. Detection of aeroacoustic sound sources on aircraft and wind turbines (2009), 1–173.

[38] E. Simley. Development of an acoustic array for wind turbine aeroacoustic noise analysis (2010), 166.

[39] P. Sijtsma. Phased Array Beamforming Applied to Wind Tunnel and Fly-Over Tests. *SAE Technical Papers* **2010-Octob** (2010), 17–19.

[40] R. Merino-Martínez, P. Sijtsma, A. R. Carpio, et al. Integration methods for distributed sound sources. *International Journal of Aeroacoustics* **18** (2019), 444–469.

[41] P. Sijtsma and M. Snellen. Inverse integration method for distributed sound sources. *BeBeC* (2018), 9–17.

[42] R. Merino-Martínez, A. Rubio Carpio, L. T. Lima Pereira, et al. Aeroacoustic design and characterization of the 3D-printed, open-jet, anechoic wind tunnel of Delft University of Technology. *Applied Acoustics* **170** (2020).

[43] P. Sijtsma. CLEAN based on spatial source coherence. *13th AIAA/CEAS Aeroacoustics Conference (28th AIAA Aeroacoustics Conference)* **6** (2007), 357–374.

[44] P. Sijtsma, R. Merino-Martinez, A. M. Malgoezar, and M. Snellen. High-resolution CLEAN-SC: Theory and experimental validation. *International Journal of Aeroacoustics* **16** (2017), 274–298.

[45] Rayleigh. XXXI. Investigations in optics, with special reference to the spectroscope. *The London, Edinburgh, and Dublin Philosophical Magazine and Journal of Science* **8** (1879), 261–274.

[46] R. C. Ramachandran, G. Raman, and R. P. Dougherty. Wind turbine noise measurement using a compact microphone array with advanced deconvolution algorithms. *Journal of Sound and Vibration* **333** (2014), 3058–3080.

[47] C. J. Bahr and W. C. Horne. Advanced background subtraction applied to aeroacoustic wind tunnel testing. *21st AIAA/CEAS Aeroacoustics Conference* (2015).

[48] A. Sareen, C. A. Sapre, and M. S. Selig. Effects of leading edge erosion on wind turbine blade performance. *Wind Energy* **17** (2014), 1531–1542.

[49] A. Rubio Carpio, F. Avallone, D. Ragni, M. Snellen, and S. Van Der Zwaag. Mechanisms of broadband noise generation on metal foam edges. *Physics of Fluids* **31** (2019).

[50] T. Kurian and J. H. Fransson. Grid-generated turbulence revisited. *Fluid Dynamics Research* **41** (2009).

[51] J. Groth and A. V. Johansson. Turbulence reduction by screens. *Journal of Fluid Mechanics* **197** (1988), 139–155.

[52] R. Tresso and D. R. Munoz. Homogeneous, isotropic flow in grid generated turbulence. *Journal of Fluids Engineering, Transactions of the ASME* **122** (2000), 51–56.

[53] R. J. Barthelmie, S. T. Frandsen, M. N. Nielsen, et al. Modelling and measurements of power losses and turbulence intensity in wind turbine wakes at middelgrunden offshore wind farm. *Wind Energy* **10** (2007), 517–528.

[54] A.N.Kolmogorov. A refinement of previous hypotheses concerning the local structure. *Journal of Fluid Mechanics* (1962), 82–85.

[55] G. C. Lam and R. C. Leung. Aeroacoustics of NACA 0018 airfoil with a cavity. *AIAA Journal* **56** (2018), 4775–4786.

[56] S. Luesutthiviboon, D. Ragni, F. Avallone, and M. Snellen. An alternative permeable topology design space for trailing-edge noise attenuation. *International Journal of Aeroacoustics* (2021).

[57] W. A. Timmer. Two-dimensional low-Reynolds number wind tunnel results for airfoil NACA 0018. *Wind Engineering* **32** (2008), 525–537.

[58] M. S. Boutilier and S. Yarusevych. Parametric study of separation and transition characteristics over an airfoil at low Reynolds numbers. *Experiments in Fluids* **52** (2012), 1491–1506.

[59] A. M. G. Lopes and J. A. V. Alé. Numerical simulation of the aerodynamic characteristics of the NACA 0018 airfoil at medium range Reynolds number. *Wind Engineering* **46** (2022), 1675–1688.

[60] W. A. Timmer and R. P. Van Rooij. Summary of the Delft University wind turbine dedicated airfoils. *Journal of Solar Energy Engineering, Transactions of the ASME* **125** (2003), 488–496.

[61] B. Moghadassian and A. Sharma. Designing wind turbine rotor blades to enhance energy capture in turbine arrays. *Renewable Energy* **148** (2020), 651–664.

[62] L. A. Joseph, A. Borgoltz, and W. Devenport. Infrared thermography for detection of laminar-turbulent transition in low—speed wind tunnel testing. *Experiments in Fluids* **57** (2016), 1–13.

[63] M. Drela. "XFOIL: An analysis and design system for low Reynolds number airfoils". In: *Low Reynolds number aerodynamics*. Springer, 1989, pp. 1–12.

[64] F. Hutcheson and T. Brooks. Noise radiation from single and multiple rod configurations. *International Journal of Aeroacoustics* **11** (2012), 291–334.

[65] Q. Ye, F. F. Schrijer, and F. Scarano. Boundary layer transition mechanisms behind a micro-ramp. *Journal of Fluid Mechanics* **793** (2016), 132–161.

[66] J. Serpieri and M. Kotsonis. Flow visualization of swept wing boundary layer transition. *10th Pacific Symposium on Flow Visualization and Image Processing* (2015), 15–18.

3

TRAILING EDGE CRACK DETECTION

In this chapter, the trailing edge crack detection is experimentally investigated based on the measurement of airfoil aerodynamic noise. Experiments are conducted at different inflow velocities, inflow turbulence intensities and angles of attack. Far-field noise scattered from the airfoil is measured by means of a microphone array. The spectral differences in sound pressure level between the damaged cases and the baseline (without any damage) are compared. The results show that it is possible to detect the trailing edge crack for the clean and low turbulence intensity cases. The crack-induced tonal noise appears at trailing-edge thickness-based Strouhal number, St_h, approximatively equal to 0.1. However, at higher angles of attack or under conditions of high turbulence intensity (e.g., ~ 7.1%), the amplitude of the tonal peak diminishes suggesting that complementary measurements or longer acquisition time to remove inflow turbulence effects are needed to monitor trailing edge cracks.

Parts of this chapter have been published in *Applied Acoustics* **191** (2022) [1].

3.1. INTRODUCTION

The decarbonization of the energy system is vital to mitigate the potentially damaging effects of climate change. Wind energy can make a valuable contribution and has seen a huge expansion in recent years [2–5]. For example, in 2020, wind farms in Europe produced 458 TWh, covering 16.4% of electricity demand [6]. Globally, 93 GW of new installed capacity resulted in a 53% growth rate with respect to 2019 [7]. Because of the harsh environment particularly for offshore installations, wind turbines are subject to various types of damage such as structural [8, 9], mechanical [10–12] and electrical equipment malfunction [13, 14]. Wind turbine blades, amongst other components, are subject to mechanical damage that can affect energy production [15]. A statistical analysis, focusing on failures in Swedish wind farms during 1997-2005, indicated that blade damage represented 13.4% of all failures while gearboxes and generators contributed 9.8% and 5.5%, respectively [16]. Other studies [15, 17, 18] also report similar conclusions.

The foregoing discussion highlights the need for effective condition monitoring to prevent serious wind turbine blade damage. At present, blade monitoring is performed primarily by visual inspection and regular planned maintenance that require the wind turbines to be shut down. Therefore, the development of real-time non-contact health monitoring techniques is of some interest. Health monitoring techniques can be classified as contact and non-contact. Contact techniques are usually based on vibration [19–22] or strain [23–25] measurements with sensors installed on the blades. Even if direct measurements on the blade guarantee high quality data, information about the damage is reliable only close to the sensor location because of the high damping coefficient of the blades which are made of fiberglass composite material. Furthermore, although sensors can be retrofitted to the blades, this is cumbersome, adds cost, is not always reliable. Ideally, sensors should be embedded in the blade during manufacturing. On the other hand, non-contact approaches rely on measurements acquired with remote systems such as infrared thermography, lasers, microphones, or a combination of these. Infrared thermography can be used for blade damage detection [26, 27], but it is limited by its spatial resolution and dynamic range. Another damage detection approach is based on lasers [28–30], but to improve laser measurement performance, a pre-treatment for the target surface is necessary. Acoustic measurements have also the potential to be used; however, until recently, mainly vibro-acoustic approaches have been adopted [31–34]. A few studies in the literature focus on the measurement of audible sound (20 Hz to 20 kHz) using microphones. The first approach [35, 36] works by mounting audio speakers inside a wind turbine blade and measuring the sound radiated from the blade to identify damage within the structure (e.g., cracks, edge splits or holes. Another approach [37–40] is based on the use of microphones to detect trends, shifts, or spikes in the sound pressure level within the blade cavity. This approach mainly relies on the measurements of the acoustic pressure responses of the flow-induced noise within the blade cavity. On the other hand, it is potentially possible to use aerodynamic noise generated by the wind turbine blades, also known as airfoil self-noise [41], as a source of information for blades health monitoring [42–45]. In this case, the microphones are located outside the blade and the internal speakers are not needed, thus simplifying the detection method.

In recent years, aerodynamic noise from wind turbines has mainly been investigated

because it can limit the installation of onshore wind farms from a noise nuisance perspective [46, 47]. As a consequence, the focus has been on its reduction [48, 49]. However, in offshore applications, where noise emissions are less of a problem, it is possible to use airfoil self-noise as a source of information for damage detection. As a matter of fact, leading edge erosion or icing will affect boundary layer transition over the blades thus causing a variation of the turbulent boundary layer integral quantities at the trailing edge [50]. There will be a variation of the turbulent boundary layer trailing edge noise and, additional noise will be scattered at the roughness location. These noise sources will alter the broadband component of the noise in the low and high frequency ranges, respectively. Other damage, such as trailing edge delamination and cracks, may result in a thicker trailing edge. When the thickness of the trailing edge is larger than 0.3 times the boundary layer displacement thickness, δ^*, at the trailing edge, vortex shedding appears which results in tonal noise in the far-field spectrum [51–53].

The variation in the far-field spectrum can be an indication of damage. However, in real working conditions, the blade is subject to inflow turbulence with variable length scales. This affects the development of the flow over the blade and introduces an additional source of noise, called leading edge impingement noise [49, 54], which can alter the far-field noise spectrum and potentially hide the damage-induced spectral features. While previous publications [42–45] have mainly focused on the development of data-driven methods by means of airfoil self-noise for damage detection, we aim at providing a physics-based interpretation of the results, and we extend the previous studies by including a turbulent inflow. In this regard, trailing edge crack detection is investigated due to the presence of a tonal noise component in the spectrum.

The rest of this chapter is organized as follows: In Section 3.2, the details of the experimental setup are described and the test conditions of the experiment are presented. In Section 3.3, the results of acoustic measurements are shown and the related physics affecting the acoustic characteristics are discussed. Finally, Section 3.4 summarizes the main conclusions from the experiments.

3.2. EXPERIMENTAL SETUP AND TEST CONDITIONS

3.2.1. EXPERIMENTAL SETUP

WIND TUNNEL AND TEST MODELS

The experiment was carried out in the anechoic vertical open-jet tunnel (A-tunnel) of Delft University of Technology. The wind tunnel has a contraction ratio of 15:1 and the rectangular test section outlet is 40 cm × 70 cm. The operating free-stream velocity of the wind tunnel can be up to 45 m/s with turbulence intensity below 0.1% of the free-stream velocity for the entire range of operating velocities. The uniformity of the free-stream velocity distribution across the test section is within 0.5% with respect to velocity at the center of the nozzle [55].

The test model is a NACA 0018 airfoil, which is manufactured from solid aluminum using computer numerical control (CNC) machining (surface roughness: 0.05 mm), with chord length C of 200 mm and span length L of 400 mm (the span-chord ratio $L/C = 2$) as shown in Figure 3.1(a). The airfoil model has exchangeable trailing edges to allow the testing of different crack configurations. Since there is no model reported in the litera-

ture describing how to model a trailing edge crack of the wind turbine blade, in this thesis, the assumption is taken that when a crack occurs there is only a minor shape change resulting in a thickness increase at the trailing edge. To investigate different damage levels, four changeable trailing edge parts with a rectangle crack are designed. The crack widths W are 0.2, 0.5, 1.0 and 2.0 mm, respectively, and the sizes of the crack depth D are based on the crack depth-width ratio, D/W, of 1.5. As a consequence, the thicknesses at the trailing edge, $h = W + h_{\text{Baseline}}$ (h_{Baseline} = 0.76mm is the trailing edge thickness of the standard NACA 0018 airfoil with the chord length of 200 mm), are 0.96, 1.26, 1.76 and 2.76 mm, respectively. The detailed dimensions of the trailing edge parts are shown in Table 3.1. In Figure 3.1(b), an example of the trailing edge with a crack of 0.2 mm is shown. Since the Reynolds numbers at which the experiments were carried out were lower than those likely to be observed in real operating conditions for a full-scale blade, a transition to turbulent flow over the airfoil was forced with two tripping devices located at 20% of the chord at both the pressure and suction side. The tripping device was made of a piece of tape (12 mm width) and sand particles (0.84 mm height) which were distributed randomly with average density of 20 particles per square centimeter. The tested airfoil was installed between two 1.2 m long side plates to guarantee a two-dimensional flow. The leading edge of the airfoil was located at 0.3 m from the nozzle exit. The sketch of the experimental setup is shown in Figure 3.2.

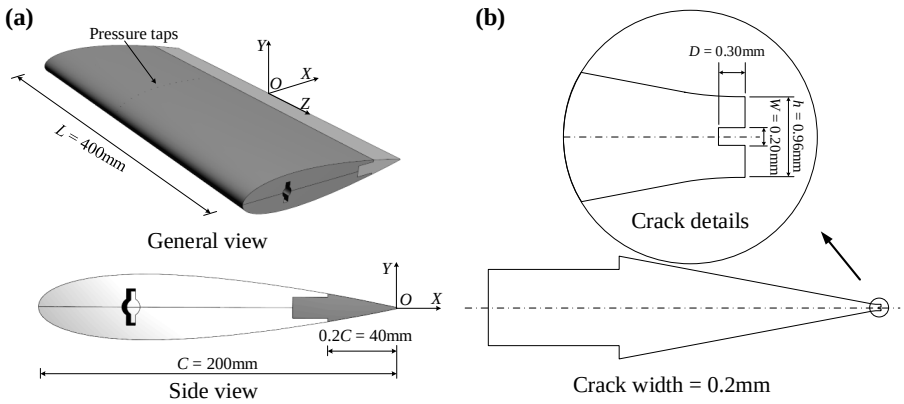

Figure 3.1: Experimental setup.

For convenience, two coordinate systems (*O-XYZ* and *o-xyz*) are used both taking the geometric center of the trailing edge as an origin. For the *O-XYZ* coordinate system, shown in Figure 3.1(a), the X-axis is aligned with the chord while, for the *o-xyz* coordinate system, shown in Figure 3.2, the x-axis is aligned with the direction of the free-stream velocity.

The geometrical angle of attack (AoA) α of the airfoil was set using a stepper motor. The effective AoA, α^*, of the airfoil is smaller than the geometrical angle due to the nature of the flow in an open test section [41]. To obtain the effective AoA, surface pressure measurements were acquired and the results were compared with XFOIL [56]. A total of

Table 3.1: The dimensions of the trailing edge parts.

Trailing edge No.	0	1	2	3	4
W (mm)	0	0.20	0.50	1.00	2.00
D (mm)	0	0.30	0.75	1.50	3.00
h (mm)	0.76	0.96	1.26	1.76	2.76
W/C(%)	0	0.10	0.25	0.50	1.00
D/C(%)	0	0.15	0.375	0.75	1.50
h/C(%)	0.38	0.48	0.63	0.88	1.38

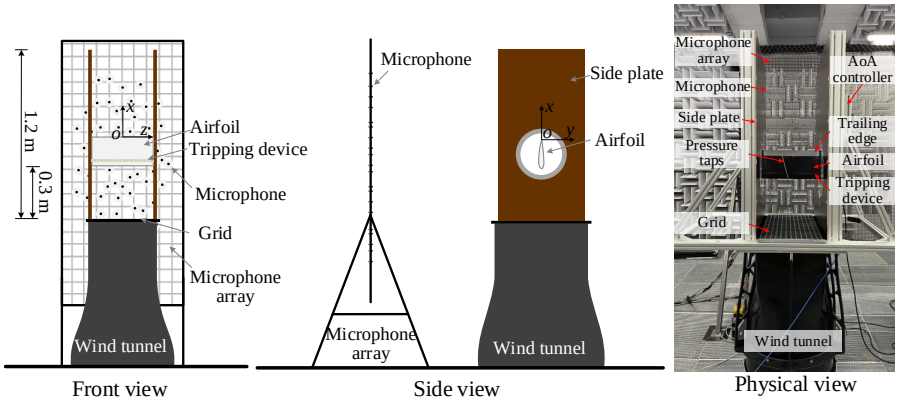

Figure 3.2: A sketch of the experimental setup.

15 pressure taps with a diameter of 0.4 mm distributed in the range $-0.99 \leq X/C \leq -0.34$ at both pressure and suction sides were used for this purpose. The pressure taps are tilted 15° with respect to the centerline to avoid near wake interference from the downstream taps. The pressure taps were connected to pressure transducers with a measurable range of ±2.5 kPa and an accuracy of 12.5 Pa. Pressure data were recorded for a period of 2 s with a sampling frequency of 100 Hz and then averaged. The coefficient of lift, C_l, at different angles of attack can be obtained by integrating the surface pressure data. The detailed calibration process is reported in Chapter 2.

The measured C_l at different values of α is shown in Figure 3.3. For comparison, the calculated values of C_l from XFOIL are also shown. By fitting straight lines to these two sets of points, a correction factor can be derived from the ratio of the effective to geometrical angle of attack, $\eta = \alpha^*/\alpha$, which in this experiment is $\eta = 0.054/0.1130 = 0.48$.

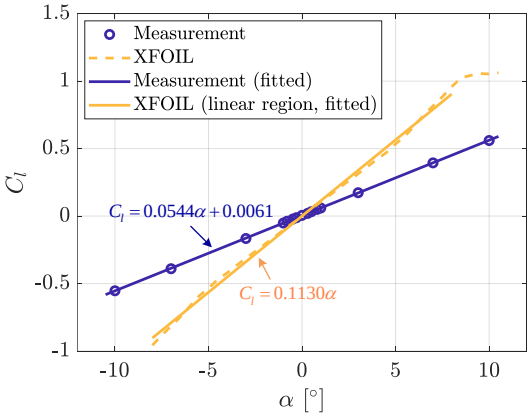

Figure 3.3: The relationships between C_l, α and α^* from the measured data and XFOIL.

PHASED MICROPHONE ARRAY AND BEAMFORMING

One single microphone can only measure the overall sound level, which has the limitation of not distinguishing the locations of sound sources. Since in the experiment, the noise sources of the trailing edge are of interest, a microphone array was adopted. The microphone array consists of 64 *G.R.A.S. 40PH* free-field microphones with a frequency response within ±1 dB from 50 Hz to 5 kHz and within ±2 dB from 5 to 20 kHz allowing a maximum output of 135 dB (reference pressure 20 μPa). The microphones were distributed as a 2-D planar array which was parallel to the stream-wise direction. The microphone array was located at 1 m from the airfoil trailing edge as shown in Figure 3.2 and the distribution of the microphones in the array is shown in Figure 3.4.

The sampling frequency f_S of each microphone was 51.2 kHz and for each test case, the signal was recorded for a length of 20 s. The signal from each microphone was separated into time blocks with 5120 samples (Δt = 10 ms) for each Fourier transform and spectral average. This provides a frequency resolution of 10 Hz thus making

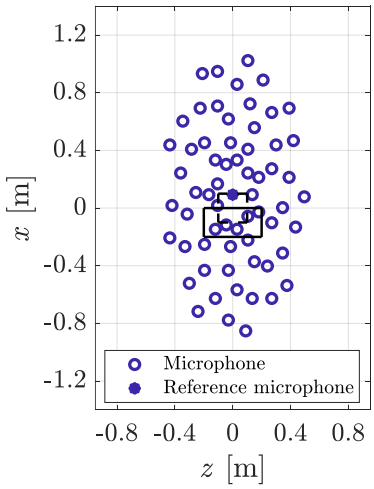

Figure 3.4: The distribution of the microphones in the array. The solid box is the projection of the airfoil onto the array plane with an AoA of 0° and the dashed box is the corresponding integration region for the sound power.

it possible to distinguish the narrowband characteristics of the signal. Furthermore, to avoid energy leakage of the Fourier transform, a Hanning weighting function with 50% data overlap was adopted. Conventional frequency domain beamforming [57, 58] was performed on a square grid (scan plane) on the *xoz* plane over an area defined by: $-0.5\text{m} \leq x + x_{\text{Ref}} \leq 0.5\text{m}$ and $-0.5\text{m} \leq z + z_{\text{Ref}} \leq 0.5\text{m}$ with a space between the grid points of 20 mm where $(x_{\text{Ref}}, z_{\text{Ref}})$ is the reference position of the central microphone (solid blue point in Figure 3.4). To separate the trailing edge noise from other undesired sound sources, a region on the scan plane over an area defined by: $-1.0\text{m} \leq x \leq 1.0\text{m}$ and $-1.0\text{m} \leq z \leq 1.0\text{m}$ was chosen for integration in which all the relevant noise sources from the trailing edge were included [59, 60]. The integration region of the sound power and its relative position with respect to the airfoil are shown in Figure 3.4.

TURBULENCE GENERATING GRIDS

As the flow of the wind tunnel is laminar, to simulate the turbulent conditions expected in a realistic operating environment and to further verify the feasibility of the approach under such turbulent conditions, two grids were used for the generation of turbulence [61–64]. Turbulence downstream of the grid was characterized using hotwire anemometry. Data were sampled at a frequency of 51.2 kHz and for each measurement, data were recorded for 20 s. The characterization was carried out without the airfoil installed in the test section, which is detailed reported in Chapter 2. The turbulence intensity, I, and integral length scale Λ_f of the inflow, when the grids were mounted, are shown in Table 3.2.

Table 3.2: Turbulence intensity and integral length scale of the flow with grid mounted.

Grid No.	Turbulence intensity (%)	Turbulence integral length scale (mm)
1	4.0	7.9
2	7.1	10.2

3.2.2. TEST CONDITIONS

MEAN FLOW VELOCITY

Experiments were performed at five inflow velocities U_∞ as reported in Table 3.3 together with the corresponding chord-length-based Reynolds numbers ($Re_C = U_\infty C/\nu$, ν - kinematic viscosity).

Table 3.3: Test conditions of mean flow velocities and Reynolds numbers.

No.	1	2	3	4	5
U_∞ (m/s)	15	20	25	30	35
Re_C	2.0×10^5	2.7×10^5	3.4×10^5	4.1×10^5	4.7×10^5

ANGLE OF ATTACK

A change in AoA of the airfoil leads to a change of the boundary layer properties both at the pressure and suction sides, which can have an effect on far-field noise. In the experiment, nine different values of AoA were tested. Because the microphone array was located on one side of the airfoil, the conditions with non-zero AoA were tested for both positive and negative values. A positive AoA is defined as the trailing edge rotated away from the microphone array. The corresponding effective AoA, α^*, is determined by the ratio, $\eta = \alpha^*/\alpha$, mentioned previously in this section. Table 3.4 shows both the geometrical and effective AoA values.

Table 3.4: The angles of attack tested in the experiment.

No.	1	2	3	4	5	6	7	8	9
α (°)	-15	-10	-5	-3	0	3	5	10	15
α^* (°)	-7.21	-4.81	-2.40	-1.44	0	1.44	2.40	4.81	7.21

3.3. RESULTS AND DISCUSSION

3.3.1. FAR-FIELD ACOUSTIC MEASUREMENTS

The metric generally adopted for acoustic measurement is the sound pressure level (SPL). Integration within a specific bandwidth is also performed, for example, a nar-

row band (10 Hz, bands of SPL spectra in this work) or one-third octave band (bands of beamforming sound maps in this work), which is defined as:

$$L_p = 10\lg\left(\frac{p'^2}{p_0^2}\right) \tag{3.1}$$

where p' is the root mean square sound pressure fluctuations and p_0 is the reference pressure, 20 μPa in air.

As mentioned in Section 3.2, a phased microphone array was used for the far-field noise measurement. Figure 3.5 shows an example of the beamforming maps for the damaged cases and the baseline (0 mm crack size) with the airfoil at an AoA of 0° and mean flow velocity of 35 m/s (clean inflow condition). The one-third octave center frequency for the beamforming map is selected at 1250 Hz, which is integrated between 1130 Hz and 1410 Hz. The beamforming maps clearly show the sound levels at different locations. In this frequency band, the noise scattered from the trailing edges is predominant. Moreover, when comparing these beamforming maps, there is a decay trend in sound levels at the trailing edge for the baseline and = 0.2, 0.5, 1.0 mm cases, with respect to the beamforming map for the 2.0 mm width crack.

3.3.2. SPECTRAL FEATURES

The sound power is integrated within a 200 mm × 200 mm region centered at the trailing edge midpoint (dashed boxes in Figure 3.4) and normalized by the total power of a unit monopole source within this region. This is referred to a sound power integration (SPI) technique which gives a total sound level within the given integrated region as mentioned in Chapter 2 and Section 3.2 of this chapter.

Figure 3.6(a) shows the integrated spectra L_p for the four damaged cases, as well as the baseline, with a frequency resolution of 10 Hz under the clean flow condition with a flow velocity of 35 m/s and AoA of 0°. The case with the 2.0 mm crack shows a significant tonal peak (~3dB) in the L_p spectrum at around 1330 Hz, but for smaller crack cases, the peaks are not significant but present as broadband humps. Moreover, with the increase in crack width, the peak or hump shifts to a lower frequency and the amplitude increases, while the broadband contributions in the spectra decrease. This is because, for a blunter trailing edge, more coherent vortex structures are shed, thus resulting in a stronger tonal peak [65, 66]. Figure 3.6(b) shows the corresponding relative SPL compared with the baseline case, i.e., $\Delta L_p = L_p - L_{p,\text{Baseline}}$. The ΔL_p spectra provide a simple and direct comparison with the baseline case.

3.3.3. EFFECTS OF TEST CONDITIONS

INFLOW MEAN FLOW VELOCITY

In Figure 3.7(a), the SPL for the 2.0 mm crack case, with an AoA of 0° and varying laminar inflow velocities is shown. As expected, the SPL increases with increasing free-stream velocity, and as the velocity increases, the spectral peak shifts to the higher frequencies. Figure 3.7(b) shows the relationship between the overall sound pressure level (OSPL, integrated from 200 Hz to 8000 Hz) and mean flow velocity. A fit to the points (dashed line) gives an OSPL which varies as a power of 4.82 to the mean flow velocity, which is in line

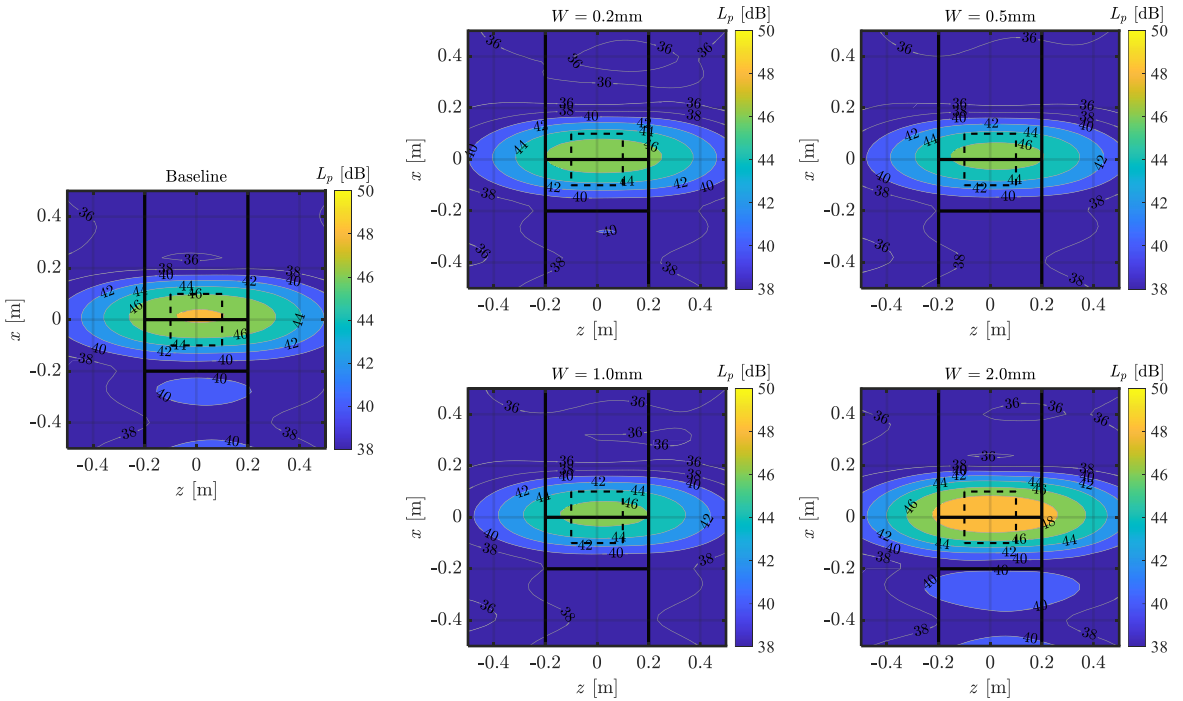

Figure 3.5: Beamforming maps of sound pressure level with the one-third octave center frequency of 1250 Hz for the cases with a mean flow velocity of 35 m/s (clean inflow condition) and AoA of 0°: the crack widths, W, are 0 (baseline), 0.2, 0.5, 1.0, and 2.0 mm.

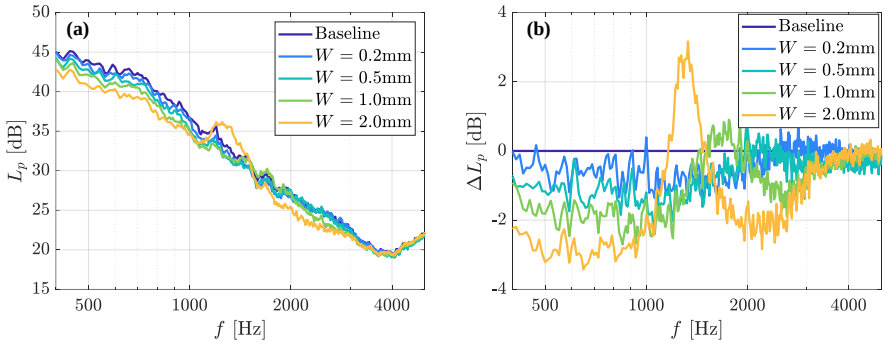

Figure 3.6: Spectra of L_p (frequency resolution of 10 Hz) within the integrated region of the case with the mean flow velocity of 35 m/s and AoA of 0° ; (b) corresponding spectra of ΔL_p.

with previous theoretical and numerical research for a sharp trailing edge [41, 67, 68] where a power of 5 is suggested (solid line in Figure 3.7(b)). Figure 3.7(c) shows the relationship between the frequency where the sound pressure level peaks (f_{peak}), and the mean flow velocity. A fit to the data shows a linear relationship, which is also found in previous studies [51, 69]. This result confirms that the measurements in this study are reliable.

The data are further analyzed as a function of the trailing-edge-thickness-based Strouhal number, $St_h = fh/U_\infty$, to scale the spectra, as suggested in [41, 53, 57]. Figure 3.8(a) shows ΔL_p as a function of St_h for the 2.0mm damage case for all flow velocities. All the curves collapse to give a peak at a St_h equal to 0.1 which is in agreement with previous results [41, 53, 57, 70]. The mean flow velocity does not significantly affect the amplitude of this peak. Figure 3.8(b) shows ΔL_p as a function of St_h for the different damage cases with AoA equal to 0°. As the crack becomes smaller, the peak broadens and the location of the peak shifts to a value of St_h smaller than 0.1.

INFLOW TURBULENCE CONDITIONS

Figure 3.9(a) shows the background noise with the grid installed at an inflow velocity of 35 m/s. For grid #1, in the lower frequency region, the background noise almost coincides with the no grid case; while at the higher frequencies, there is an increase of the broadband component and the appearance of tonal peaks at 2600 Hz and 5200 Hz. These tones are caused by the grid as demonstrated by the fact that the Strouhal number based on the grid beam diameter, $St_d = fd/U_\infty$, at which they are shed is approximately equal to 0.2 [71], as shown in Figure 3.9(b). However, in this experiment, those tonal peaks due to the rod beams of grid #1 are at a higher frequency compared with the characteristic tones related to the blunt trailing edge noise. This means at the low frequency region the data are still reliable. In contrast to grid #1, in Figure 3.9(a), grid #2 does not show significant tonal peaks but only broadband background noise.

Figure 3.10 shows the sound pressure level spectra for different crack sizes with an AoA of 0° and a mean flow velocity of 35 m/s when grid #1 or grid #2 is mounted. Figure

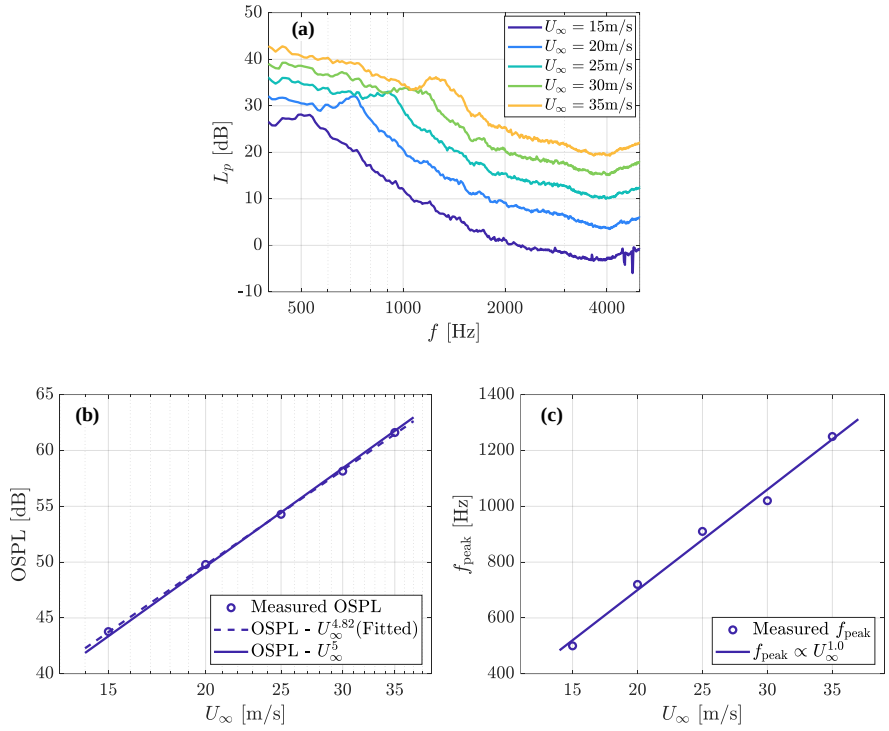

Figure 3.7: (a) The SPL of the cases with 2.0 mm crack testing at the AoA of under different mean flow velocities (15, 20, 25, 30, 35 m/s); (b) the relationships between the OSPL and mean flow velocity; (c) corresponding relationships between the frequency of spectral peaks and mean flow velocity.

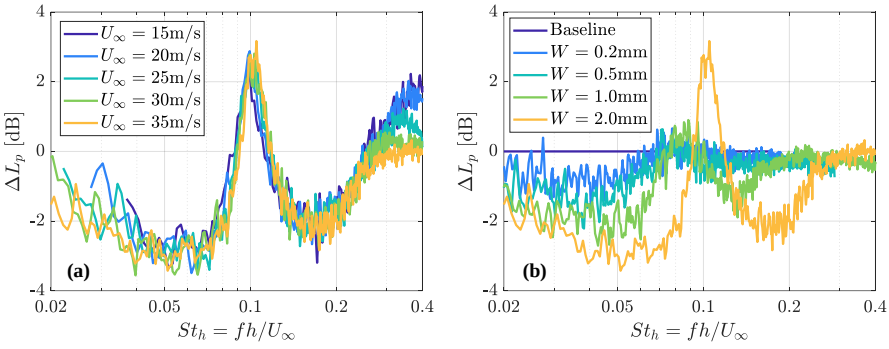

Figure 3.8: The relationships between ΔL_p and St_h with AoA of 0°: (a) under different mean flow velocities when crack width is 2.0 mm; and (b) under different crack sizes when mean flow velocity is 35 m/s.

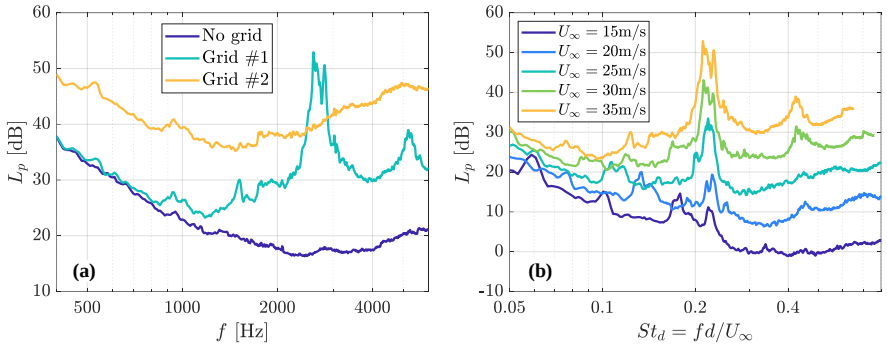

Figure 3.9: Spectra of SPL at the integrated region when the airfoil is removed: (a) for a mean flow velocity of 35 m/s and (b) for different mean flow velocities when grid #1 is mounted.

3.11 shows the corresponding relative SPL, ΔL_p, as a function of St_h. For grid #1, for which the turbulence intensity is ~ 4%, when the crack size is small, i.e., 0.2, 0.5 and 1.0 mm, the spectral differences ΔL_p are not easy to distinguish. When the damage level becomes larger, i.e., 2.0 mm, the spectra of both L_p and ΔL_p show similar trends as the case with clean flow under the same test conditions (shown in Figure 3.6(a) and Figure 3.8(b)), but with lower amplitude. However, when grid #2 is mounted and the inflow turbulence intensity becomes higher (~7.1%), shows very little difference between the different crack cases indicating that the sound characteristics due to the crack (bluntness of trailing edge) cannot be distinguished anymore.

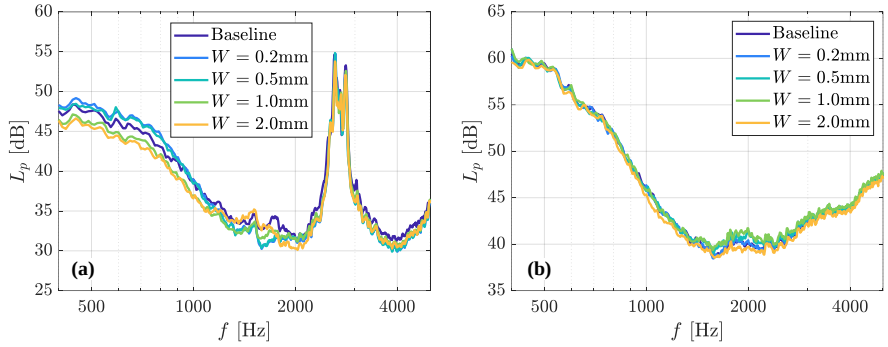

Figure 3.10: SPL spectra for different in-flow turbulence conditions when the mean flow velocity is 35 m/s and airfoil AoA is 0°: (a) turbulence generated by grid #1 and (b) turbulence generated by grid #2.

Concerning the sensitivity to the damage when the turbulence condition changes, Figure 3.12 shows the spectra of ΔL_p against St_h for the 2.0 mm crack case for these two turbulence conditions. When turbulence is generated by grid #1, the tonal peaks are still

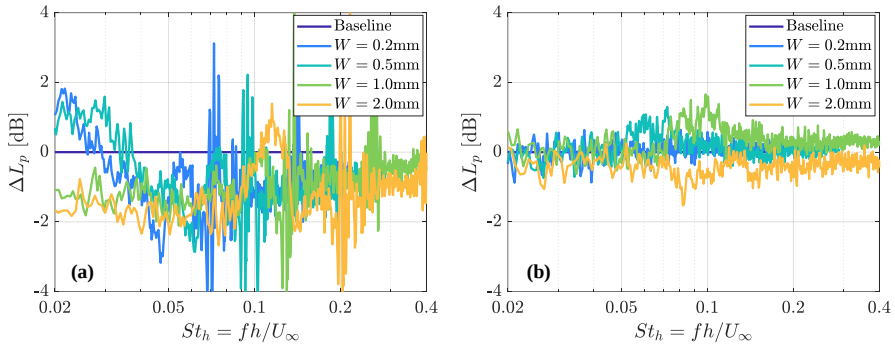

Figure 3.11: ΔL_p spectra against St_h for different inflow turbulence conditions when the mean flow velocity is 35 m/s and airfoil AoA is 0°: turbulence generated by grid #1 and (b) turbulence generated by grid #2.

distinguishable and the locations of the peaks shift slightly to a value of St_h larger than 0.1, while with grid #2, no significant peaks are evident. Compared with the clean flow seen in Figure 3.8(a), the amplitude of the tonal peaks clearly diminishes with increasing turbulence intensity.

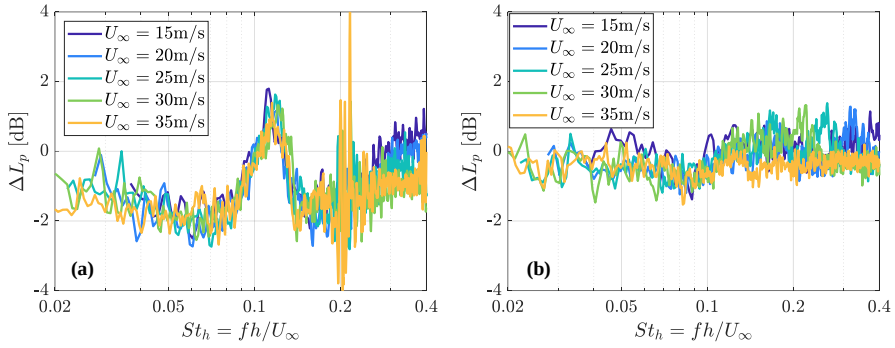

Figure 3.12: ΔL_p spectra against St_h for the 2.0 mm crack case for two turbulence conditions: (a) with grid #1 and (b) with grid #2.

AIRFOIL ANGLE OF ATTACK

Because of the change in the AoA, the boundary layer both on the pressure and suction side changes; it becomes larger on the suction side and smaller on the pressure side thus affecting vortex formation and its roll-up and, consequently affecting blunt trailing edge vortex shedding noise. Figure 3.13 shows the L_p spectra for the baseline and 2.0 mm crack cases at different angles of attack. The mean flow velocity is set at 35 m/s and the inflow is laminar. Since the acoustic array is always at the same position with

respect to the test section, the positive AoA is indicated the sound is measured looking at the suction side while the opposite is the case for the negative AoA. For a positive AoA, the spectra of the SPL in the lower frequency range, $f < 600$ Hz, show an increase with increasing AoA, while at the higher frequencies, $f > 600$ Hz, the trend is reversed. This is because the boundary layer is thicker at the suction side increasing the angle of the suction side and there is a redistribution of the energy in the turbulent flow.

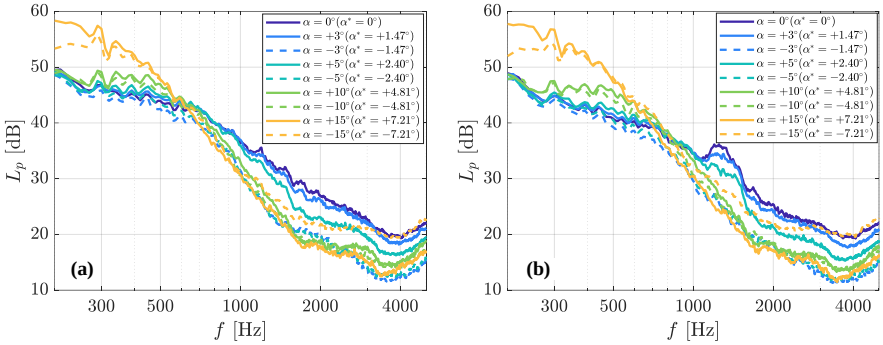

Figure 3.13: SPL with a mean flow velocity of 35 m/s at different AoA values when the flow is clean: (a) baseline, (b) crack width of 2.0 mm.

Figure 3.14(a) and (b) show ΔL_p for the 2.0 mm crack case when the flow is clean for low and high angles of attack, respectively. The peaks caused by the cracks can be found for AoAs up to ±5°. At higher AoAs, i.e., ±10° and ±15°, the boundary layer on the suction side becomes thicker and the ratio h/δ^* is no longer over the threshold value of 0.3 [51–53], and no tonal peak can be seen. Furthermore, at a higher AoA, the asymmetry between the pressure and suction side may affect the vortex shedding.

The results for turbulent inflow conditions are shown in Figure 3.14(c-f). It can be seen that the tonal peak is no longer present for the highest turbulence intensity condition when grid #2 is mounted, thus emphasizing the fact that turbulent inflow conditions might affect the ability to detect cracks from the spectra of SPL alone.

3.4. SUMMARY

In this chapter, an experimental study focusing on the potential for wind turbine blade trailing edge crack monitoring using airfoil aerodynamic noise was presented. The experimental results showed that it is possible to detect features of the tonal noise caused by the presence of a crack, for clean or low turbulent inflow conditions at moderate angles of attack. As might be expected, larger cracks show more distinct tonal features. However, a turbulent inflow reduces the intensity of the tonal noise caused by the blunt trailing edge. In this work, if the intensity of the turbulent inflow fluctuations is higher than 7.1% of the free stream velocity, then the blunt trailing edge noise can no longer be detected. By increasing the AoA, the intensity of blunt trailing edge noise decreases and eventually the cracks are no longer detectable.

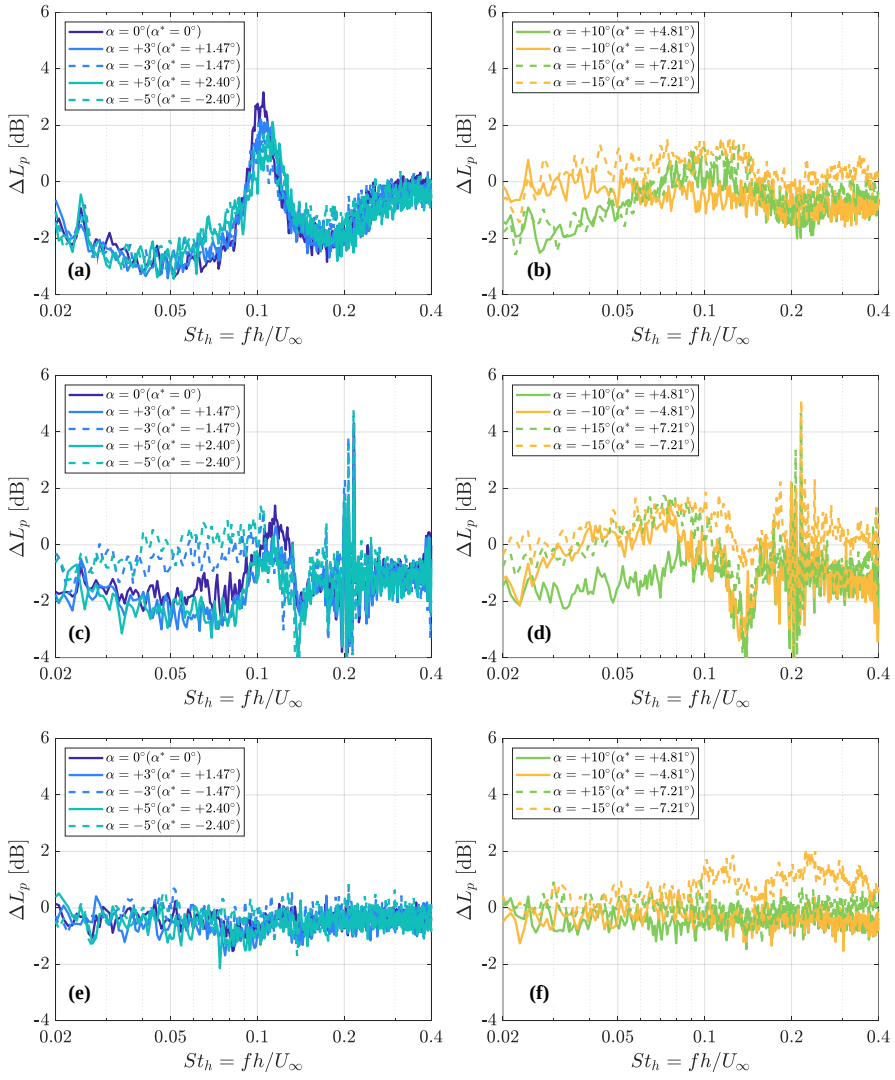

Figure 3.14: ΔL_p for the 2.0 mm crack case for different AoA values when mean flow velocity is 35 m/s: (a) no grid, low AoA; (b) no grid, high AoA; (c) grid #1, low AoA; (d) grid #1, high AoA; (e) grid #2, low AoA; and (f) grid #2, high AoA.

It can be concluded that it is potentially possible to use airfoil self-noise for trailing edge blade health monitoring, but under certain conditions. It is important to point out that the effect of turbulent inflow could be mitigated by a longer data acquisition time. In addition, a priori knowledge of the boundary layer properties over the airfoil at different radial locations would be required to predict the minimum crack size that can be measured.

Furthermore, the experiments performed have been made under ideal controlled conditions for a stationary airfoil. Clearly, significant further work would be required to assess the efficacy of using acoustic measurements to detect trailing edge cracks on the blades of a full-scale operational turbine in the field.

REFERENCES

[1] Y. Zhang, F. Avallone, and S. Watson. Wind turbine blade trailing edge crack detection based on airfoil aerodynamic noise: An experimental study. *Applied Acoustics* **191** (2022), 108668.

[2] P. Enevoldsen and M. Z. Jacobson. Data investigation of installed and output power densities of onshore and offshore wind turbines worldwide. *Energy for Sustainable Development* **60** (2021), 40–51.

[3] M. deCastro, S. Salvador, M. Gómez-Gesteira, et al. Europe, China and the United States: Three different approaches to the development of offshore wind energy. *Renewable and Sustainable Energy Reviews* **109** (2019), 55–70.

[4] R. Lacal-Arántegui. Globalization in the wind energy industry: contribution and economic impact of European companies. *Renewable Energy* **134** (2019), 612–628.

[5] S. Watson, A. Moro, V. Reis, et al. Future emerging technologies in the wind power sector: A European perspective. *Renewable and Sustainable Energy Reviews* **113** (2019), 109270.

[6] Wind Europe. *Wind energy in Europe - 2020 Statistics and the outlook for 2021-2025*. 2021.

[7] J. Lee and F. Zhao. Global Wind Report | GWEC. *Global Wind Energy Council* (2021), 75.

[8] C. C. Ciang, J. R. Lee, and H. J. Bang. Structural health monitoring for a wind turbine system: A review of damage detection methods. *Measurement Science and Technology* **19** (2008).

[9] C. Q. Gómez Muñoz, F. P. García Marquez, B. Hernandez Crespo, and K. Makaya. Structural health monitoring for delamination detection and location in wind turbine blades employing guided waves. *Wind Energy* **22** (2019), 698–711.

[10] S. Shanbr, F. Elasha, M. Elforjani, and J. Teixeira. Detection of natural crack in wind turbine gearbox. *Renewable Energy* **118** (2018), 172–179.

[11] H. Singh, R. V. Pulikollu, W. Hawkins, and G. Smith. Investigation of Microstructural Alterations in Low- and High-Speed Intermediate-Stage Wind Turbine Gearbox Bearings. *Tribology Letters* **65** (2017), 1–13.

[12] U. Bhardwaj, A. P. Teixeira, and C. G. Soares. Reliability prediction of an offshore wind turbine gearbox. *Renewable Energy* **141** (2019), 693–706.

[13] K. Alewine and W. Chen. A review of electrical winding failures in wind turbine generators. *IEEE Electrical Insulation Magazine* **28** (2012), 8–13.

[14] R. K. Ibrahim, S. J. Watson, S. Djurović, and C. J. Crabtree. An effective approach for rotor electrical asymmetry detection in wind turbine DFIGs. *IEEE Transactions on Industrial Electronics* **65** (2018), 8872–8881.

[15] M. A. S. Shohag, E. C. Hammel, D. O. Olawale, and O. I. Okoli. Damage mitigation techniques in wind turbine blades: A review. *Wind Engineering* **41** (2017), 185–210.

[16] J. Ribrant and L. Bertling. Survey of failures in wind power systems with focus on Swedish wind power plants during 1997-2005. *2007 IEEE Power Engineering Society General Meeting, PES* (2007), 1–8.

[17] C. Dao, B. Kazemtabrizi, and C. Crabtree. Wind turbine reliability data review and impacts on levelised cost of energy. *Wind Energy* **22** (2019), 1848–1871.

[18] W. Yang, Z. Peng, K. Wei, and W. Tian. Structural health monitoring of composite wind turbine blades: Challenges, issues and potential solutions. *IET Renewable Power Generation* **11** (2017), 411–416.

[19] A. Joshuva and V. Sugumaran. A study of various blade fault conditions on a wind turbine using vibration signals through histogram features. *Journal of Engineering Science and Technology* **13** (2018), 102–121.

[20] K. F. Abdulraheem and G. Al-Kindi. A Simplified wind turbine blade crack identification using Experimental Modal Analysis (EMA). *International Journal of Renewable Energy Research* **7** (2017), 715–722.

[21] A. Sarrafi, Z. Mao, C. Niezrecki, and P. Poozesh. Vibration-based damage detection in wind turbine blades using Phase-based Motion Estimation and motion magnification. *Journal of Sound and Vibration* **421** (2018), 300–318.

[22] G. Oliveira, F. Magalhães, Á. Cunha, and E. Caetano. Vibration-based damage detection in a wind turbine using 1 year of data. *Structural Control and Health Monitoring* **25** (2018), 1–22.

[23] K. Schroeder, W. Ecke, J. Apitz, E. Lembke, and G. Lenschow. A fibre Bragg grating sensor system monitors operational load in a wind turbine rotor blade. *Measurement Science and Technology* **17** (2006), 1167–1172.

[24] T. Verbruggen. Load monitoring for wind turbines. Fibre optic sensing and data processing. *Wind Energy* (2013).

[25] J. Sierra-Pérez, M. A. Torres-Arredondo, and A. Güemes. Damage and nonlinearities detection in wind turbine blades based on strain field pattern recognition. FBGs, OBR and strain gauges comparison. *Composite Structures* **135** (2016), 156–166.

[26] R. Yang, Y. He, A. Mandelis, et al. Induction infrared thermography and thermal-wave-radar analysis for imaging inspection and diagnosis of blade composites. *IEEE Transactions on Industrial Informatics* **14** (2018), 5637–5647.

[27] A. Manohar, J. Tippmann, and F. Lanza di Scalea. Localization of defects in wind turbine blades and defect depth estimation using infrared thermography. *Sensors and Smart Structures Technologies for Civil, Mechanical, and Aerospace Systems 2012* **8345** (2012), 83451O.

[28] J. Talbot, Q. Wang, N. Brady, and R. Holden. Offshore wind turbine blades measurement using Coherent Laser Radar. *Measurement: Journal of the International Measurement Confederation* **79** (2016), 53–65.

[29] S. Hwang, Y. K. An, and H. Sohn. Continuous-wave line laser thermography for monitoring of rotating wind turbine blades. *Structural Health Monitoring* **18** (2019), 1010–1021.

[30] B. Park, H. Sohn, P. Malinowski, and W. Ostachowicz. Delamination localization in wind turbine blades based on adaptive time-of-flight analysis of noncontact laser ultrasonic signals. *Nondestructive Testing and Evaluation* **32** (2017), 1–20.

[31] P. A. Joosse, M. J. Blanch, A. G. Dutton, et al. Acoustic emission monitoring of small wind turbine blades. *Journal of Solar Energy Engineering, Transactions of the ASME* **124** (2002), 446–454.

[32] J. Tang, S. Soua, C. Mares, and T. H. Gan. An experimental study of acoustic emission methodology for in service condition monitoring of wind turbine blades. *Renewable Energy* **99** (2016), 170–179.

[33] B. H. Han, D. J. Yoon, Y. H. Huh, and Y. S. Lee. Damage assessment of wind turbine blade under static loading test using acoustic emission. *Journal of Intelligent Material Systems and Structures* **25** (2014), 621–630.

[34] S. Shahidan, R. Pulin, N. Muhamad Bunnori, and K. M. Holford. Damage classification in reinforced concrete beam by acoustic emission signal analysis. *Construction and Building Materials* **45** (2013), 78–86.

[35] K. Aizawa, P. Poozesh, C. Niezrecki, et al. An acoustic-array based structural health monitoring technique for wind turbine blades. *Structural Health Monitoring and Inspection of Advanced Materials, Aerospace, and Civil Infrastructure 2015* **9437** (2015), 94371P.

[36] P. Poozesh, K. Aizawa, C. Niezrecki, et al. Structural health monitoring of wind turbine blades using acoustic microphone array. *Structural Health Monitoring* **16** (2017), 471–485.

[37] C. Traylor, M. DiPaola, D. J. Willis, and M. Inalpolat. A computational investigation of airfoil aeroacoustics for structural health monitoring of wind turbine blades. *Wind Energy* **23** (2020), 795–809.

[38] J. Solimine, C. Niezrecki, and M. Inalpolat. An experimental investigation into passive acoustic damage detection for structural health monitoring of wind turbine blades. *Structural Health Monitoring* **19** (2020), 1711–1725.

[39] C. Beale, C. Niezrecki, and M. Inalpolat. An adaptive wavelet packet denoising algorithm for enhanced active acoustic damage detection from wind turbine blades. *Mechanical Systems and Signal Processing* **142** (2020), 106754.

[40] C. Beale, D. J. Willis, C. Niezrecki, and M. Inalpolat. Passive acoustic damage detection of structural cavities using flow-induced acoustic excitations. *Structural Health Monitoring* **19** (2020), 751–764.

[41] T. F. Brooks, D. S. Pope, and M. A. Marcolini. *Airfoil self-noise and prediction.* Vol. 1218. National Aeronautics and Space Administration, 1989.

[42] B. M. Fazenda and D. Comboni. Acoustic condition monitoring of wind turbines: Tip faults. *9th International Conference on Condition Monitoring and Machinery Failure Prevention Technologies 2012, CM 2012 and MFPT 2012* **1** (2012), 109–123.

[43] B. Chen, S. Yu, Y. Yu, and Y. Zhou. Acoustical damage detection of wind turbine blade using the improved incremental support vector data description. *Renewable Energy* **156** (2020), 548–557.

[44] C. Q. Zhang, Z. Y. Gao, Y. Y. Chen, et al. Locating and tracking sound sources on a horizontal axis wind turbine using a compact microphone array based on beamforming. *Applied Acoustics* **146** (2019), 295–309.

[45] T. H. Tu, F. C. Lo, C. C. Liao, C. F. Chung, and R. C. Chen. Using wind turbine noise to inspect blade damage through portable device. *INTER-NOISE 2019 MADRID - 48th International Congress and Exhibition on Noise Control Engineering* (2019), 1–5.

[46] M. Pawlaczyk-ŁUszczyńska, A. Dudarewicz, K. Zaborowski, M. Zamojska-Daniszewska, and M. Waszkowska. Evaluation of annoyance from the wind turbine noise: A pilot study. *International Journal of Occupational Medicine and Environmental Health* **27** (2014), 364–388.

[47] D. S. Michaud, K. Feder, S. E. Keith, et al. Exposure to wind turbine noise: Perceptual responses and reported health effects. *The Journal of the Acoustical Society of America* **139** (2016), 1443–1454.

[48] S. Luesutthiviboon, D. Ragni, F. Avallone, and M. Snellen. An alternative permeable topology design space for trailing-edge noise attenuation. *International Journal of Aeroacoustics* (2021).

[49] C. Teruna, F. Avallone, D. Casalino, and D. Ragni. Numerical investigation of leading edge noise reduction on a rod-airfoil configuration using porous materials and serrations. *Journal of Sound and Vibration* **494** (2021), 1–25.

[50] Q. Ye, F. Avallone, D. Ragni, M. Choudhari, and D. Casalino. Effect of Surface Roughness Geometry on Boundary-Layer Transition and Far-Field Noise. *AIAA Journal* (2021), 1–13.

[51] S. M. Hasheminejad, T. P. Chong, G. Lacagnina, et al. On the manipulation of flow and acoustic fields of a blunt trailing edge aerofoil by serrated leading edges. *The Journal of the Acoustical Society of America* **147** (2020), 3932–3947.

[52] W. K. Blake. *Mechanics of flow-induced sound and vibration, Volume 2: Complex flow-structure interactions*. Academic press, 2017.

[53] S. Oerlemans. Wind turbine noise : primary noise sources (2011), 1–57.

[54] G. Bampanis, M. Roger, D. Ragni, F. Avallone, and C. Teruna. Airfoil-turbulence interaction noise source identification and reduction by leading-edge serrations. *25th AIAA/CEAS Aeroacoustics Conference, 2019* (2019), 1–18.

[55] R. Merino-Martínez, A. Rubio Carpio, L. T. Lima Pereira, et al. Aeroacoustic design and characterization of the 3D-printed, open-jet, anechoic wind tunnel of Delft University of Technology. *Applied Acoustics* **170** (2020).

[56] M. Drela. "XFOIL: An analysis and design system for low Reynolds number airfoils". In: *Low Reynolds number aerodynamics*. Springer, 1989, pp. 1–12.

[57] S. Oerlemans. Detection of aeroacoustic sound sources on aircraft and wind turbines (2009), 1–173.

[58] P. Sijtsma. Phased Array Beamforming Applied to Wind Tunnel and Fly-Over Tests. *SAE Technical Papers* **2010-Octob** (2010), 17–19.

[59] R. Merino-Martínez, P. Sijtsma, A. R. Carpio, et al. Integration methods for distributed sound sources. *International Journal of Aeroacoustics* **18** (2019), 444–469.

[60] P. Sijtsma and M. Snellen. Inverse integration method for distributed sound sources. *BeBeC* (2018), 9–17.

[61] G. Comte-Bellot and S. Corrsin. The use of a contraction to improve the isotropy of grid-generated turbulence. *Journal of Fluid Mechanics* **25** (1966), 657–682.

[62] J. Groth and A. V. Johansson. Turbulence reduction by screens. *Journal of Fluid Mechanics* **197** (1988), 139–155.

[63] T. Kurian and J. H. Fransson. Grid-generated turbulence revisited. *Fluid Dynamics Research* **41** (2009).

[64] J. C. Isaza, R. Salazar, and Z. Warhaft. On grid-generated turbulence in the near- and far field regions. *Journal of Fluid Mechanics* **753** (2014), 402–426.

[65] N. Thomareisa and G. Papadakis. Effect of trailing edge shape on the separated flow characteristics around an airfoil at low reynolds number: A numerical study. *Physics of Fluids* **29** (2017).

[66] C. N. Metzinger, R. Chow, J. P. Baker, A. M. Cooperman, and C. P. Van Dam. Experimental and computational investigation of blunt trailing-edge airfoils with splitter plates. *AIAA Journal* **56** (2018), 3229–3239.

[67] S. Oerlemans, P. Sijtsma, and B. Méndez López. Location and quantification of noise sources on a wind turbine. *Journal of Sound and Vibration* **299** (2007), 869–883.

[68] B. Cheng, Y. Han, K. S. Brentner, et al. Surface roughness effect on rotor broadband noise. *International Journal of Aeroacoustics* **17** (2018), 438–466.

[69] W. R. Wolf, J. L. Azevedo, and S. K. Lele. Effects of mean flow convection, quadrupole sources and vortex shedding on airfoil overall sound pressure level. *Journal of Sound and Vibration* **332** (2013), 6905–6912.

[70] W. J. Zhu, W. Z. Shen, J. N. Sørensen, and G. Leloudas. Improvement of airfoil trailing edge bluntness noise model. *Advances in Mechanical Engineering* **8** (2016), 1–12.

[71] F. Hutcheson and T. Brooks. Noise radiation from single and multiple rod configurations. *International Journal of Aeroacoustics* **11** (2012), 291–334.

4

PHYSICS OF NOISE CHANGES FOR TRAILING EDGE CRACK DETECTION

In the last chapter, the trailing edge noise spectra for the airfoil with cracks were investigated. However, the physics of how the crack and turbulent inflow affect the noise emission is still not clear. In this chapter, to further fill in this research gap and eventually link the crack-induced tones to the crack size for both clean and turbulent inflow conditions, the velocity fields near the trailing edge and in the near wake are measured using the Particle Image Velocimetry (PIV) technique. The experimental results indicate that the velocity gradient near the wall region at the trailing edge location increases as the size of the crack increases, for both clean and turbulent inflows. This creates stronger coherent vortex shedding with respect to the baseline configuration with consequent louder tonal noise at higher frequencies. It is confirmed that the normalized frequencies of the tones induced by the crack agree with the tonal prediction model proposed by Brooks, Pope and Marcolini. For a turbulent condition, the length scale of the coherent vortex structures slightly decreases with respect to the clean inflow one, with a consistent increase in the frequency of the tonal component. This suggests that when using this prediction model to estimate the crack size or trailing edge thickness, the impact of the turbulent inflow cannot be neglected.

Parts of this chapter have been submitted to *Journal of Sound and Vibration* (2023).

4.1. INTRODUCTION

In recent years, wind energy has become one of the most promising renewable energy sources, thus attracting increasing interest in both industry and academia [1, 2]. However, wind turbine blades are often subjected to several types of damage, such as erosion of the leading edge caused by sand particles, raindrops, or other airborne objects [3–5]; trailing-edge cracks due to fatigue failures of the adhesive joints [6, 7]; and blade coating delamination or shedding due to ageing and weathering [8]. The direct consequence of these types of damage is that the aerodynamic performance of the blades is reduced [9] with the consequent chance of full system failure [10].

Therefore, blade health condition monitoring and damage detection have become increasingly important to maintain stable power output and safe operation of the wind turbine. Continuous monitoring can be helpful in assessing the severity of damage and predicting its development. Established techniques for blade damage detection generally rely on measurements of vibration [11, 12], strain [13] or acoustic emission (AE) [14]. These techniques adopt mounting one or multiple sensors mounted on or in the blade requiring cumbersome retrofitting for wind turbines that are already operational. For this reason, non-contact approaches are being developed such as infrared thermography [15] and laser scanning techniques [16]. These techniques provide a clear visualization of the damage, but at the cost of complicated post-processing.

In recent years, wind turbine noise has been a crucial issue to be mitigated to meet the installation regulations and social acceptance [17], in particular for onshore wind farms. Since aerodynamic noise from a wind turbine is one of the most important noise sources, many studies have been conducted to reduce it by adjusting the geometry of the airfoils [18–20], adding serrations [21, 22] or adopting porous materials [23–26]. These techniques are standard approaches for noise reduction, on which some benchmark studies have focused [27, 28]. These studies have inspired a new application of aeroacoustics for wind turbine blade damage detection. The working principle is based upon the modifications to the flow field that surface damage can cause, which in turn affects aerodynamically generated noise.

Acoustic measurements might complement other damage detection techniques such as those mentioned above with the final aim to better quantify damage. A recent promising non-contact detection approach is based on remote acoustic measurements using microphones in the far-field [29–32]. The studies presented in Chapters 3 and 5 proved that, under some circumstances, measurements of aerodynamic noise can provide useful information for blade damage detection. For example, in the presence of leading-edge erosion, it has been found that the leading-edge impingement noise has lower high-frequency spectral content with respect to a baseline reference airfoil. This was attributed to a larger stagnation region [20, 33] formed in front of the eroded leading edge and to a consequent reduction in the magnitude of the surface pressure fluctuations at the leading edge [34]. It was further observed that the difference in the spectral peak sound pressure level between the baseline airfoil and one with an eroded leading edge, $\Delta L_p = L_{p,\text{Baseline}} - L_{p,\text{Erosion}}$, occurs at chord-length-based Strouhal number $St_C \sim 10$. Moreover, the amplitude of ΔL_p increases as the size of the damage increases.

By contrast, when a crack appears at the trailing edge, this results in an effective thicker trailing edge that can cause blunt trailing edge noise. It is known from the lit-

erature that, when the trailing edge thickness, h, is approximately larger than 0.3 times the boundary layer displacement thickness, δ^*, periodic vortex shedding appears causing tonal noise [35–37]. The frequency and amplitude of the tonal peaks depend on the ratio of trailing edge thickness to boundary layer thickness, h/δ^*, and it usually appears at trailing-edge-thickness-based Strouhal number $St_h \sim 0.1$ [38]. In the previous work in Chapter 3, it was investigated how the trailing edge crack and the operational conditions affect the trailing edge noise spectra, in particular the crack-induced tones. However, it is not clear yet how the change of thickness due to the damage at the trailing edge and the inflow conditions affect locally the velocity gradient (this may potentially affect the coherent vortex shedding [39, 40]), the development of the turbulent boundary layer and consequently the associated tones. Such knowledge is essential to confirm if semi-empirical models used to predict blunt trailing edge noise [38] can still be adopted in the presence of trailing-edge damage, and if the prediction is robust under both uniform and turbulent inflow conditions. A fact that has inspired this investigation is that when inflow turbulence is introduced, it has been found that the crack-induced tone shifts to a slightly higher value of the trailing-edge-thickness-based Strouhal number [31], but how the turbulent inflow affects the integral boundary layer parameters at the trailing edge is still not known and is rarely reported in the literature. The present study in this chapter explains how the trailing edge crack modifies the boundary layer velocity gradients and the coherent vortex structures in the near wake for both clean and turbulent inflow conditions, and links them to the acoustic measurements. This will provide prior knowledge for a more accurate estimation of crack size using the current semi-empirical models [38].

To this end, the present study combines measurements of aerodynamic far-field noise and velocity fields near the trailing edge region and in the near wake of a NACA 0018 airfoil with different crack sizes for clean and turbulent inflow conditions. The aerodynamic noise is measured using a phased microphone array coupled with a beamforming technique [37, 41]. The velocity fields are measured using Particle Image Velocimetry (PIV) [42, 43]. To further analyze the vortex shedding from the trailing edge, Proper Orthogonal Decomposition (POD) is applied to the velocity fields [42, 43].

The rest of this chapter is organized as follows: Section 4.2 presents the experimental setup and the methodologies used both for the acoustic and aerodynamic measurements. In Section 4.3, the experimental results and the relationship between the acoustic and aerodynamic data are reported and the interpretation of the change of the crack-induced tone is also discussed. Section 4.4 summarizes the findings of this study and provides recommendations for the next steps.

4.2. EXPERIMENTAL SETUP AND METHODOLOGY

4.2.1. FACILITIES AND TEST MODELS

The experiments were carried out in the anechoic vertical open-jet wind tunnel (A-tunnel) of Delft University of Technology [44]. The turbulence intensity of the inflow is below 0.1% of the free-stream velocity. Absorbent foam wedges, with a height of 0.49 m, are placed on the walls of the test room; the acoustic cutoff frequency is 173.5 Hz; the A-weighted overall background noise levels vary from 35 dBA to 64 dBA as the free stream

velocity increases from 10 m/s to 40 m/s. Additional details on the wind tunnel characteristics can be found in Reference [44]. To mimic the turbulent inflow conditions, a grid was designed and mounted on the nozzle of the wind tunnel providing a turbulent inflow with a turbulence intensity level of $I = 4.0\%$ and an integral length scale of $\Lambda_f = 7.9$ mm. A detailed characterization of the inflow turbulence can be found in Chapter 2.

A NACA 0018 airfoil with a chord length of $C = 200$ mm and a span of $L = 400$ mm was tested. The trailing edge of the airfoil is changeable which allows the testing of different trailing edge configurations with different crack sizes. Each crack was designed as a rectangular gap with a given width, W, and depth, $D = 1.5W$. The dimensions of the trailing edge cracks investigated are reported in Table 4.1. Consequently, the thickness of the trailing edge, h, is equal to $h_{\text{Baseline}} + W$ (where h_{Baseline} is the trailing edge thickness of the baseline). Figure 4.1 shows the baseline airfoil and an example of the trailing edge with a crack width of 0.2 mm. Due to the nature of the open test section of the wind tunnel, the effective angle of attack, α^*, is lower than the geometrical one, α, more specifically $\alpha^*/\alpha = 0.48$ [31].

Table 4.1: The dimensions of the cracked trailing edges.

Trailing edge No.	0	1	2	3	4
W (mm)	0	0.20	0.50	1.00	2.00
h (mm)	0.76	0.96	1.26	1.76	2.76
W/C(%)	0	0.10	0.25	0.50	1.00
h/C(%)	0.38	0.48	0.63	0.88	1.38

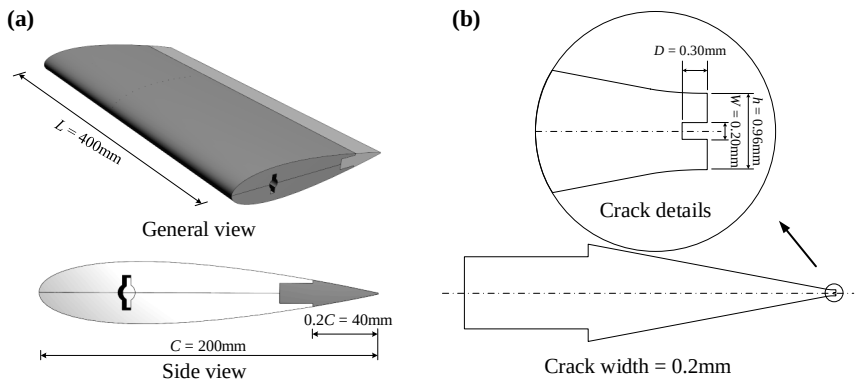

Figure 4.1: The test airfoil: (a) baseline (a trailing edge insert without a crack is shown as darker gray in the side view) and (b) an example of a trailing edge insert with a 0.2 mm crack.

The tests were carried out at mean inflow velocities equal to $U_\infty = 15$ m/s, 20 m/s, 25 m/s, 30 m/s and 35 m/s, which correspond to the chord-length-based Reynolds numbers of $Re_C = 2.0\times10^5$, 2.7×10^5, 3.4×10^5, 4.1×10^5 and 4.7×10^5, respectively. Due to the

low-Reynolds number conditions, the flow was forced to transition using carborundum tape at 20 % of the chord location on both the suction and pressure sides. The average carborundum roughness element size was 0.84 mm.

4.2.2. ACOUSTIC MEASUREMENTS

Noise measurements were conducted using a 2-D planar microphone array with 64 *G.R.A.S. 40PH* free-field microphones. The sampling frequency of each microphone is 51.2 kHz and the signal was recorded for 20 s for each case. The signal was separated into chunks with 5120 samples (Δt = 0.1 s) for each Fourier transform (with a Hanning weighting function and 50% data overlap) and the spectrum was averaged over all chunks. The final spectral resolution is equal to 10 Hz. Conventional frequency domain beamforming [41, 45] was then carried out on the plane where the trailing edge is located. In this study, the trailing edge noise is of interest, therefore, the source power integration [46] was performed on a 0.2m × 0.2m square area centered at the mid-span of the trailing edge. The detailed setup for the acoustic measurements was reported in Chapter 2.

The sound pressure level (SPL, $L_p = 10\log\left(\frac{p'^2}{p_0^2}\right)$, where p' and p_0 are the root-mean-square of sound pressure fluctuations and reference pressure of 20 μPa for air, respectively) is used as the metric for the far-field noise spectra. In this study, the measured L_p of trailing edge noise was obtained from the beamforming and the source power integration. The measured sound pressure levels of the airfoil trailing edge noise are more than 10 dB above the background noise within the frequency bands 500 – 2000 Hz and 500 – 1500 Hz for the clean and turbulent inflow conditions, respectively (reported in Chapter 2).

The relative sound pressure level, ΔL_p, is used to compare the sound pressure level resulting from the cracked cases with that from the baseline, and is defined as:

$$\Delta L_p = L_p - L_{p,\text{Baseline}} \tag{4.1}$$

The frequency, f, is nondimensionalized by trailing-edge-thickness-based Strouhal number, i.e. $St_h = fh/U_\infty$, where U_∞ is the inflow mean velocity. In order to estimate the frequency of the tonal peak of ΔL_p and reduce the uncertainly of the estimate, the curve of ΔL_p was fitted as

$$\Delta L'_p = Ae^{\left(St_h + St'_{h,\text{peak}}\right)} + B_{\text{offset}} \tag{4.2}$$

where $\Delta L'_p$ denotes the estimation of ΔL_p; $St'_{h,\text{peak}}$ the estimated location of the tonal peak; A and B_{offset} are the fitting coefficients determining the shape and offset of the curve. Figure 4.2 shows examples of the fit for the W = 2.0 mm case with both clean and turbulent (I = 4.0%) inflow conditions.

4.2.3. VELOCITY FIELD MEASUREMENTS

Velocity fields near the trailing edge and in the near wake were measured using a PIV technique. The setup for PIV measurement is shown in Figure 4.3(a). The seeding particles were generated by the SAFEX Twin-Fog Double Power fog generator with an aver-

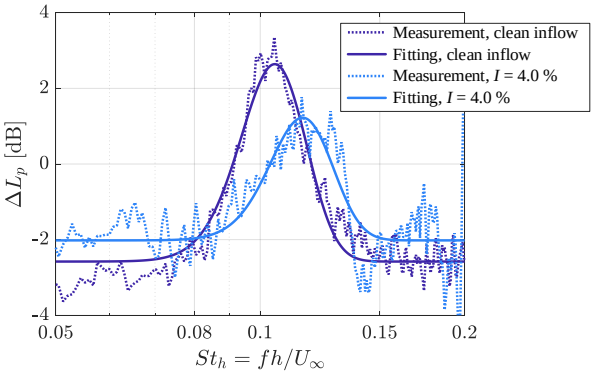

Figure 4.2: The measured spectra and the fitted curves of ΔL_p for W = 2.0 mm case at zero angle of attack and 35 m/s inflow velocity for clean and turbulent inflow conditions.

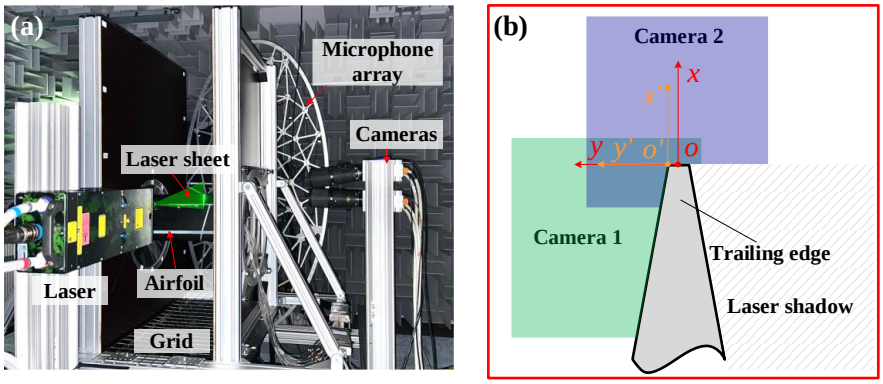

Figure 4.3: Setup for PIV measurements: (a) a picture of the experimental setup and (b) fields of view for the two cameras

age droplet diameter of 1 μm. The laser sheet illuminates the trailing edge surface and near wake with a pulse frequency of 10 Hz. Two LaVision sCMOS cameras were used to record the particle images. One was used to measure the velocity field and the boundary layer near the trailing edge while the other one for the near-wake velocity field. Each camera provided a field of view approximately 32mm × 27mm. The two fields of view are shown in Figure 4.3(b) and a right-hand *xoy* coordinate system was established at the middle span of the trailing edge. Since the trailing edge surface location varies for different crack sizes, an offset coordinate system $x'o'y'$ was adopted to plot the boundary layer profiles, i.e., $y' = y - h/2$, as shown in Figure 4.3(b). For each case, statistics were computed by recording 300 pairs of images. The velocity field calculation was then carried out using the software LaVision DaVis 10.2 with a standard multi-pass 2D cross-correlation algorithm, providing the velocity field with a spatial resolution of 0.3 mm and a vector spacing of 0.075 mm. The measurement uncertainty of the mean velocity and root mean square velocity are 1.15% and 0.82%, respectively. The setup has been described in Chapter 2 in detail.

4.3. RESULTS AND DISCUSSION

4.3.1. VELOCITY FIELD NEAR THE TRAILING EDGE

Figure 4.4 shows the mean flow velocity field near the trailing edge for the different damage cases for both clean and turbulent ($I = 4.0\%$) inflow conditions and the airfoil set at zero angle of attack. For the clean inflow condition (top row in Figure 4.4), the contour lines of the velocity magnitude, U, normalized by the freestream velocity, U_∞, show that near the trailing edge, when increasing the size of the damage, the boundary layer is affected because of a different pressure gradient imposed by the variation in the geometry. For example, the space between the trailing edge surface and the $0.4U_\infty$ contour line decreases as the damage size increases, which indicates that the velocity gradient near the surface is larger when the damage is larger. A similar trend of the velocity gradient can be observed near the airfoil surface when the inflow is turbulent, as shown in the bottom row in Figure 4.4.

BOUNDARY LAYER PROFILE OF THE MEAN VELOCITY

The vortex shedding from a bluff body is potentially affected by the wall-normal boundary layer properties [39, 40]. Since data are shown very close to the trailing edge, the boundary layer profiles of velocity magnitude, U, are shown in the $x'o'y'$ reference system. Figure 4.5 shows the mean velocity profiles at the trailing edge for all the cases investigated, where the velocity is normalized by the boundary layer edge velocity, U_e. The airfoil is tripped so the boundary layer is turbulent for all the cases. The figure confirms the qualitative observations reported previously: the velocity gradient within the inner region in the y'-axis direction increases with the increasing size of the damage. This is found for both inflow conditions. However, for the turbulent inflow cases, the velocity profile slopes ($\mathrm{d}y'/\mathrm{d}U$) at the boundary layer edge region for the baseline and $W = 2.0$ mm cases are smaller than the $W = 0.2$, 0.5, and 1.0 mm ones, which indicates a greater velocity gradient.

Since the boundary layer data at the very near-wall region are not available, to quantify the boundary layer properties, the Clauser plot method [47–49] is employed. The

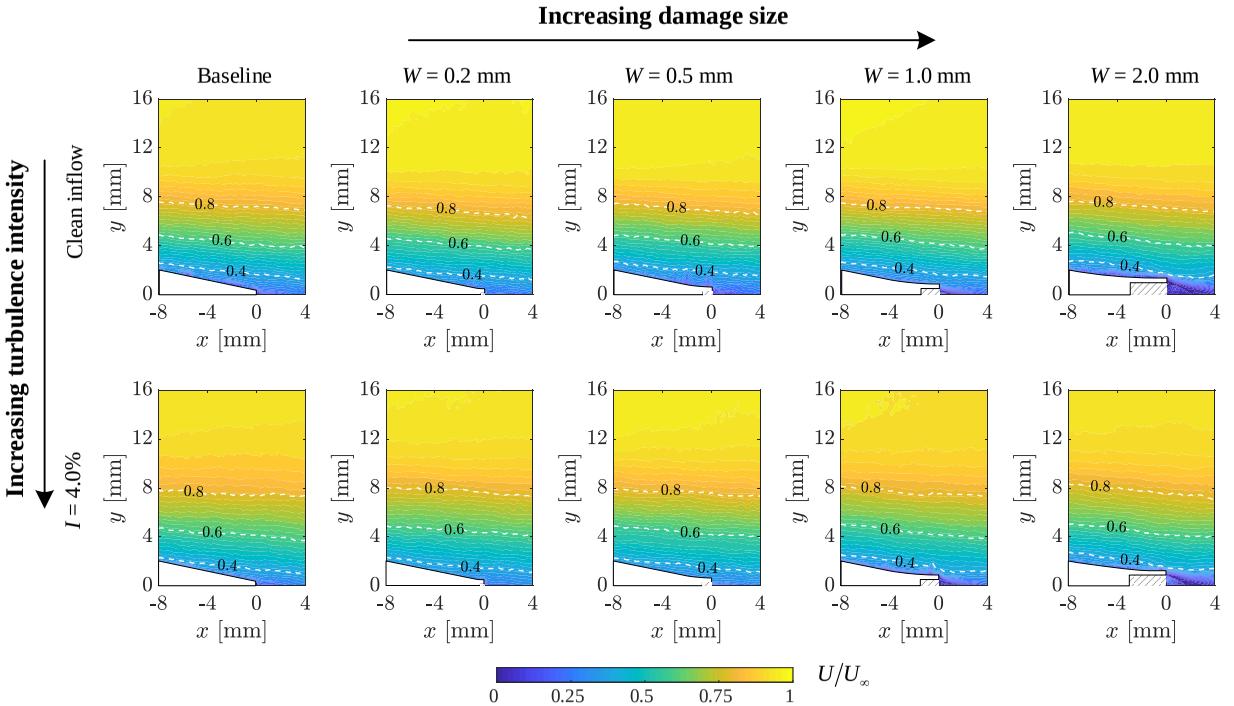

Figure 4.4: Mean velocity field near the trailing edge surface for different crack sizes with clean and turbulent inflows. The white blocks are half sections of the trailing edge and the shaded regions are the shadow areas of the laser.

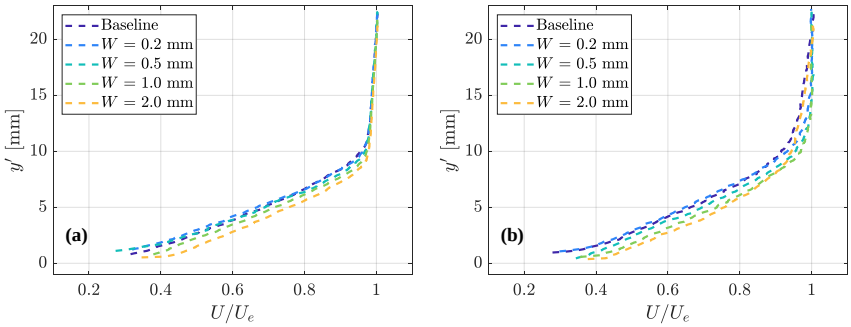

Figure 4.5: Velocity profiles at the trailing edge for different crack sizes for (a) clean inflow and (b) turbulent inflow ($I = 4\%$) conditions.

turbulent boundary layer within the logarithmic region can be fitted as:

$$U^+ = \frac{1}{\kappa} \ln y^+ + B \tag{4.3}$$

where $\kappa = 0.41$ is the von Kármán constant and $B = 5$ as suggested in References [47, 50, 51]. $U^+ = U/U_\tau$ and $y^+ = y'U_\tau/\nu$ are the nondimensional velocity and distance in the y'-axis direction relative to the wall, respectively, where U_τ is the friction velocity and ν is the kinematic viscosity. By introducing the skin friction coefficient, C_f, where

$$\frac{U_\tau}{U_e} = \sqrt{\frac{1}{2C_f}} \tag{4.4}$$

and substituting it into Equation 4.3, there is only one unknown variable C_f that can be determined by fitting the log-law using boundary layer data within the logarithmic region (in this study data are selected within the range $30 < y' < 100$), as shown in Figure 4.6 for both the clean and turbulent inflow cases. Retrieving U_τ, the boundary layer profile at the near-wall region (viscous sublayer) reads as

$$U^+ = y^+ \tag{4.5}$$

The friction coefficients, C_f, and friction velocities, U_τ, for the above cases investigated are presented in Table 4.2. The obtained C_f and U_τ of the baseline case agree with the ones in previous studies [22, 49]. For the clean inflows, as the crack size increases, the friction coefficient, C_f, and friction velocity, U_τ, increase as well. This indicates that in the near wall region, a greater trailing edge crack size also leads to a larger velocity gradient. Similarly to the clean inflow cases, when the turbulent inflow is investigated, both the friction coefficient, C_f, and friction velocity, U_τ, tend to be greater but the differences between the smaller crack cases are not significant.

Figure 4.7 shows the mean velocity profiles for the baseline airfoil and the ones with a crack of $W = 2.0$ mm for clean inflow conditions at different free-stream velocities. With the increase in inflow velocity, for both baseline and cracked cases, the differences

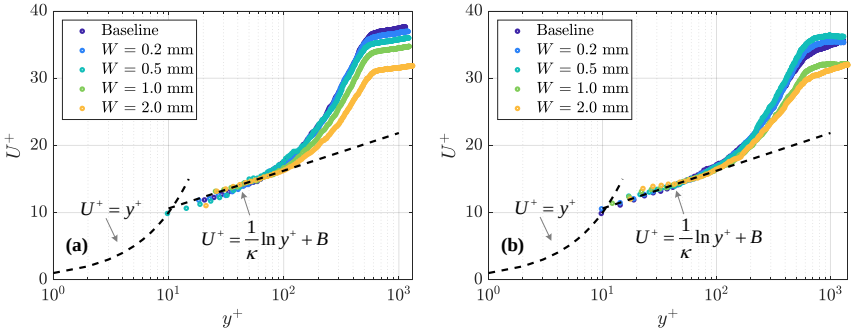

Figure 4.6: The nondimensional velocity profiles at the trailing edge for different damage cases for (a) clean inflow and (b) turbulent inflow ($I = 4\%$) conditions.

Table 4.2: Skin friction coefficient, C_f, and the friction velocity, U_τ, obtained by applying the Clauser's method.

Crack size, W (mm)	Clean inflow		$I = 4.0\%$	
	$C_f (\times 10^{-3})$	U_τ (m/s)	$C_f (\times 10^{-3})$	U_τ (m/s)
0 (Baseline)	1.4	0.891	1.6	0.974
0.2	1.5	0.918	1.6	0.940
0.5	1.5	0.944	1.5	0.917
1.0	1.5	0.977	1.9	1.024
2.0	1.7	1.068	2.0	1.058

in velocity profiles are mainly observed in the inner region. The slope of the velocity profile curve (dy'/dU) in this region is slightly smaller as the inflow velocity increases. This agrees with the trend of boundary development on the flat plate or in a pipe by increasing the Reynolds number [52]. Similarly, by comparing the cracked cases to the baseline one for all the tested velocities, it is found that the cracks lead to a greater velocity gradient within the inner region of the boundary layer, which agrees with the results discussed earlier in this Chapter. Figure 4.8 shows the same cases for the turbulent inflow condition demonstrating that the crack leads to similar changes in the boundary layer velocity gradient. However, by changing the inflow conditions, as shown in Figure 4.7 and Figure 4.8, the velocity gradient at the boundary layer edge is greater for the turbulent condition, as the slopes of the velocity profiles in the region near the boundary layer edge are smaller than those tested with clean inflow. This suggests that the inflow turbulence strongly affects the boundary layer at the outer region. Similar results were also found in previous works [53–55].

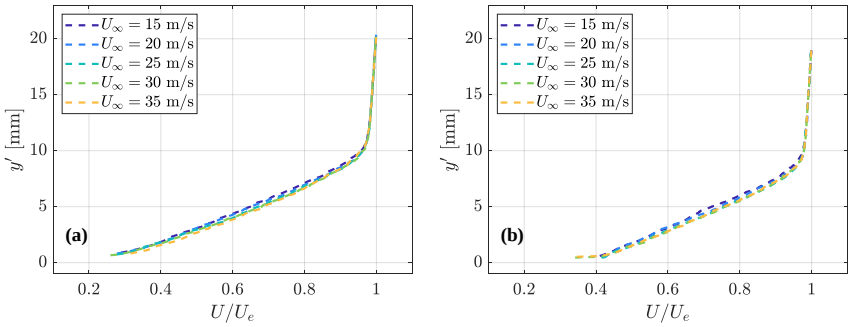

Figure 4.7: Velocity profiles at the trailing edge for clean inflows of different mean velocities: (a) baseline and (b) $W = 2.0$ mm.

Figure 4.9 shows the mean velocity profiles of the baseline and $W = 2.0$ mm cases at angles of attack of 0° and 5° for the clean inflow condition. On the suction side, as the angle of attack increases, the velocity gradient becomes smaller in the inner region of the boundary layer, where the slope of the velocity profile is greater, for both the baseline and damaged cases; this agrees with the results of previous studies in the literature [56]. As the crack is present, for both angles of attack, the velocity gradient on the suction side becomes greater compared with the baseline case. On the pressure side, the increase in the angle of attack leads to a greater velocity gradient near the wall for both the baseline and cracked cases; however, as the angle of attack increases, the differences in the boundary layer between the baseline and the cracked case become less significant. Figure 4.10 shows the same cases for the turbulent inflow condition, where similar results can be observed. The differences happen at the edge of the boundary layer, where for the turbulent inflow cases, the slopes of the boundary layer profiles become smaller indicating greater velocity gradients compared with the same cases for the clean inflow.

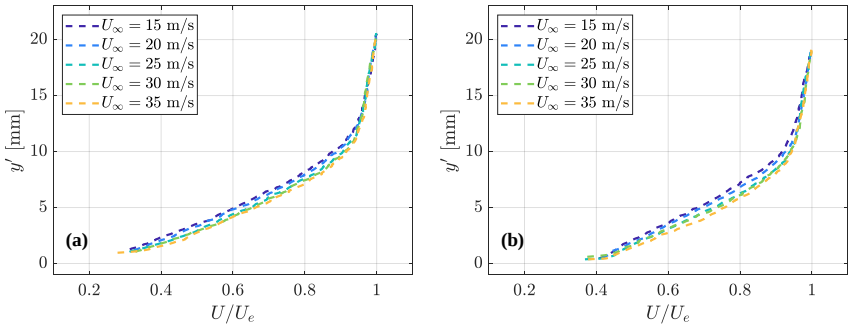

Figure 4.8: Velocity profiles at the trailing edge for turbulent inflows of different mean velocities: (a) baseline and (b) $W = 2.0$ mm.

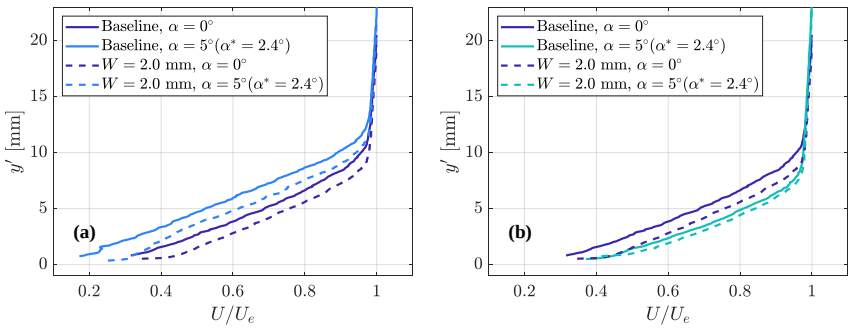

Figure 4.9: Velocity profiles at the trailing edge of the clean inflow condition for different angles of attack: (a) on the suction side and (b) on the pressure side.

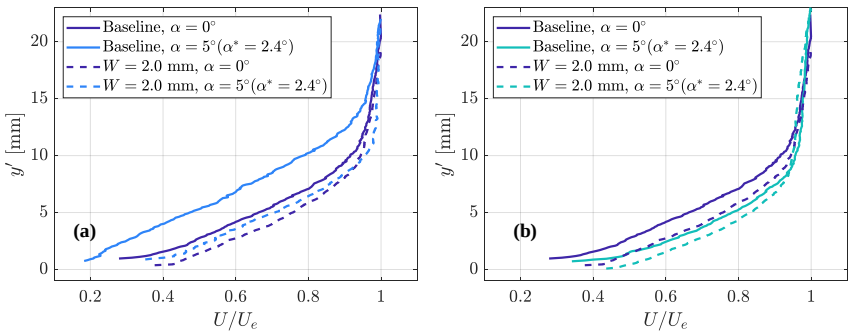

Figure 4.10: Velocity profiles at the trailing edge of the turbulent inflow condition ($I = 4.0\%$) for different angles of attack: (a) on the suction side and (b) on the pressure side.

BOUNDARY LAYER THICKNESS AND DISPLACEMENT THICKNESS

Figure 4.11 shows the boundary layer thickness, δ, and displacement thickness, δ^*, at the trailing edge for the cases with different crack sizes. In the present work, the boundary layer thickness is defined as the point where the velocity within the boundary layer reaches 95% of the boundary layer edge velocity, U_e, i.e. $\delta = \delta_{95}$, and the displacement thickness is defined as $\delta^* = \int_0^{\delta} \left(1 - U\left(y'\right)/U_e\right) \mathrm{d}y'$. When the inflow is clean, both the boundary layer thickness and displacement thickness tend to decrease as the crack size increases. This is because the crack results in an increase in the velocity gradient of the boundary layer at the trailing edge and as the size of the crack increases the velocity gradient becomes greater. When the turbulent inflow is introduced, both the boundary layer thickness and displacement thickness tend to be thicker compared with the ones for the clean inflow condition. For the damaged cases with smaller cracks (W = 0.2, 0.5 and 1.0 mm), a decay trend can be seen both for the boundary layer thickness and displacement thickness. However, for the 2.0 mm crack case, an increasing trend is presented for both boundary layer thickness and displacement thickness. This mainly results from a lower slope of velocity profile for the 2.0 mm crack case near the boundary layer edge where the velocity recovers to the free-stream velocity more slowly compared to the other cracked cases, as shown in Figure 4.5(b).

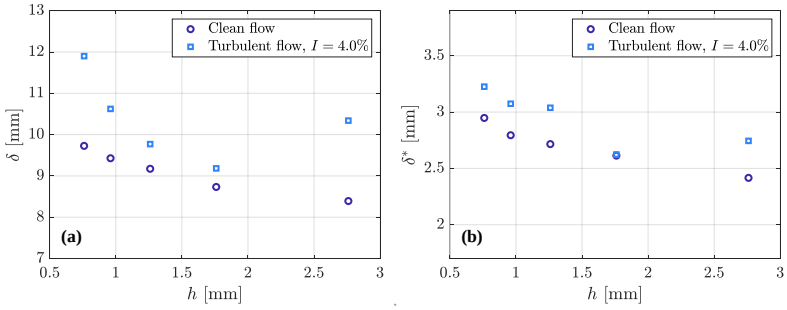

Figure 4.11: Boundary layer thickness and displacement thickness at the trailing edge for different crack sizes for 35 m/s inflow and zero angle of attack condition: (a) boundary layer thickness and (b) displacement thickness.

Varying the inflow velocity, as shown in Figure 4.12 for the crack where W = 2.0 mm, both boundary layer thickness and displacement thickness become thinner as the inflow velocity increases. For the turbulent inflow condition, both the boundary layer and displacement thickness become slightly thicker than the clean inflow ones. This is attributed to greater gradients (with smaller slopes of velocity profiles) near the edge of the boundary layer when the inflow is turbulent, thus making a greater integral area below the velocity profile for the calculation of displacement thickness, as discussed previously when comparing Figure 4.7 and Figure 4.8. For both clean and turbulent inflow conditions, the measured boundary layer thickness or displacement thickness decays with the -1/5th power law of the chord-length-based Reynolds number, which agrees with the trends of turbulent boundary layer thickness or displacement thickness for a

flat plate as the Reynolds number increases [57].

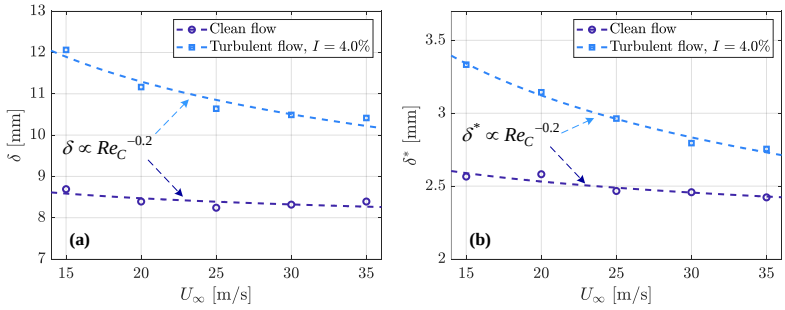

Figure 4.12: Boundary layer thickness and displacement thickness at the trailing edge of $W = 2.0$ mm for different inflow velocities and zero angle of attack conditions: (a) boundary layer thickness and (b) displacement thickness.

4.3.2. VELOCITY FIELD OF THE NEAR WAKE

The crack-induced tonal components in the far-field noise spectra are related to the coherent vortex structures shed from the trailing edge. In order to analyze the vortex shedding, POD is performed in the near wake.

Figure 4.13 shows the energy distribution of POD modes, ϕ_v, for the vertical component of the velocity, v, for the crack sizes equal to 1.0 mm and 2.0 mm with both clean and turbulent inflows. The energy of each i-th POD mode, λ_i, is scaled by the total energy of all modes. For the 1.0 mm and the 2.0 mm cracks and clean inflow conditions, the energy of the first two modes is close and a stair-stepping distribution is observed. This indicates that the first two modes might be associated with strong coherent vortex structures in the near wake [43]. As the damage level increases, the energy of the first two modes increases which suggests that the contribution of coherent vortex structures to the total fluctuations in the near wake is greater [58, 59]. For the 2.0 mm crack and turbulent inflow, the difference in the energy between the first two modes becomes larger compared to the clean inflow case and the stair-stepping distribution is not clear. To verify if the first two modes for this case are associated with the same coherent vortex shedding, an analysis for the spatial distribution of the vortex structures in the first two modes is conducted subsequently, as suggested in the References [58, 60].

Figure 4.14 shows the first two POD modes for the same cases mentioned above. The x-axis and y-axis are scaled with the trailing edge thickness which allows a comparison of the relative size of the vortices. For all the cases, it is observed that there is a difference between the locations of the vortex structure cores in the first mode and second mode, with the latter being located at a distance of approximately 1/4 of the length of the vortex structures downstream [43, 58, 59, 61, 62]. This confirms that the first two modes are linked to the same coherent vortex shedding. Comparing the 1.0 mm crack case with the 2.0 mm crack case for the clean inflow condition, it can be observed that the vortex structures are stronger for the latter case, as expected because of the thicker trailing edge.

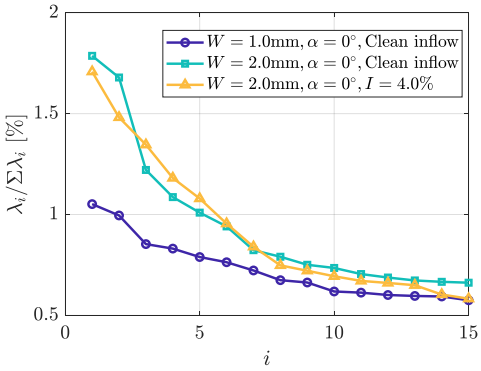

Figure 4.13: The energy distribution of the POD modes for 1.0 mm crack and 2.0 mm crack cases for different inflow conditions.

For the turbulent inflow condition, the shapes of the first two modes look like the ones for the clean inflow condition but the strength of the vortex structures appears to be slightly lower.

Figure 4.15 shows the energy distribution of the POD modes for the 2.0 mm crack case at an angle of attack of $\alpha = 5°$ ($\alpha^* = 2.4°$) and clean inflow condition. In contrast to the case at zero angle of attack, the energy of the first mode is much larger than the second mode and the stair-stepping is not present. The energy of the second and third modes are close, and these two modes seem to be paired, thus hinting at coherent vortex shedding. Figure 4.15(b)-(d) shows the first three POD modes. The second and third modes show similar characteristics to the ones of the first two modes for the zero angle of attack case: the cores of the vortex structures in the second mode shift 1/4 of the length of the vortex structures downstream, which confirms that these two modes are associated with the same coherent vortex structures in the near wake.

Figure 4.16 shows the root mean square velocity fluctuations in the near wake reconstructed by the paired modes for the cases discussed above, which indicates the intensity of the coherent vortex structures in the near wake. As the crack increases to 2.0 mm, the strength of the coherent vortex structures increases significantly. On the other hand, for the same crack size, the strength of the coherent vortex structures decreases as the inflow turbulence is present or the angle of attack is increased.

In order to determine and compare the length scales, Λ, associated with the coherent vortex structures for different cases, a cross-correlation analysis [63] in the streamwise direction is performed for the paired POD modes of the vertical velocity component. As shown in Figure 4.17(a), assuming there are two paired modes, $\phi_{v,1}(x,y)$ and $\phi_{v,2}(x,y)$, the cross-correlation coefficient of the two modes with a displacement, Δx, is calculated within the dashed region as:

$$\sigma(\Delta x) = \frac{\sum \phi_{v,1}(x+\Delta x, y)\,\phi_{v,2}(x,y)}{|\phi_{v,1}(x+\Delta x, y)||\phi_{v,2}(x,y)|} \tag{4.6}$$

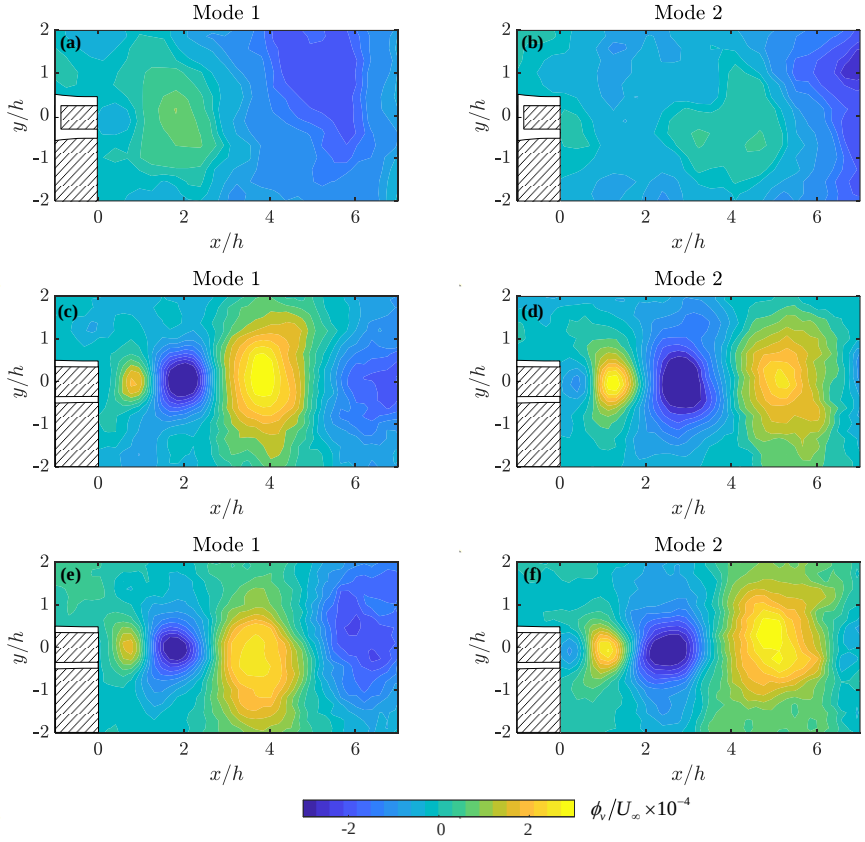

Figure 4.14: First two POD models of the v component for the cases: (a) and (b) 1.0 mm crack case for clean inflow condition; (c) and (d) 2.0 mm crack for clean inflow condition; (e) and (f) 2.0 mm crack for turbulent inflow condition. The white blocks are the trailing edges and the shaded sections are the shadow areas of the laser.

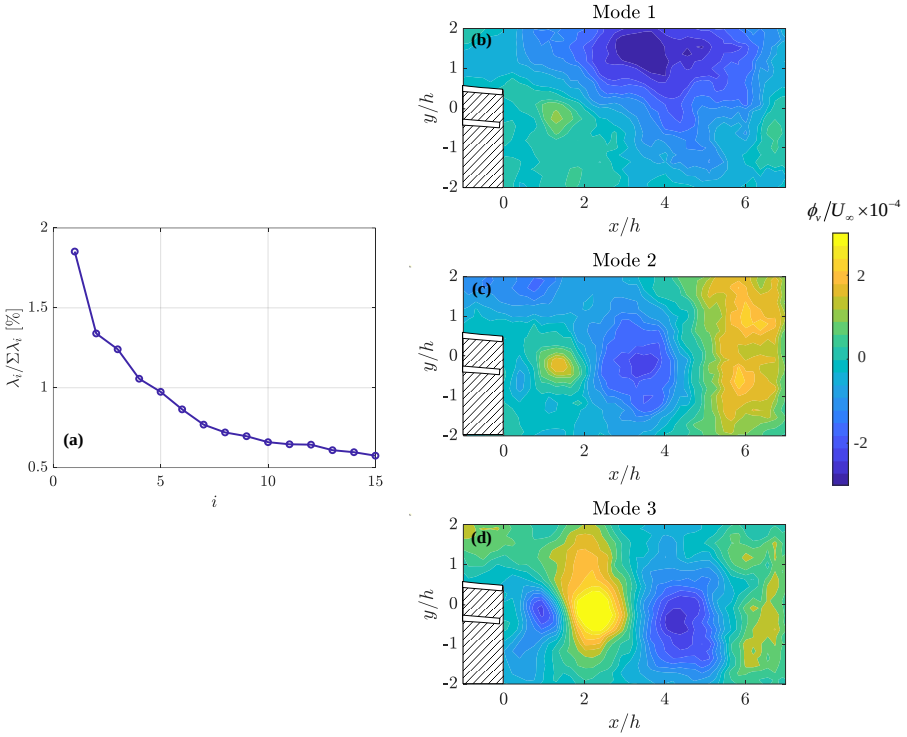

Figure 4.15: The energy distribution and first three modes for the case with a 2.0 mm crack at $\alpha = 5°$ ($\alpha^* = 2.4°$) for the clean inflow condition. The white blocks are the trailing edges and the shaded sections are the shadow areas of the laser.

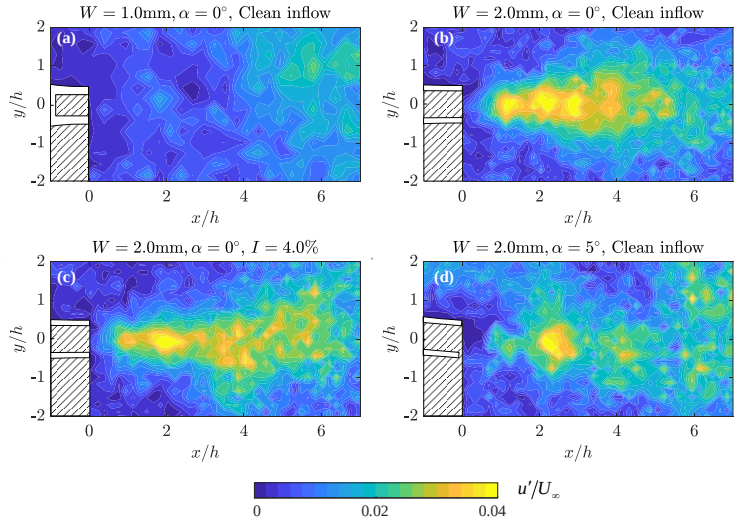

Figure 4.16: The fluctuations in the near wake reconstructed with the paired modes: (a) for 1.0 mm crack case and (b) (c) (d) for 2.0 mm crack cases for different conditions. The white blocks are the trailing edge and the shaded sections are the shadow areas of the laser.

Figure 4.17 (b) shows the cross-correlation coefficients of the paired modes for the 1.0 mm and 2.0 mm damage cases for different test conditions. The displacement is scaled with the trailing edge thickness, h. Due to the orthogonality of the POD modes, the cross-correlation coefficients for all the cases are all at zero when the displacement $\Delta x = 0$. The location of the first peak of cross-correlation coefficients indicates the 1/4 length of the coherent vortex structures and the location of the first valley indicates the 3/4 length of the coherent vortex structures. The location of the first peak of the cross-correlation coefficients for the case with the 1.0 mm crack is at $\Delta x/h = 2.6$ and it is greater than the one for the 2.0 mm crack cases at $\Delta x/h = 1.0$, which means the relative size of the coherent vortex structures is larger. However, for all the tested cases with a 2.0 mm crack, the locations of the first peak of the cross-correlation coefficients are close at $\Delta x/h \sim 1.0$, which makes it difficult to compare the sizes of vortex structures for these cases. The locations of the first valley for the 2.0 mm crack cases are at $\Delta x/h = 3.52$, 3.41 and 3.27 for the cases of clean inflow and zero angle of attack, turbulent inflow and zero angle of attack, clean inflow and $\alpha = 5°$ ($\alpha^* = 2.4°$), respectively. This suggests the length scale of the coherent vortex structures for the first case is slightly greater than the ones of the other two cases.

4.3.3. EFFECTS ON THE TONES OF TRAILING EDGE NOISE

The preceding analysis and discussion explained in detail how trailing edge crack and inflow turbulence alter the boundary layer properties and coherent vortex shedding at the trailing edge. This can further explain their influence on the shift of the tonal noise

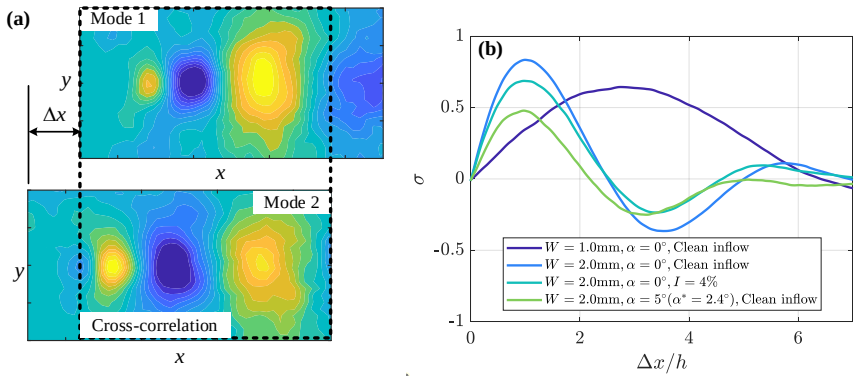

Figure 4.17: The fluctuations in the near wake reconstructed with the paired modes: (a) for 1.0 mm crack case and (b) (c) (d) for 2.0 mm crack cases of different conditions. The white blocks are the trailing edges and the shaded sections are the shadow areas of the laser.

peak. Figure 4.18 shows the relative sound pressure level, $\Delta L_p = L_p - L_{p,\text{Baseline}}$ (where ΔL_p and $L_{p,\text{Baseline}}$ are the sound pressure levels for the cracked and baseline cases under the same test condition), and the corresponding fitted curves of the spectra for the cases with different crack sizes and inflow conditions. The frequency is scaled using the trailing-edge-thickness-based Strouhal number, $St_h = fh/U_\infty$. The vortex shedding frequency depends on the convective velocity of vortex shedding and vortex length scale, i.e., $f = U_c/\Lambda$. Therefore St_h can be calculated as $St_h = \dfrac{U_c}{U_\infty}\dfrac{h}{\Lambda}$, which is proportional to the h/Λ assuming U_c/U_∞ is a constant. The spectral peak for the case with the crack size of $W = 2.0$ mm is narrower with a higher St_h at 0.1052 compared with the one for the damage case of $W = 1.0$ mm, which is at 0.085. This is because the strength of the coherent vortex structures is greater (as shown in Figure 4.16) and the relative length scale, Λ/h, is shorter (as shown in Figure 4.17) when the damage level increases as discussed above. Similarly, for the cases with a turbulent inflow or at a higher angle of attack, the intensity of the coherent vortex shedding is less and the vortex length scale, Λ, is shorter, which leads to a tone with a lower amplitude and higher frequency in the spectrum. As the velocity increases, the amplitude of the tonal peak increases and the location of the tonal peak shifts to a higher value of St_h. This is attributed to a greater velocity gradient in the boundary layer and thus stronger coherent vortex structures with slightly shorter length scales in the near wake. A similar result was observed in some numerical and experimental studies [64, 65], where the ratio of the vortex structure length to tailing edge thickness, Λ/h, slightly shifts to a higher value as the Reynolds number increases.

As suggested by Brooks et al. [38], the distribution of the Strouhal number, $St_{h,\text{peak}}$, as a function of $h/\bar{\delta}^*$, where $\bar{\delta}^*$ is the averaged boundary layer displacement thickness between the pressure side and suction side, $\bar{\delta}^* = \left(\delta_\text{p}^* + \delta_\text{s}^*\right)$, for $h/\bar{\delta}^* \geq 0.2$, follows the semi-empirical law:

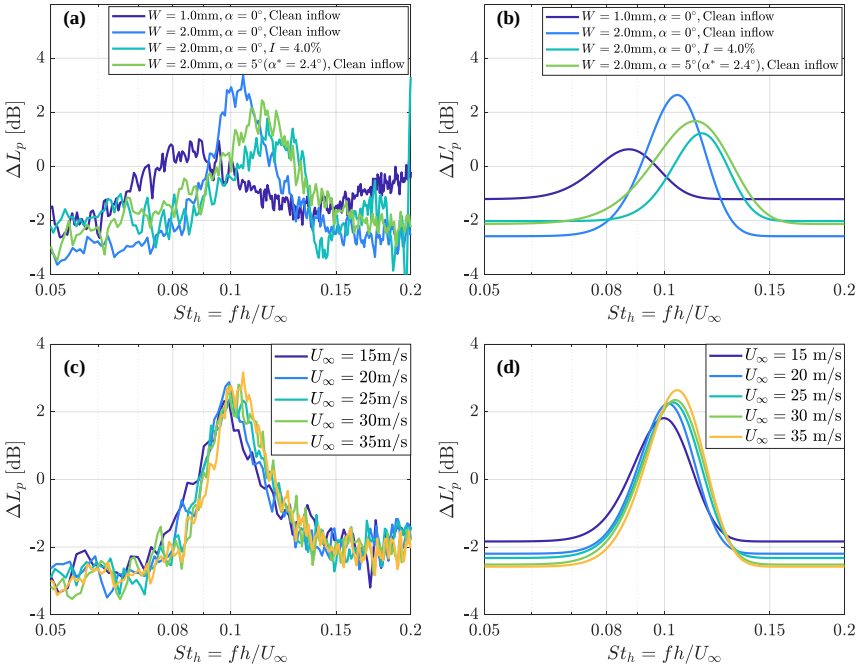

Figure 4.18: Relative sound pressure level ΔL_p and the corresponding fitted curves for different cases: (a) with inflow velocity of U_∞ = 35 m/s ; (b) with inflow velocity of U_∞ = 35 m/s (fitted); (c) at different velocities with clean inflow; (d) at different velocities with clean inflow (fitted).

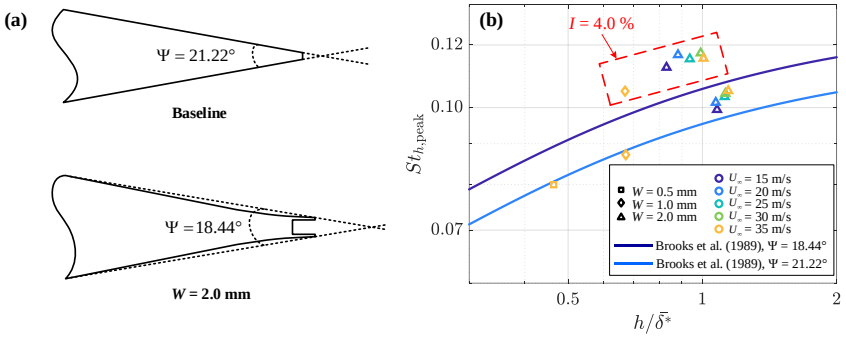

Figure 4.19: Comparison with the model developed by Brooks et al.: (a) definition of solid angle for baseline and cracked cases; (b) dependence of the peak Strouhal number versus the ratio of trailing edge thickness to boundary layer displacement thickness. The points outside the dashed box are for clean inflow cases. Solid lines are obtained using the semi-empirical law reported by Brooks et al. for the two different values of the solid angle shown in (a).

$$St_{h,\text{peak}} = \frac{0.212 - 0.0045\Psi}{1 + 0.235\left(h/\bar{\delta}^*\right)^{-1} - 0.0132\left(h/\bar{\delta}^*\right)^{-2}} \tag{4.7}$$

where Ψ is the solid angle (in degrees) between the sloping surfaces upstream of the trailing edge as defined in the reference paper and shown in the upper illustration of Figure 4.19(a). In the present work, the solid angle is 21.22° for the baseline airfoil. As the crack is present, due to the change in geometry at the trailing edge, an equivalent solid angle is defined as shown in the lower illustration of Figure 4.19(a). As the crack size increases, the effective solid angle slightly decreases and is estimated to be equal to 20.94°, 20.54°, 19.83° and 18.44° for the four crack cases, 0.2 mm, 0.5 mm, 1.0 mm and 2.0 mm, respectively.

Figure 4.19(b) reports the measured $St_{h,\text{peak}}$, where the frequency of the tonal peak is determined using the fitting procedure shown in Figure 4.18. As described above, the tonal peak cannot be accurately determined for all cases and therefore these points are excluded from the figure. The two solid lines in Figure 4.19(b) are obtained by plotting the Strouhal number determined using Equation 4.7 with solid angles equal to 18.44° (for 2.0 mm crack case) and 21.22° (for the baseline case). Data for the clean inflow cases lie between the two lines, showing consistency with the model. It is interesting to note that as the crack size increases, the measured $St_{h,\text{peak}}$ is in agreement with the model. However, for the W = 2.0 mm case, the measured $St_{h,\text{peak}}$ values do not quite coincide with the upper line corresponding to the solid angle of 18.44°. This might be because the reduction in the effective solid angle as a function of the crack size is slightly overestimated in the lower illustration of Figure 4.19(a).

When the inflow is turbulent, the measured $St_{h,\text{peak}}$ shifts to higher values for all the investigated cases. This is because the inflow turbulence affects the boundary layer velocity gradients and therefore the amplitude and frequency of the coherent vortex shedding as discussed previously. Although there is an offset with respect to the data for the clean inflow cases, the distribution of measured points for the turbulent inflow cases seems to follow the same trend line as for the clean inflow case. This suggests that the model developed by Brooks et al. [38] can capture the variation in Strouhal number as a function of crack size, albeit some correction is required for turbulent inflow. This result is significant because it suggests that the model could be used for practical applications. The exact correction will require further work.

4.4. SUMMARY

In this chapter, the trailing edge noise and the velocity fields near the trailing edge surface and near wake were measured for a NACA 0018 airfoil with different sizes of cracks at the trailing edge. This is done in order to investigate the relationship between the variations in the aerodynamic field and the far-field noise. The airfoil self-noise was measured by a phased microphone array. With the help of beamforming and source power integration techniques, the contributions of the trailing edge noise were obtained. The measurements for velocity fields near the surfaces of the trailing edge and the near wake were carried out using a PIV technique. A POD method was used to identify the dominant vortex structures from the velocity field data.

When the inflow is clean, the velocity gradient within the boundary layer increases as the crack size increases. As a result, the boundary layer thickness and displacement thickness decreases. When a turbulent inflow is introduced, compared with the same test configuration for the clean inflow condition, a similar trend of change in the boundary layer velocity profile in the inner region was observed: as the damage level increases the velocity gradient in the boundary layer becomes greater. The difference from the clean cases is that at the edge of the boundary layer, the slope of the velocity profile ($\mathrm{d}y'/\mathrm{d}U$) decreases in the presence of turbulent inflow thus a greater velocity gradient is present compared with the same case with clean inflow.

As the crack size increases, the coherent vortex structures in the near wake have greater intensities and shorter relative length scales Λ/h. This results in the shift of the tonal peak to a higher nondimensional frequency, St_h, with higher amplitude for a larger crack (with a blunter trailing edge). When the turbulent inflow is introduced, the shapes of coherent vortex structures in the near wake seem to be deformed with a slightly smaller size, which leads to the tonal peak slightly shifting to a higher value of St_h.

As expected, as the inflow velocity increases, for the same crack configuration, the boundary layer velocity gradient near the wall becomes greater for both clean and turbulent inflow conditions which leads to a thinner boundary layer thickness and displacement thickness. Also, when the airfoil is set at a higher angle of attack ($\alpha = 5°$, $\alpha^* = 2.4°$), the boundary layer velocity gradient becomes less on the suction side and greater on the pressure side, respectively, compared with the zero angle of attack case, which agrees with the findings in the previous studies [56]. This also changes the formation of the coherent vortex shedding and thus the tone in the noise spectrum.

The current experimental data for both clean and turbulent inflow conditions fit well with the trend of the previous model found in Reference [38] using the relationships between the $St_{h,\mathrm{peak}}$ and $h/\bar{\delta}^*$. This suggests that the model is still valid for the cases with a trailing edge crack. However, when the inflow is turbulent, the frequencies of the tonal peaks shift to higher values. This suggests it is necessary to consider a correction term for the turbulent inflow conditions for the estimation of the crack size or trailing edge thickness when using the suggested prediction model.

It should be noted that, in this study, the geometry of the trailing edge crack is simplified and idealized. In the real world, trailing edge damage is diverse, leading to more complicated changes in shape at the trailing edge. As can be seen from this study, the geometry of the trailing edge can alter the local boundary layer properties, vortex shedding and consequent aerodynamic noise. This suggests that it may require a specific analysis for a certain type of damage. However, the general methodology and technical route provided in this study can be used to investigate similar problems.

REFERENCES

[1] S. Watson, A. Moro, V. Reis, et al. Future emerging technologies in the wind power sector: A European perspective. *Renewable and Sustainable Energy Reviews* **113** (2019), 109270.

[2] D. Li, S. C. M. Ho, G. Song, L. Ren, and H. Li. A review of damage detection methods for wind turbine blades. *Smart Materials and Structures* **24** (2015).

[3] B. Yang and D. Sun. Testing, inspecting and monitoring technologies for wind turbine blades: A survey. *Renewable and Sustainable Energy Reviews* **22** (2013), 515–526.

[4] L. Bartolomé and J. Teuwen. Prospective challenges in the experimentation of the rain erosion on the leading edge of wind turbine blades. *Wind Energy* **22** (2019), 140–151.

[5] A. Sareen, C. A. Sapre, and M. S. Selig. Effects of leading edge erosion on wind turbine blade performance. *Wind Energy* **17** (2014), 1531–1542.

[6] M. Rosemeier, A. Krimmer, A. Bardenhagen, and A. Antoniou. Tunneling crack initiation in trailing-edge bond lines of wind-turbine blades. *AIAA Journal* **57** (2019), 5462–5474.

[7] J. Wang, X. Huang, C. Wei, et al. Failure analysis at trailing edge of a wind turbine blade through subcomponent test. *Engineering Failure Analysis* **130** (2021).

[8] C. C. Ciang, J. R. Lee, and H. J. Bang. Structural health monitoring for a wind turbine system: A review of damage detection methods. *Measurement Science and Technology* **19** (2008).

[9] F. Papi, L. Cappugi, S. Perez-Becker, and A. Bianchini. Numerical modeling of the effects of leading-edge erosion and trailing-edge damage on wind turbine loads and performance. *Journal of Engineering for Gas Turbines and Power* **142** (2020), 1–12.

[10] J. S. Chou, C. K. Chiu, I. K. Huang, and K. N. Chi. Failure analysis of wind turbine blade under critical wind loads. *Engineering Failure Analysis* **27** (2013), 99–118.

[11] Y. Ou, E. N. Chatzi, V. K. Dertimanis, and M. D. Spiridonakos. Vibration-based experimental damage detection of a small-scale wind turbine blade. *Structural Health Monitoring* **16** (2017), 79–96.

[12] A. Sarrafi, Z. Mao, C. Niezrecki, and P. Poozesh. Vibration-based damage detection in wind turbine blades using Phase-based Motion Estimation and motion magnification. *Journal of Sound and Vibration* **421** (2018), 300–318.

[13] B. Moynihan, B. Moaveni, S. Liberatore, and E. Hines. Estimation of blade forces in wind turbines using blade root strain measurements with OpenFAST verification. *Renewable Energy* **184** (2022), 662–676.

[14] D. Xu, P. F. Liu, and Z. P. Chen. Damage mode identification and singular signal detection of composite wind turbine blade using acoustic emission. *Composite Structures* **255** (2021).

[15] X. Y. Zhang, B. Zhou, H. Li, and W. Xin. Depth detection of spar cap defects in large-scale wind turbine blades based on a 3D heat conduction model using step heating infrared thermography. *Measurement Science and Technology* **33** (2022).

[16] S. Hwang, Y. K. An, J. Yang, and H. Sohn. Remote Inspection of Internal Delamination in Wind Turbine Blades using Continuous Line Laser Scanning Thermography. *International Journal of Precision Engineering and Manufacturing - Green Technology* **7** (2020), 699–712.

[17] E. Nieuwenhuizen and M. Köhl. Differences in noise regulations for wind turbines in four European countries. *Euronoise 2015* (2015), 333–338.

[18] T. Lutz, A. Herrig, W. Würz, M. Kamruzzaman, and E. Krämer. Design and wind-tunnel verification of low-noise airfoils for wind turbines. *AIAA Journal* **45** (2007), 779–785.

[19] L. E. Jones and R. D. Sandberg. Numerical analysis of tonal airfoil self-noise and acoustic feedback-loops. *Journal of Sound and Vibration* **330** (2011), 6137–6152.

[20] J. Gill, X. Zhang, and P. Joseph. Symmetric airfoil geometry effects on leading edge noise. *The Journal of the Acoustical Society of America* **134** (2013), 2669–2680.

[21] F. Avallone, D. Casalino, and D. Ragni. Impingement of a propeller-slipstream on a leading edge with a flow-permeable insert: A computational aeroacoustic study. *International Journal of Aeroacoustics* **17** (2018), 687–711.

[22] L. T. Lima Pereira, D. Ragni, F. Avallone, and F. Scarano. Aeroacoustics of sawtooth trailing-edge serrations under aerodynamic loading. *Journal of Sound and Vibration* **537** (2022), 117202.

[23] M. Herr and J. Reichenberger. In search of airworthy trailing-edge noise reduction means. *17th AIAA/CEAS Aeroacoustics Conference 2011 (32nd AIAA Aeroacoustics Conference)* (2011), 5–8.

[24] L. Rossian, A. Suryadi, M. Herr, R. Ewert, and J. Delfs. Effect of Porous Materials on the Acoustic Emissions of a Circulation-Control High-Lift Airfoil (2020).

[25] C. Teruna, F. Avallone, D. Casalino, and D. Ragni. Numerical investigation of leading edge noise reduction on a rod-airfoil configuration using porous materials and serrations. *Journal of Sound and Vibration* **494** (2021), 1–25.

[26] A. Rubio Carpio, F. Avallone, D. Ragni, M. Snellen, and S. Van Der Zwaag. Mechanisms of broadband noise generation on metal foam edges. *Physics of Fluids* **31** (2019).

[27] O. Ferret Gasch, S. Oerlemans, B. W. Faßmann, et al. Trailing edge noise prediction of wind turbine airfoils: A benchmark exercise. *25th AIAA/CEAS Aeroacoustics Conference, 2019* (2019), 1–23.

[28] S. Luesutthiviboon, L. T. L. Pereira, D. Ragni, F. Avallone, and M. Snellen. Aeroacoustic Benchmarking of Trailing-Edge Noise from NACA 633 –018 Airfoil with Trailing-Edge Serrations. *AIAA Journal* **61** (2023), 329–354.

[29] B. Chen, S. Yu, Y. Yu, and Y. Zhou. Acoustical damage detection of wind turbine blade using the improved incremental support vector data description. *Renewable Energy* **156** (2020), 548–557.

[30] F. P. García Márquez, P. J. Bernalte Sánchez, and I. Segovia Ramírez. Acoustic inspection system with unmanned aerial vehicles for wind turbines structure health monitoring. *Structural Health Monitoring* **21** (2022), 485–500.

[31] Y. Zhang, F. Avallone, and S. Watson. Wind turbine blade trailing edge crack detection based on airfoil aerodynamic noise: An experimental study. *Applied Acoustics* **191** (2022), 108668.

[32] Y. Zhang, F. Avallone, and S. Watson. An aeroacoustics-based approach for wind turbine blade damage detection. *Journal of Physics: Conference Series* **2265** (2022), 022088.

[33] D. Kim, G. S. Lee, and C. Cheong. Inflow broadband noise from an isolated symmetric airfoil interacting with incident turbulence. *Journal of Fluids and Structures* **55** (2015), 428–450.

[34] Y. Zhang, F. Avallone, and S. Watson. Leading edge erosion detection for a wind turbine blade using far-field aerodynamic noise. *Applied Acoustics* **207** (2023), 109365.

[35] T.F. Brooks and T.H. Hodgson. Trailing edge noise prediction from measured surface pressures. **78** (1981), 69–117.

[36] S. M. Hasheminejad, T. P. Chong, G. Lacagnina, et al. On the manipulation of flow and acoustic fields of a blunt trailing edge aerofoil by serrated leading edges. *The Journal of the Acoustical Society of America* **147** (2020), 3932–3947.

[37] S. Oerlemans. Wind turbine noise : primary noise sources (2011), 1–57.

[38] T. F. Brooks, D. S. Pope, and M. A. Marcolini. *Airfoil self-noise and prediction*. Vol. 1218. National Aeronautics and Space Administration, 1989.

[39] M. Kiya, H. Tamura, and M. Arie. Vortex shedding from a circular cylinder in moderate-Reynolds-number shear flow. *Journal of Fluid Mechanics* **141** (1980), 721–735.

[40] B. A. Younis and V. P. Przulj. Computation of turbulent vortex shedding. *Computational Mechanics* **37** (2006), 408–425.

[41] P. Sijtsma. Phased Array Beamforming Applied to Wind Tunnel and Fly-Over Tests. *SAE Technical Papers* **2010-Octob** (2010), 17–19.

[42] G. Berkooz, P. Holmes, and J. L. Lumley. The proper orthogonal, decomposition in the analysis of turbulent flows (1993).

[43] B. W. Van Oudheusden, F. Scarano, N. P. Van Hinsberg, and D. W. Watt. Phase-resolved characterization of vortex shedding in the near wake of a square-section cylinder at incidence. *Experiments in Fluids* **39** (2005), 86–98.

[44] R. Merino-Martínez, A. Rubio Carpio, L. T. Lima Pereira, et al. Aeroacoustic design and characterization of the 3D-printed, open-jet, anechoic wind tunnel of Delft University of Technology. *Applied Acoustics* **170** (2020).

[45] S. Oerlemans. Detection of aeroacoustic sound sources on aircraft and wind turbines (2009), 1–173.

[46] R. Merino-Martínez, P. Sijtsma, A. R. Carpio, et al. Integration methods for distributed sound sources. *International Journal of Aeroacoustics* **18** (2019), 444–469.

[47] Q. Ye, F. F. Schrijer, and F. Scarano. Boundary layer transition mechanisms behind a micro-ramp. *Journal of Fluid Mechanics* **793** (2016), 132–161.

[48] F. H. Clauser. The turbulent boundary layer. *Advances in applied mechanics* **4** (1956), 1–51.

[49] A. Rubio Carpio, R. Merino Martínez, F. Avallone, et al. Experimental characterization of the turbulent boundary layer over a porous trailing edge for noise abatement. *Journal of Sound and Vibration* **443** (2019), 537–558.

[50] G. D. Huffman and P. Bradshaw. A note on von Kármán's constant in low Reynolds number turbulent flows. *Journal of Fluid Mechanics* **53** (1972), 45–60.

[51] S. C. Bailey, M. Vallikivi, M. Hultmark, and A. J. Smits. Estimating the value of von Kármán's constant in turbulent pipe flow. *Journal of Fluid Mechanics* **749** (2014), 79–98.

[52] R. Maddahian, A. Kebriaee, B. Farhanieh, and B. Firoozabadi. Analytical investigation of boundary layer growth and swirl intensity decay rate in a pipe. *Archive of Applied Mechanics* **81** (2011), 489–501.

[53] K. A. Thole and D. G. Bogard. High freestream turbulence effects on turbulent boundary layers. *Journal of Fluids Engineering, Transactions of the ASME* **118** (1996), 276–284.

[54] B. Brzek, S. Torres-Nieves, J. Lebrn, et al. Effects of free-stream turbulence on rough surface turbulent boundary layers. *Journal of Fluid Mechanics* **635** (2009), 207–243.

[55] S. N. Sharp, S. Neuscamman, and Z. Warhaft. Effects of large-scale free stream turbulence on a turbulent boundary layer. *Physics of Fluids* **21** (2009).

[56] O. M. Fouatih, B. Imine, and M. Medale. Numerical/experimental investigations on reducing drag penalty of passive vortex generators on a NACA 4415 airfoil. *Wind Energy* **22** (2019), 1003–1017.

[57] T. Cebeci. *Short Cut Methods*. 2013, pp. 237–292.

[58] D. Yuan, J. Deng, R. Han, D. Li, and S. Tan. Experimental study on flow structures of central blockage accidents in a rectangular channel using PIV and POD. *Annals of Nuclear Energy* **153** (2021).

[59] Q. Zhang and Y. Liu. Influence of incident vortex street on separated flow around a finite blunt plate: PIV measurement and POD analysis. *Journal of Fluids and Structures* **55** (2015), 463–483.

[60] M. Stöhr, R. Sadanandan, and W. Meier. Phase-resolved characterization of vortex-flame interaction in a turbulent swirl flame. *Experiments in Fluids* **51** (2011), 1153–1167.

[61] Y. Yang, S. Pröbsting, Y. Liu, et al. Effect of dual vortex shedding on airfoil tonal noise generation. *Physics of Fluids* **33** (2021).

[62] H. Cao, T. Zhou, Y. Zhang, and M. Zhang. An experimental investigation of aerodynamic and aeroacoustic performance of a wind turbine airfoil with trailing edge serrations. **1211** (2022).

[63] B. Turhan, Z. Wang, and I. Gursul. Coherence of unsteady wake of periodically plunging airfoil. *Journal of Fluid Mechanics* **938** (2022), 1–32.

[64] B. Gibeau and S. Ghaemi. The mode B structure of streamwise vortices in the wake of a two-dimensional blunt trailing edge. *Journal of Fluid Mechanics* **884** (2019).

[65] G. Taherian, M. Nili-Ahmadabadi, M. H. Karimi, and M. R. Tavakoli. Flow visualization over a thick blunt trailing-edge airfoil with base cavity at low Reynolds numbers using PIV technique. *Journal of Visualization* **20** (2017), 695–710.

5

LEADING EDGE EROSION DETECTION

In this chapter, the feasibility of using far-field acoustic measurements as a non-contact monitoring technique for wind turbine blade leading edge erosion is assessed. For this purpose, a DU96 W180 airfoil with several eroded leading edge configurations of different severities is experimentally investigated. The eroded leading edges are designed with pits, gouges and coating delamination scaled from a real eroded blade. To assess the feasibility of the technique in quasi-realistic configurations, experiments are carried out under clean and turbulent inflow conditions. Acoustic measurements are performed with a phased microphone array. The experimental results suggest that the leading edge erosion modifies the transition process of the flow on the airfoil surface and increases the stagnation region in front of the leading edge thus providing different trailing edge or leading edge noise spectra compared with the baseline.

Parts of this chapter have been published in *Applied Acoustics* **207** (2023) [1].

5.1. INTRODUCTION

Leading edge erosion is one of the most observed damage types on wind turbine blades. During the operational life of a wind turbine, aside from the aging of the blades, raindrops or hail, and other solid particles, such as sand grains, are the principal external contributors to blade leading edge erosion [2–4]. At the very first stage, damage often appears as small, randomly distributed pits; then as the damage develops, larger-size gouges occur; these pits and gouges grow in size and density leading to coating delamination on the surface [5]. This results in a reduction in the lift of the blade, therefore a loss of power output [6–8].

Power conversion efficiency or turbine efficiency is often considered as a priority in the wind power industry. Therefore, most of the research on leading edge erosion has concentrated mainly on how the erosion affects the aerodynamic performance of the blades [5, 9–11]. However, it is essential to detect erosion and monitor the development of damage, not only to provide a reliable prediction of power output but more importantly to reduce potential operational risks for a wind farm. Therefore, the development of a reliable, flexible and low-cost damage detection technique is of high relevance to the wind power industry [12].

A few studies [2, 4, 13] have focused on the mechanism of erosion formation and growth aiming at building dynamic models to predict the potential lifetime of a blade and any consequential effect on the annual energy production. These models account for blade material properties, operational (e.g., wind and rotor speed) and environmental (sizes of raindrops or sands) conditions. They provide good predictions for blade lifetime and the timing for inspections but cannot be used for real-time monitoring. For the latter, detection approaches are mainly based on the measurements of vibrations [14], strain [15] or elastic waves (vibro-acoustic emission) [16] on the blade. Since the sensors are required to be mounted inside the blade in advance, these detection approaches cannot be easily applied to in-service wind turbines. Other non-contact approaches based on infrared thermography cameras [17] or laser scanners [18] are potentially easier to apply to existing wind turbines. Similarly, the measurements of audible sound (20 Hz to 20 kHz) in the far-field or inside the blade structures with microphones can also be used as an alternative for blade damage detection [19–22]. Those airborne-sound-based methods can be classified into two basic categories: the active excitation method [23, 24] and the passive excitation method [20, 22]. The former relies on far-field measurements for acoustic waves, which are originally excited by the speakers inside the blade structures, passing through the holes or cracks of the blades. The latter places the microphones inside the blade structures to measure the flow-induced pressure responses due to the leakage of flow from the holes or cracks into the blade cavity. Besides the above two approaches using airborne sound, another possible acoustic solution for damage detection can be based on airfoil self-noise or turbulence-leading-edge impingement noise measurements in the far-field, of which the mechanisms of the sound generation are essentially different from the speaker-based or cavity-flow-responses induced ones. Compared with a clean blade, an eroded one usually has a rougher surface near the leading edge and a smaller thickness and radius at the leading edge due to the coating shedding [3, 5, 25]. These geometrical changes in airfoil shape and surface roughness may affect the noise generated aerodynamically both at the leading edge and trailing edge. Previous

studies, that have used aerodynamic noise measurements for damage detection [26–29], have been based on data-driven methods. However, the physical interpretation of the measured acoustic signal and the mechanism of the sound generation have not been investigated extensively nor related to the types and sizes of damage. Such data-driven models derived from existing databases may not be reliable when applied to new operating conditions, blade structures or damage severity. Several studies [30–32] have used a modified surface roughness to emulate blade erosion and assess its effect on the far-field noise. However, roughness tapes attached to airfoil surfaces cannot exactly mimic leading edge erosion, as in reality an eroded airfoil sees a reduced thickness as well as a roughened surface. Other numerical studies [33, 34] have also investigated the effects of blade icing accretion on noise generation and far-field noise emission.

At low Reynolds numbers, i.e., at the blade inner radial locations, a laminar separation bubble may exist under clean inflow conditions. In this case, boundary layer instabilities in the form of Tollmien–Schlichting (T-S) waves can be triggered and an acoustic feedback loop can take place [35]. This phenomenon creates tonal noise known as laminar-boundary-layer–vortex-shedding noise [36–38]. The presence of small surface discontinuities due to erosion can affect the formation and development of the instabilities, thus causing different noise spectra in the far field. Furthermore, if the surface roughness or damaged region due to the erosion is large, the laminar separation bubble might not be present, and the boundary layer might develop directly into a fully turbulent one thus leading to broadband turbulent-boundary-layer-trailing-edge noise [30, 39–41]. From a physical perspective, the damaged surface near the leading edge may force the boundary layer transition location to move towards the leading edge, thus affecting the turbulent boundary layer approaching the trailing edge and, as a consequence, affecting the spectra of the scattered turbulent-boundary-layer-trailing-edge noise.

In this chapter, the aerodynamic noise characteristics are experimentally investigated with and without free-stream turbulence, when leading edge erosion occurs. A DU96 W180 airfoil with different leading edge erosion levels with pits, gouges and coating delamination scaled from a real eroded blade is tested in an anechoic wind tunnel. The aerodynamic noise scattered from the airfoil is measured and analyzed and a physical interpretation behind the acoustic data is postulated. Major differences between experiments carried out in a wind tunnel environment and real life are: the Reynolds number, often low in aeroacoustics facilities; and the presence of turbulence in the wind farm. Because of the former, an acoustic feedback loop might not be present in large wind turbines close to the tip of the blades, but only on the inner part of the blade. Considering the latter point, the presence of free-stream turbulence can cause turbulence leading edge impingement noise [42–45]. Previous studies revealed that there is a dependence between the wavelength of the free-stream turbulence, the leading edge radius and the thickness of the airfoil [42, 46–51]. Furthermore, the effect of flow turbulence can potentially hinder the effect of leading edge erosion on transition, thus raising the possibility of assessing erosion from far-field noise measurements. For this reason, this chapter also investigates this aspect, which is poorly analyzed in the literature so far.

The rest of this chapter is organized as follows. In Section 5.2, the details of the facilities, test models and data processing configurations are presented. In Section 5.3, the

results of acoustic measurements for different erosion levels are reported together with the physical interpretation of the noise generation mechanism. In this section the effects of erosion features, airfoil angle of attack and mean flow velocity on the noise spectra are discussed. The last section summarizes the findings from this chapter and proposes an outlook for future studies.

5.2. EXPERIMENTAL SETUP AND TEST CONDITIONS

5.2.1. FACILITIES AND TEST MODELS

Experiments were performed in the anechoic vertical open-jet tunnel (A-tunnel) of Delft University of Technology. The wind tunnel is equipped with a 40 cm × 70 cm rectangular test section, which allows a test with a maximum free-stream velocity of 45 m/s with turbulence intensity below 0.1%. The mean flow velocity non-uniformity within the whole test section is below 0.5% with respect to the velocity at the center [52]. The experimental setup is shown in Figure 5.1.

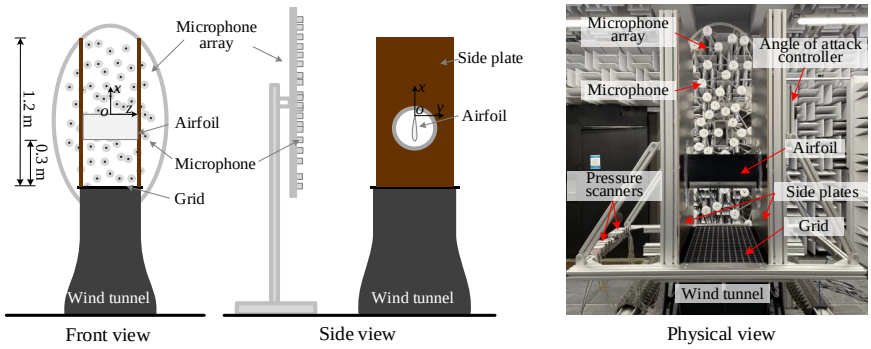

Figure 5.1: Experimental setup.

Two grids (#1 and #2) were used to generate turbulence for moderate and high turbulence conditions. Inflow turbulence intensity and integral length scales with two grids mounted were measured using hotwire anemometry in Chapter 2 and previous work [53] and are reported in Table 5.1.

Table 5.1: Turbulence intensity and integral length scale of the flow with grid mounted.

Grid No.	Turbulence intensity (%)	Turbulence integral length scale (mm)
1	4.0	7.9
2	7.1	10.2

A DU96 W180 airfoil was investigated. The profile of this airfoil was designed at Delft University of Technology for wind energy applications [54–56]. The airfoil model was

made of aluminum by computer numerical control (CNC) machining (surface roughness: 0.05 mm) with a chord length, C, of 200 mm and span length, L, of 400 mm, as shown in Figure 5.2. The leading edge is changeable which allows the testing of different erosion cases as well as a baseline (without any damage).

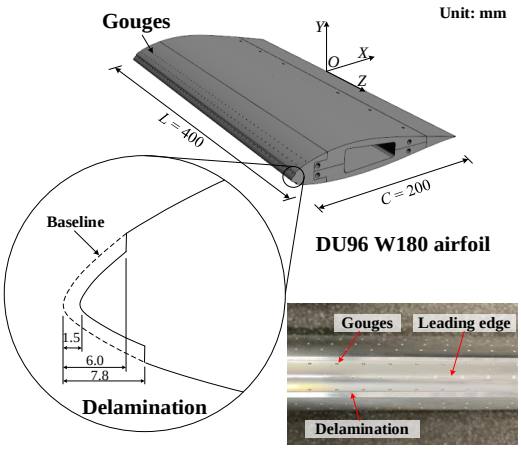

Figure 5.2: Airfoil and leading edge erosion model: an example for damage level 4.

A global *o-xyz* Cartesian coordinate system is defined. The origin is located at the trailing edge mid-span of the airfoil. The x-axis is oriented with the direction of the free-stream, as shown in Figure 5.1. An airfoil-based Cartesian reference system, *O-XYZ*, is also defined with origin at the trailing edge mid-span and X-axis oriented in the direction of the airfoil chord, as shown in Figure 5.2.

Due to the experiments being performed in an open test section, the effective angle of attack, α^*, of the airfoil is smaller than the geometrical angle of attack, α [36]. The effective angle of attack was obtained using the surface pressure distributions and compared with the data from XFOIL [57]. The static pressure was measured with two pressure scanners connected to sixteen pressure taps with 0.4 mm diameter on both pressure and suction side. The taps are distributed within the range of $-0.99 \leq X/C \leq -0.175$, tilted 15° to the airfoil centerline to avoid the contamination of the wakes from upstream taps on the downstream ones. The sampling frequency and accuracy of the pressure scanner are 100 Hz and 12.5 Pa, respectively. For each measurement, pressure data were recorded for 2 s. Figure 5.3 shows the relationships between the calculated coefficient of lift, C_l, and the angle of attack from the measurement and XFOIL for 20 m/s free stream velocity. The correction factor, η, can be calculated from the slope ratio of the fitted curve from XFOIL to the one from the measurements, i.e., $\eta = 0.0829/0.1073 = 0.773$.

The design for the leading edge erosion is based on the measurements of eroded blades from 3M [5] and the damage sizes are scaled to the airfoil used in this study. The leading edge erosion contains pits (P), gouges (G) and coating delamination (DL). The

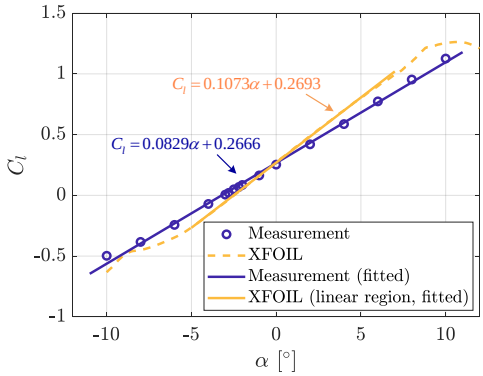

Figure 5.3: Coefficient of lift versus angle of attack from measurement and XFOIL.

simulated pits (with depth and diameter of 0.2 mm) and gouges (with depth and diameter of 1.0 mm) are simplified as hollow cylinders and the coating delamination is simulated as a sunken offset with 1.5 mm depth to the baseline surface at the leading edge. The pits and gouges are staggered and distributed within $-200\text{mm} \leq X \leq -180\text{mm}$ on the suction side and $-200\text{mm} \leq X \leq -174\text{mm}$ on the pressure side, respectively. The chordwise extension ranges of the coating delamination are from the leading edge up to 2, 4, and 6 mm on the suction side and 2.6, 5.2, and 7.8 mm on the pressure side for different delamination severities (DL, DL+ and DL++). The distributed range of damage features on the pressure side is 1.3 times the one on the suction side, as suggested in [5], which takes into account that the pressure side of a real blade is vulnerable to more severe erosion. The detailed dimensions and distributed range of the erosion features are shown in Table 5.2.

Four erosion levels are designed with different combinations of erosion features. Table 5.3 shows the amounts of pits or gouges and the severity of delamination for different damage levels. Considering the fact that the scaled dimension of the pits is far smaller than gouges and delamination, the effect of those pits on aerodynamic noise emission will be negligible, thus the pits were not manufactured for the simulated erosion cases (Level 1 ~ 4). Alternatively, in order to investigate the separate influence of the pits, gouges and delamination on the noise emission, three additional leading edge parts with a single type of erosion feature were manufactured. In Figure 5.2, an example of the geometry and real test leading edge of damage level 4 is shown.

5.2.2. PHASED MICROPHONE ARRAY AND ACOUSTIC MEASUREMENTS

Far-field noise was measured using a 2-D planar phased microphone array which contained 64 *G.R.A.S. 40PH* free-field microphones. The microphone array was placed at $y = -1$ m, as shown in Figure 5.1. The distribution of the microphones in the array is shown in Figure 5.4. The reference microphone was set at (0.2, -1, 0) m to ensure all microphones being out of the acoustic shadow of the wind tunnel nozzle. The frequency

Table 5.2: Dimensions and distributed range of erosion features.

Features	Depth/Diameter (mm)	Damaged range (mm)	
		Pressure side	Suction side
Pits (P)	0.2 (0.1% C)	26 (13% C)	20 (10% C)
Gouges (G)	1.0 (0.5% C)	26 (13% C)	20 (10% C)
Delamination (DL)	1.5 (0.75% C), depth	2.6, 5.2, 7.8 (1.3%, 2.6%, 3.9% C) for DL, DL+, DL++	2, 4, 6 (1.0%, 2.0%, 3.0% C) for DL, DL+, DL++

Table 5.3: Dimensions and distributed range of erosion features.

	Damage case		Erosion features	
No.	Description		Pressure side	Suction side
0	Baseline		-	-
1	Simulated erosion	Level 1	30G	25G
2		Level 2	65G/DL	50G/DL
3		Level 3	130G/DL+	100G/DL+
4		Level 4	260G/DL++	200G/DL++
5	Decoupled features from level 4		520P	400P
6			260G	200G
7			DL++	DL++

response of the microphone is within ±1 dB between 50 Hz and 5 kHz, and within ±2 dB between 5 kHz and 20 kHz. The maximum measurable range of the microphone is 135 dB with respect to the reference pressure of 20 μPa.

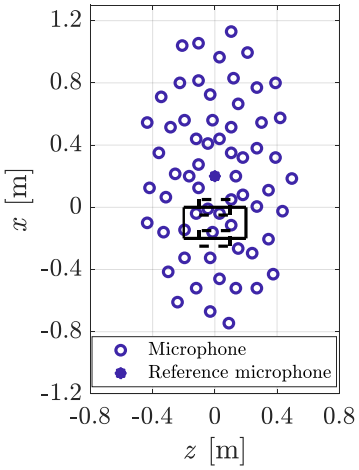

Figure 5.4: Microphones in the array. The solid box is the projection of the airfoil onto the array plane and the top or bottom dashed box is the corresponding source power integration region at the leading edge or trailing edge, respectively.

The acoustic signal of each test case was recorded for 20 s with a sampling frequency, f_S, of 51.2 kHz. For each measurement, the signal was separated into time chunks of 5120 samples with 50% data overlap for the Fourier transform. For each chunk, a Hanning weighting function was applied to reduce the energy leakage. The cross-spectral matrix was averaged from the obtained auto spectra of the Fourier transform. Conventional frequency domain beamforming (CFDB) [58–62] introduced in Chapter 2 was performed on a square scan plane parallel to the *xoz* plane, ranging: $-0.5\text{m} \leq x \leq 0.5\text{m}$ and $-0.5\text{m} \leq z \leq 0.5\text{m}$. The distance between the microphone array and scan plane was corrected with the airfoil angle of attack (at non-zero). The background noise from the wind tunnel test section and turbulence generating grids was measured under the same test condition before the airfoil was mounted. Then the background noise was reduced by means of the eigenvalue identification and subtraction (EIS) algorithm [62] reported in Chapter 2. A source power integration (SPI) technique [63, 64] was applied within a rectangular box (as shown in Figure 5.4) with a size of 10 cm × 10 cm centered at the midpoint of the leading edge or trailing edge to look at the noise scattered from the regions of interest.

The noise spectrum in this study is quantified using the sound pressure level (SPL) which is defined as:

$$L_p = 10\log\left(\frac{p'^2}{p_0^2}\right) \tag{5.1}$$

where p' is the root mean square sound pressure fluctuations and p_0 is the reference pressure, 20 μPa in air.

5.2.3. SURFACE OIL FLOW VISUALIZATION

To investigate the effect of erosion on flow transition on the airfoil surfaces, surface oil flow visualization [65] was carried out. The setup is shown in Figure 5.5(a). A fluorescing oil mixture was made of paraffin oil and petroleum. The mixture was brushed on the airfoil surface and then fluorescence was excited with an ultra-violet (UV) lamp. Pictures were taken by a digital camera. The distribution of this oil film was affected by shear forces and the change in the velocity gradient of flow, induced by laminar or turbulent boundary layers or other features. As an example, flow separation is visualized [66, 67] in Figure 5.5(b).

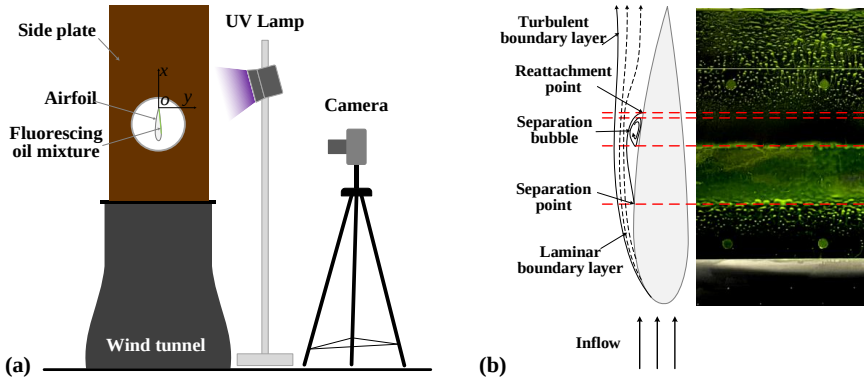

Figure 5.5: Setup of surface oil flow visualization: (a) a sketch; (b) an example and interpretation for oil visualization of damage level 2 under clean flow condition with a mean flow velocity of 30 m/s (picture was taken on the suction side at an angle of attack of 0°).

5.2.4. TEST CONDITIONS

The experiments were carried out under five different inflow velocities. The mean flow velocity and relevant chord-length-based Reynold numbers ($Re_C = U_\infty C/\nu$, where ν is kinematic viscosity) are shown in Table 5.4. For each mean flow velocity, three inflow conditions were tested: clean inflow and turbulent inflow obtained by mounting one of two different grids.

Five angles of attack were selected to investigate the effect of the airfoil angle of attack on the ability to detect erosion under zero lift, zero angle of attack, low angle of attack, pre-stall and stall conditions. The geometrical angles of attack and the corresponding effective ones are listed in Table 5.5.

Table 5.4: Test conditions of mean flow velocities and Reynolds numbers.

No.	1	2	3	4	5
U_∞ (m/s)	15	20	25	30	35
Re_C	2.0×10^5	2.7×10^5	3.4×10^5	4.1×10^5	4.7×10^5

Table 5.5: The angles of attack tested in the experiment.

No.	1 ($C_l = 0$)	2 ($\alpha = 0°$)	3 (low)	4 (pre-stall)	5 (stall)
α (°)	-3.2	0	5	10	15
α^* (°)	-2.5	0	3.8	7.7	11.6

5

5.3. RESULTS AND DISCUSSION

5.3.1. IDENTIFICATION OF EROSION LEVEL

CLEAN INFLOW CONDITION

Figure 5.6 shows the spectra of sound pressure level at the trailing edge measured with the microphone array facing both the suction and pressure side for different damage levels for the clean inflow case. The angle of attack is 0°, the free-stream velocity 30 m/s. When there is no damage (baseline) or the damage is small (e.g., damage level 1), at a low Reynolds number, laminar boundary layer instability noise can be observed. The noise spectra typically show the combination of a broadband hump with a series of tonal peaks [35, 68–71]. Both on the suction and pressure side, the broadband contributions of the damage level 1 do not show many differences compared with the baseline case, both in amplitude and frequency. However, on the suction side, the amplitude of the tones for damage level 1 is larger than that for the baseline. For example, the amplitudes of the dominant tones are 48.36 dB ($f_{n,\max}$ at 1800 Hz) for damage level 1 and 41.25 dB ($f_{n,\max}$ at 1830 Hz) for the baseline case, respectively. This is attributed to a change in the size of the laminar separation bubble, which becomes longer on the suction side with respect to the baseline case. This is confirmed by the surface oil flow visualization technique shown in Figure 5.7. On the suction side, since the separation bubble is larger and closer to the trailing edge, more coherent vortices are shed near the trailing edge, thus resulting in larger tonal noise [38, 72–74]. Figure 5.6 also shows the spectra normalized by chord-length-based Strouhal number, St_C. For the damage level 1 case, the dominant tone occurs at $St_C = 12$ on the suction side and $St_C = 10.2$ on the pressure side and the baseline cases at $St_C = 12.2$ and $St_C = 10.2$, respectively. The frequency of the dominant tones does not change in the presence of a small amount of damage. For the baseline case, there is also a secondary harmonic tone on the suction side at $St_C = 5.9$, while, for the damage level 1 case, there is not. Similar results are reported in [72], where the tones on the suction side and pressure side lock on to the same frequency (and the same St_C) for the NACA 0012 airfoil. The asymmetry of the DU96 W180 airfoil may be responsible for the difference (i.e., a smaller peak St_C on the pressure side) between the results of

this study and in [72].

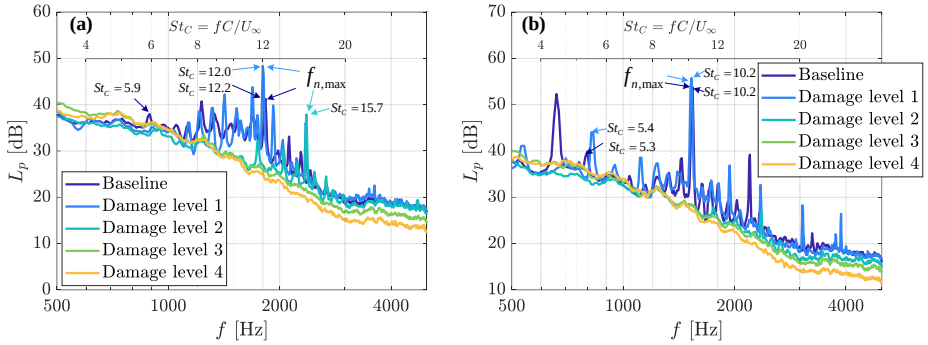

Figure 5.6: Spectra of sound pressure level at the tailing edge for different damage levels at the angle of attack of 0° under clean flow condition with the mean flow velocity of 30 m/s: (a) on the suction side and (b) on the pressure side.

5

When the damage becomes larger, for example damage level 2, on the pressure side, the flow is turbulent right after the eroded region as shown in Figure 5.7, thus resulting in broadband far-field noise as shown in Figure 5.6. A small tone appears at $St_C = 15.7$ and might be due to the noise scattered from the feedback loop present on the suction side. On the suction side, a similar spectral shape to the damage 1 case is found. The major difference is that the amplitude is lower and both the broadband hump and the tonal peaks shift to a higher frequency region. As a matter of fact, the dominant tone is found at $St_C = 15.7$ for the damage level 2 case, while it is at $St_C = 12.2$ for the damage level 1 case. Previous studies observed similar trends when forcing transition on the pressure side [72, 75].

When the damage level becomes even larger (e.g., damage levels 3 and 4), the spectra both on the suction and pressure side show only broadband features (Figure 5.7). Surface oil flow visualization results of those cases, as shown in Figure 5.6, confirm that the boundary layer is turbulent on both sides. However, when comparing the spectra, the overall trend is that as the damage level is larger, there is an energy increase in the low-frequency range and a decrease in the high-frequency one. The potential cause for this spectral shape is that a larger damage area leads to more large-scale turbulence structures and a thicker boundary layer at the trailing edge; as a result, the energy is redistributed to a lower frequency region.

TURBULENT INFLOW CONDITIONS

In the presence of a turbulent inflow, as shown by the beamforming maps in Figure 5.8, three different noise sources can be identified: one from the grid, one from the airfoil leading edge and one from the trailing edge. The noise generated by the grid strongly increases the background noise, thus affecting the quality of the measurement. To reduce the contribution from the grid, the signal processing approach discussed in Section 5.2.2 has been applied. Furthermore, data are presented only below 2000 Hz to keep a high ratio of airfoil noise to grid background noise.

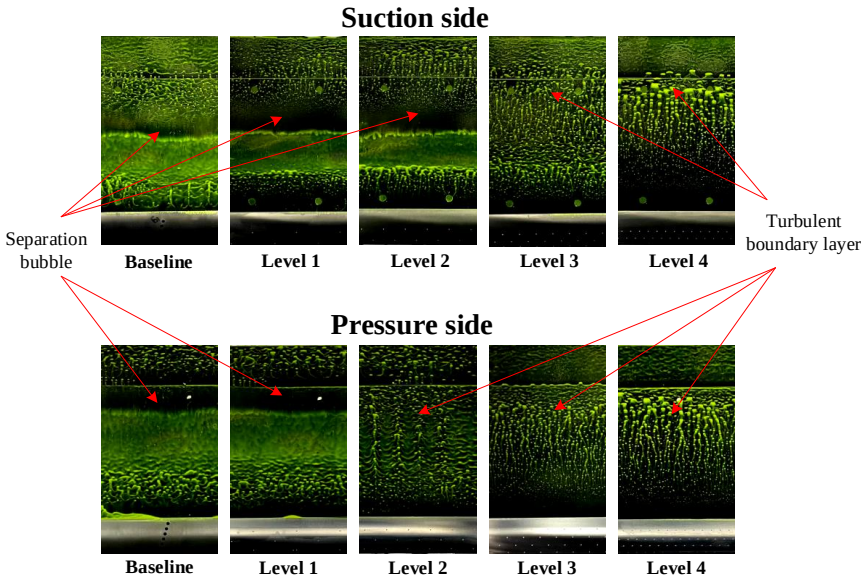

Figure 5.7: Surface oil flow visualization for different damage levels at the angle of attack of 0° under a clean flow condition with the mean flow velocity of 30 m/s.

Figure 5.9 shows the sound pressure level at the trailing edge for different damage cases as well as the baseline when grid #1 is mounted for the mean flow velocity of 30 m/s and airfoil angle of attack of 0°. Due to the turbulent inflow, the boundary layer transition to turbulent very close to the leading edge, as shown in Figure 5.10. Therefore, the noise scattered from the trailing edge can be attributed to the trailing edge turbulent boundary layer noise mechanism. However, in this condition, for all the presented cases, there is no difference between the far-field noise generated at the trailing edge. This means that damage detection using the trailing edge noise is not a valid approach.

At the leading edge, where turbulent inflow impingement noise occurs, the noise spectrum presents a decaying trend above 1000 Hz both on the pressure and suction side when the damage level increases, as shown in Figure 5.11(a) and (b). Figure 5.11(c) and (d) show the relative spectral differences from the baseline, $\Delta L_p = L_{p,\text{Baseline}} - L_{p,\text{Damage}}$, against chord-length-based Strouhal number St_C. The spectral difference shows a hump with increasing amplitude as the damage level increases. The frequency at which the hump reaches its maximum is nearly constant for all the cases at $St_C \sim 10$. Previous studies [42, 51, 76] focusing on the effects of leading edge radius and airfoil thickness on the turbulent inflow impingement noise, attributed the reduction in the high-frequency range to the larger distortion of the turbulent velocity in the larger stagnation region [77], because the distortion of the turbulent structures is related to the slope angle of the steady mean flow near the leading edge. To confirm this, a 2-D RANS numerical calculation is performed using Ansys Fluent CFD software platform. The standard $k-\epsilon$

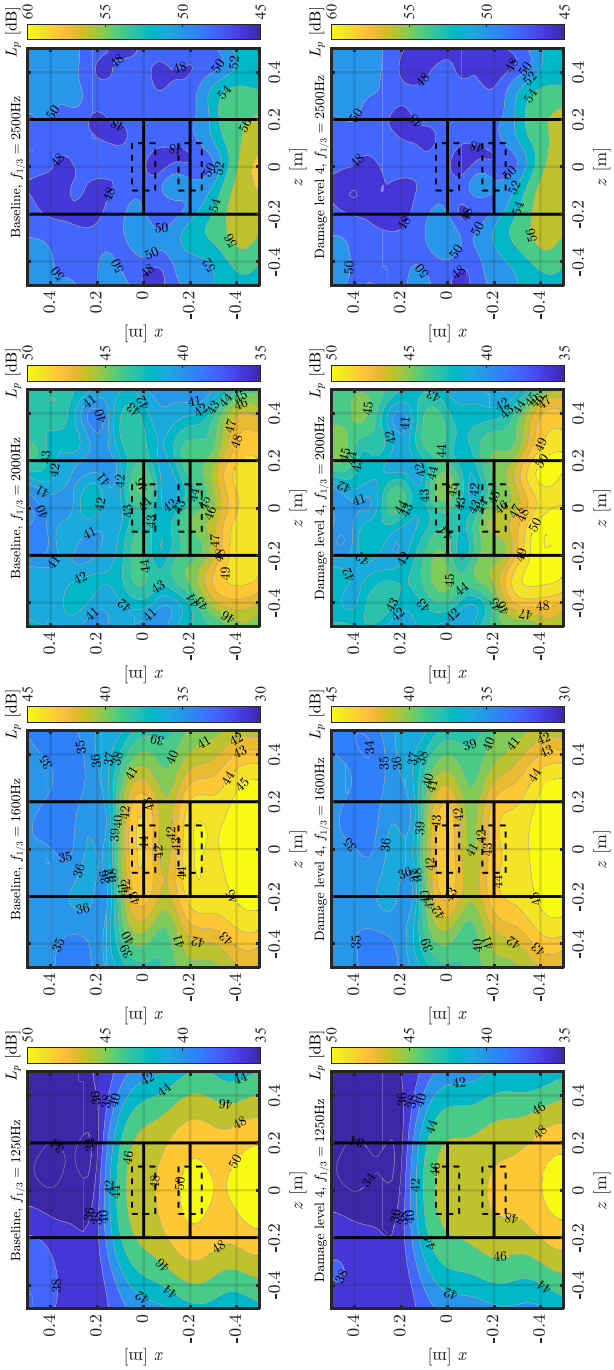

Figure 5.8: Beamforming maps on the suction side at one-third octave central frequency from 1250 Hz to 2500 Hz with grid #1 mounted when the flow velocity is 30 m/s at 0° angle of attack for baseline and damage level 4.

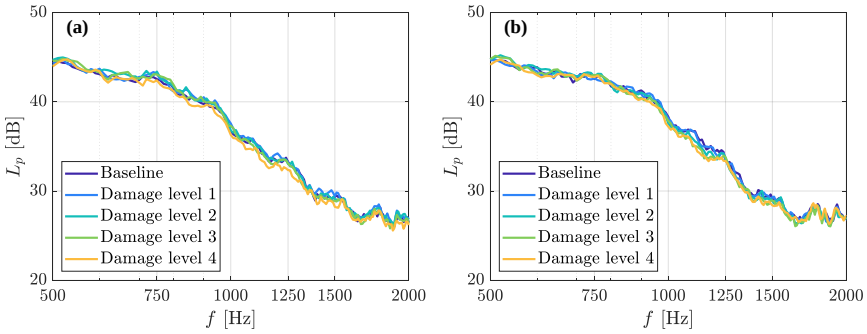

Figure 5.9: Spectra of sound pressure level at the trailing edge for different damage levels at an angle of attack of 0° when grid #1 is mounted with a mean flow velocity of 30 m/s: (a) on the suction side and (b) on the pressure side.

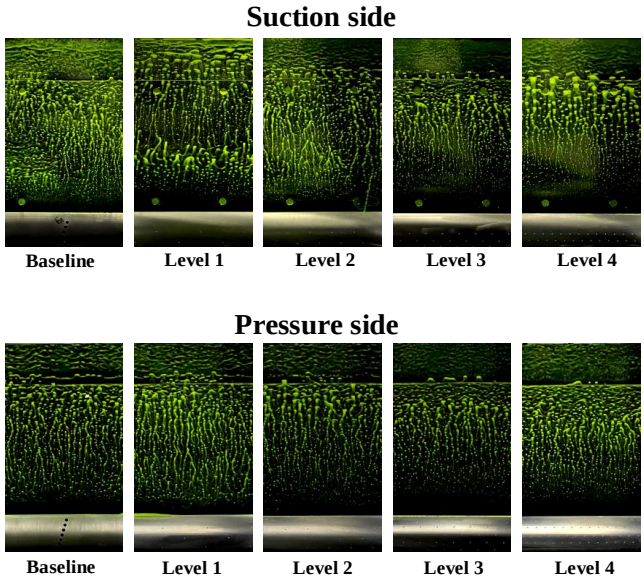

Figure 5.10: Surface oil flow visualization for different damage levels at an angle of attack of 0° when grid #1 is mounted with a mean flow velocity of 30 m/s.

two-equation turbulence model is used in the simulation providing a reasonable compromise between calculation speed and accuracy. Figure 5.12 shows numerical results for the mean velocity around the leading edge for baseline and damage level 4 under the same condition as in the experiments. The region where the mean velocity is lower than 80% of inflow velocity is determined as the stagnation region. The result shows that for the damage level 4 case, there is a larger stagnation region with larger mean flow curvature compared with the baseline, particularly due to the steps introduced to mimic the erosion damage under investigation.

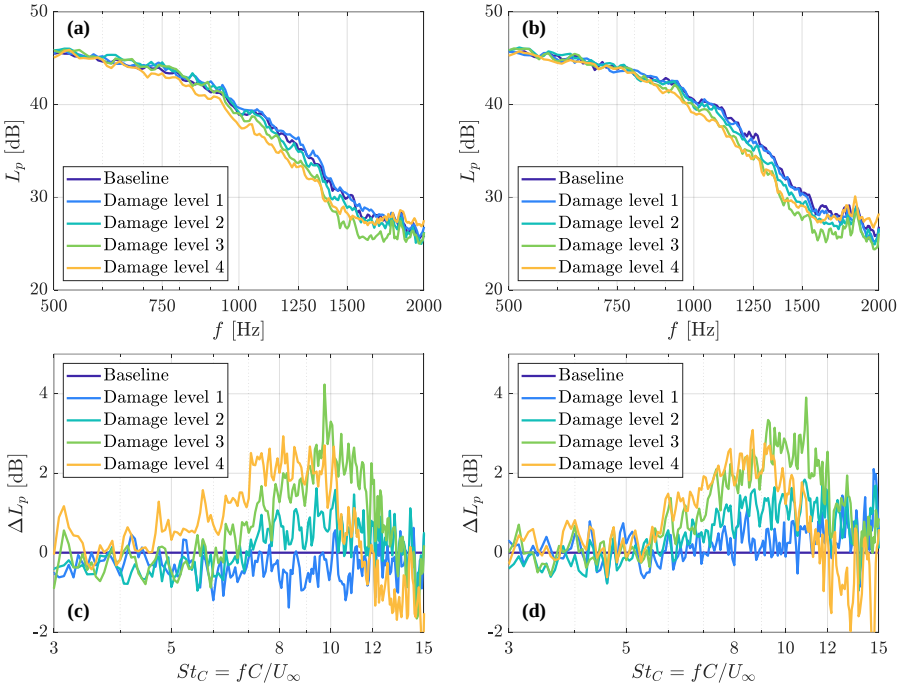

Figure 5.11: Spectra of sound pressure level and spectral differences compared to the baseline at the leading edge for different damage levels at an angle of attack of 0° when grid #1 is mounted with a mean flow velocity of 30 m/s: (a), (c) on the suction side and (b), (d) on the pressure side.

Figure 5.13 presents the spectra of sound pressure level when grid #2 is mounted, where the turbulence intensity is at ~ 7.1%. Similar results to the previous case can be observed but the spectral differences between those cases become smaller. This means the turbulent inflow with high turbulence intensity may reduce the sensitivity for damage detection by analyzing the spectra of leading edge noise.

5.3.2. EFFECT OF EROSION FEATURES

The eroded leading edge investigated contains three features: pits, gouges, and delamination. In this section, we take erosion level 4 as an example to investigate the effect of

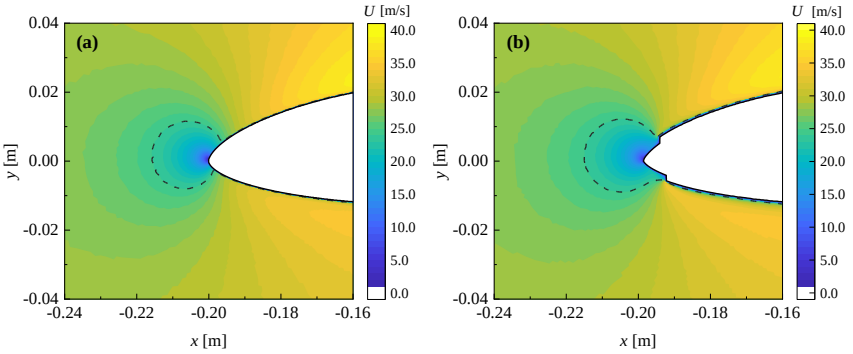

Figure 5.12: Mean velocity around the leading edge for baseline and damage level 4 at the angle of attack of 0° under inflow mean velocity of 30 m/s with grid #1 mounted: (a) baseline and (b) damage level 4. The region bounded by the dashed line is below 80% inflow mean velocity, i.e., 24 m/s, representing the stagnation region.

5

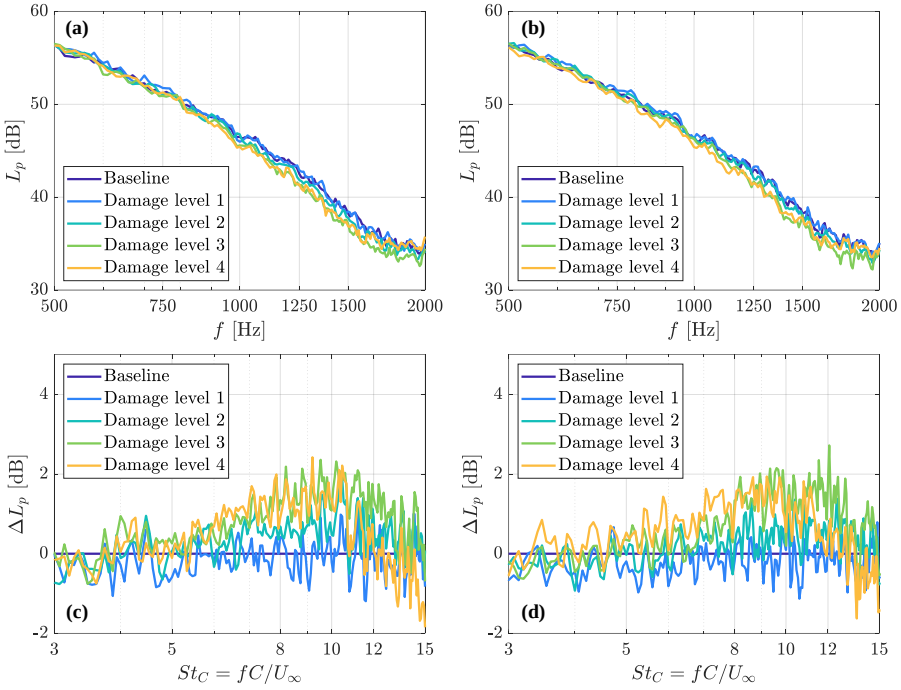

Figure 5.13: Spectra of sound pressure level and spectral differences compared to the baseline at the leading edge for different damage levels at an angle of attack of 0° when grid #2 is mounted with a mean flow velocity of 30 m/s: (a), (c) on the suction side and (b), (d) on the pressure side.

different erosion features on the far-field noise. In Figure 5.14, the spectra of the trailing edge noise for each of the isolated features present in case 4 are investigated under clean inflow conditions. The spectra of the cases with pits and gouges show laminar boundary layer instability noise characteristics. On the suction side, the discrete tones caused by the gouges case are significantly higher than the one measured for the baseline and pits-only cases; as a matter of fact, the dominant tones for the cases of gouges, pits and baseline are 56.66 dB, 45.49 dB and 41.25 dB, respectively. Conversely, on the pressure side, no clear trend is observed. The spectra of the delamination case on the suction side and pressure side are essentially consistent with the ones of damage level 4.

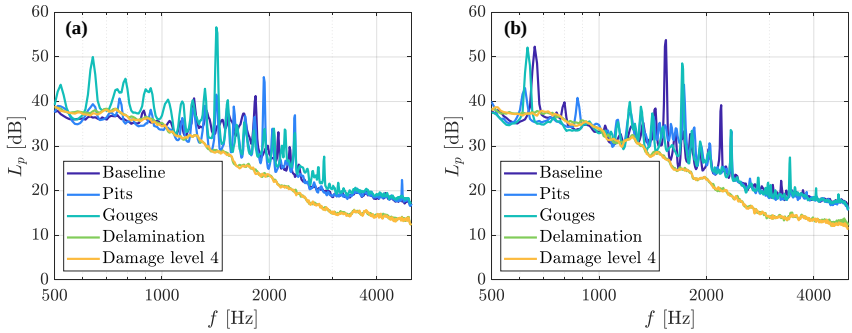

Figure 5.14: Spectra of sound pressure level at trailing edge for baseline, damage level 4 and its different erosion features at angle of attack of 0° under clean flow condition with mean flow velocity of 30 m/s: (a) on suction side; (b) on pressure side.

In Figure 5.15, the spectra for the leading edge noise under the turbulent inflow conditions (with grid #1 mounted) are shown. The spectra of cases of pits and gouges almost coincide with the baseline while the spectra of the delamination case tend to the ones of damage level 4, in agreement with the physical explanation provided in the previous section. This suggests that both under clean and turbulent conditions, the delamination feature of the erosion dominates the nature of the noise spectra.

5.3.3. EFFECT OF AIRFOIL ANGLE OF ATTACK

In Figure 5.16, the spectra of sound pressure level for the trailing edge noise under a clean inflow condition for the damage level 4 case and the baseline case at different angles of attack are shown. For the baseline configuration, at a low ($\alpha = -3.2°, 0°, 5°$) or moderate ($\alpha = 10°$, pre-stall) angle of attack, the spectra are characterized by laminar boundary layer instability noise. The tonal components are enhanced with increasing angle of attack both on the suction and pressure side. For the highest angle of attack investigated ($\alpha = 15°$, stall), where the airfoil is operating under stall conditions, the far-field noise spectra show broadband features with an increase of noise in the low frequency range with respect to other angles of attack. This is caused by the large vortices present in the separated boundary layer. By contrast, for the case of damage level 4, when the airfoil is at a low ($\alpha = -3.2°, 0°, 5°$) and moderate ($\alpha = 10°$) angle of attack, the spectra

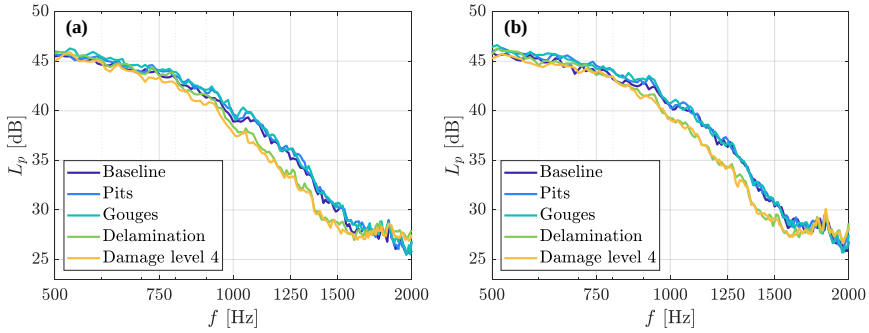

Figure 5.15: Spectra of sound pressure level at the leading edge for baseline, damage level 4 and its different erosion features at an angle of attack of 0° under mean flow velocity of 30 m/s with grid #1 mounted: (a) on the suction side; (b) on the pressure side.

show broadband turbulent boundary layer noise characteristics, similarly to what was observed in the previous section. Moreover, on both the suction side and pressure side, the intensity of noise in the low-frequency range increases while it decreases in the high-frequency range as the angle of attack increases. In contrast to the baseline case, when the airfoil is at $\alpha = 15°$, the spectra for the damaged case show higher noise intensity in the low frequency region and lower noise intensity in the high frequency region compared with the baseline case.

When turbulent inflow is introduced, the noise from the leading edge rather than the trailing edge contains the effective information for the identification of damage as discussed before. In this case, the spectra of the leading edge noise are discussed under turbulent inflow conditions. With grid #1 mounted, as shown in Figure 5.17, the variation in the angle of attack does not affect the leading edge impingement noise under low and moderate angles of attack ($\alpha = -3.2°, 0°, 5°, 10°$) for both the baseline and damage level 4 cases. By comparing the two configurations for these angles of attack, it is evident that above 1000 Hz, the sound levels of the damaged cases are consistently lower compared with those of the baseline, independent of the angle of attack. However, for a stall condition, this trend is opposite. The above results suggest that the change in the angle of attack does not affect the ability to recognize damage and the proposed approach is valid under a wide range of airfoil angles of attack.

5.3.4. EFFECT OF MEAN FLOW VELOCITY

Figure 5.18(a) and (b) show the sound pressure level of trailing edge noise under a clean inflow condition with different velocities for damage level 4. The spectra of the noise for both sides are broadband under these testing velocities. Figure 5.18(c) presents the overall sound pressure level (OSPL) against the flow velocities. The OSPL is integrated between 500 Hz and 5000 Hz. As expected, the OSPL shows an approximate fifth power law of velocity dependency(5.16 and 5.19 on suction and pressure sides, respectively).

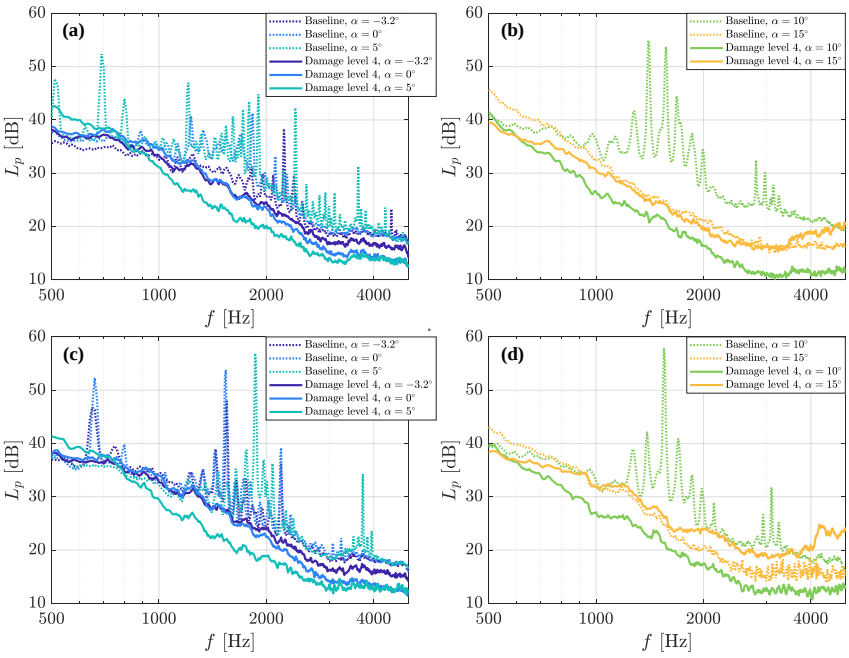

Figure 5.16: Spectra of sound pressure level of trailing edge noise for different angles of attack under clean flow condition with inflow velocity of 30 m/s: (a) and (b) on the suction side; (c) and (d) on the pressure side.

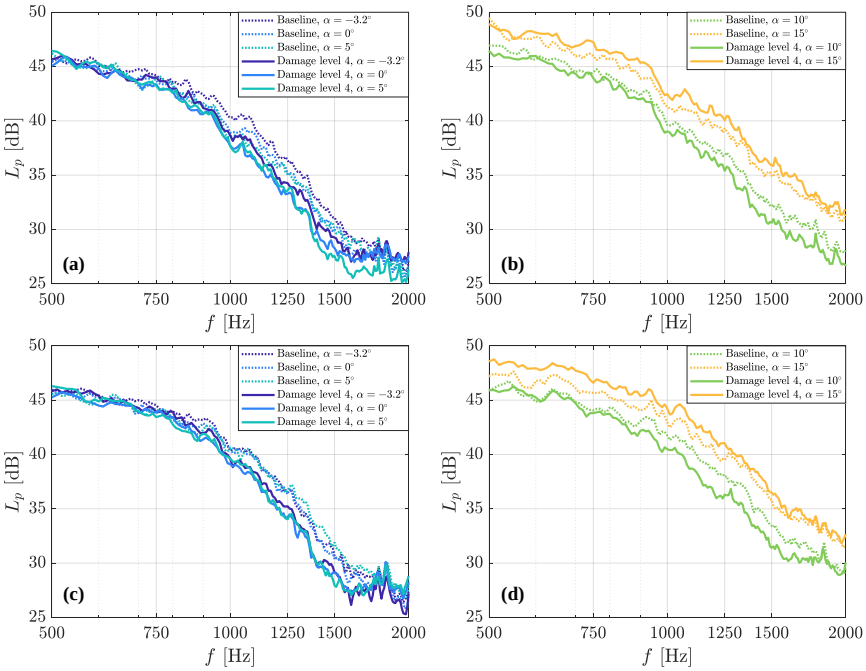

Figure 5.17: Spectra of sound pressure level of leading edge noise for different angles of attack under turbulent flow condition with grid #1 mounted and mean flow velocity of 30 m/s: (a) and (b) on the suction side; (c) and (d) on the pressure side.

This is consistent with previous studies on turbulent boundary layer trailing edge noise [32, 36, 78].

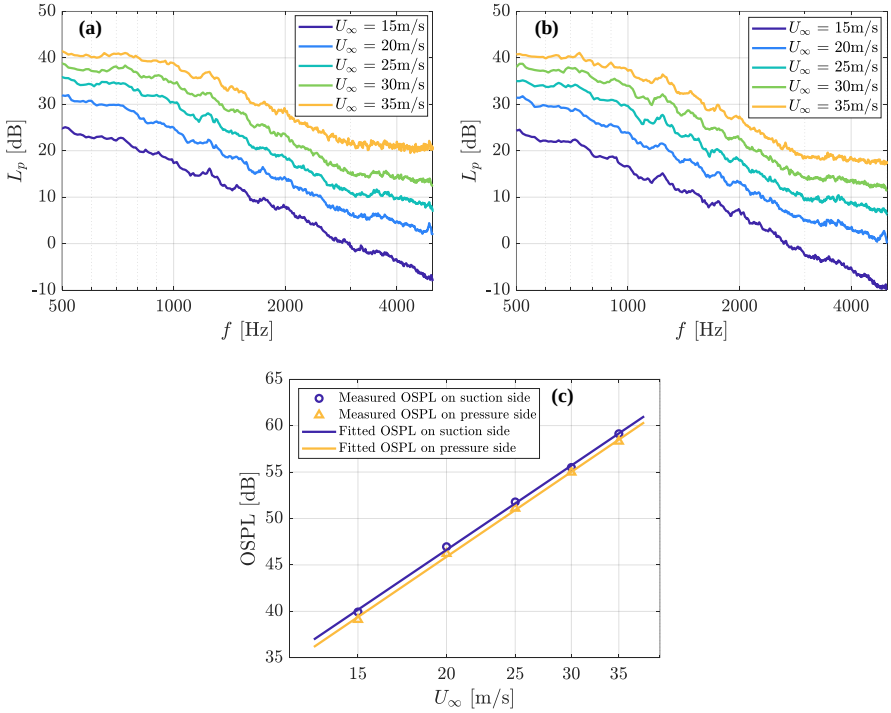

Figure 5.18: Sound pressure level of trailing edge noise for damage level 4 under clean inflow condition with different velocities at the angle of attack of 0°: (a) spectra on the suction side; (b) spectra on the pressure side; (c) overall sound pressure level to mean flow velocity.

When inflow is turbulent, the spectral features of leading edge impingement noise can be used for damage detection. Figure 5.19 shows the spectra of the leading edge impingement noise for damage level 4 and baseline as well as their spectral differences (i.e., $\Delta L_p = L_{p,\text{Baseline}} - L_{p,\text{Damage}}$) under different mean flow velocities when grid #1 is mounted. Compared with the baseline, in Figure 5.19(a) and (b), the spectrum of the damage level 4 is lower within a specific band under a given velocity. Moreover, the region with lower noise intensity shifts to high frequency as the mean flow velocity increases. When normalizing the frequency as chord-length-based Strouhal number, the peaks of ΔL_p are all approximately at $St_C \sim 10$, which suggests a proportional relation between the spectral features and the velocity. Moreover, when looking at the amplitudes of ΔL_p, the change in velocity does not affect the detection sensitivity.

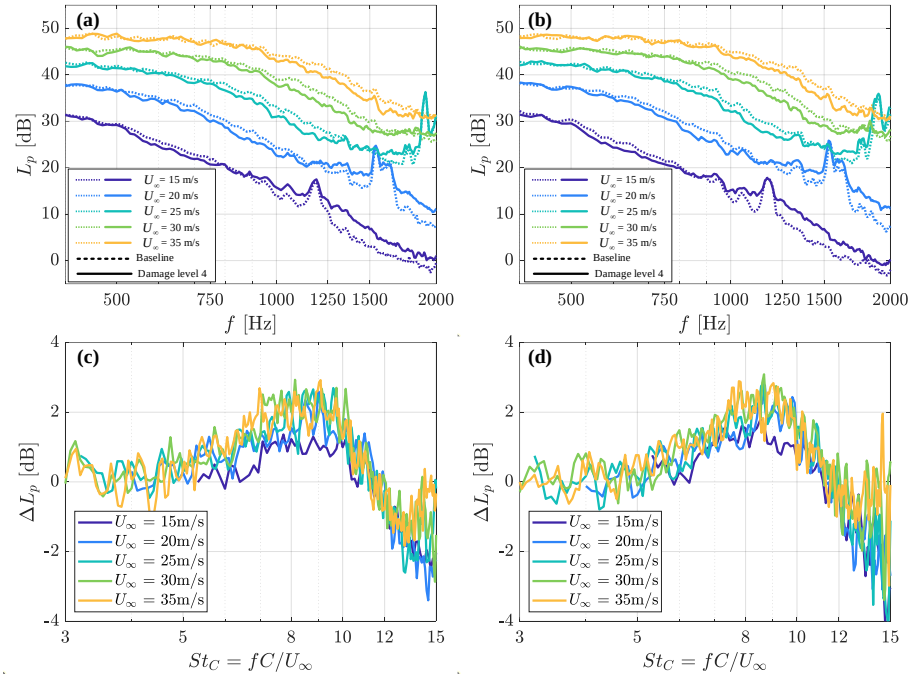

Figure 5.19: Sound pressure level of leading edge noise and spectral differences to the baseline for damage level 4 under different mean flow velocity with grid #1 mounted at the angle of attack of 0°: (a) and (c) on the suction side; (b) and (d) on the pressure side.

5.4. SUMMARY

In this chapter, the aerodynamic noise of a DU96 W180 airfoil with leading edge erosion was investigated for the purpose of the development of a non-contact approach for damage detection and condition monitoring for wind turbine blades. The experimental results showed that it is possible to use the spectral features of trailing edge noise under a clean flow condition and leading edge noise under turbulent conditions for erosion damage detection.

Under a clean inflow condition and low Reynolds number, when the damage level is minor (e.g., damage level 1), the frequencies of the tones do not change while the amplitude becomes higher than those of the baseline case. When at a moderate damage level (damage level 2), the tones can only be found from noise spectra on the suction side, and they shift to a higher frequency region with lower amplitudes. Furthermore, when the damage level is larger (damage levels 3 and 4), the noise scattered from the trailing edge becomes broadband and as the damage level increases the low-frequency contributions increase while the high-frequency contributions decrease.

Under turbulent inflow conditions, however, the spectra of the trailing edge noise for different damage cases are almost the same. This suggests that it is invalid to use the trailing edge noise for leading edge erosion detection. As the damage level increases, mid-high frequency contributions of the leading edge impingement noise decreases. This is because a greater level of erosion leads to a larger distortion of the incoming turbulent eddies. When the turbulence intensity increases, the differences in impingement noise between the different damage levels become smaller which suggests that for a high turbulence condition the detection may be affected.

The effects of erosion features, airfoil angle of attack and mean flow velocity were also investigated. By comparing spectral results of each isolated erosion feature at damage level 4 (pits, gouges and coating delamination) and the baseline, it is found that the delamination dominates the noise emission. When the airfoil angle of attack is changed, the spectral differences between the damaged case and the baseline are still present from zero lift to stall condition. This indicates that the method is still valid with variable angles of attack. Under turbulent conditions with different mean flow velocities, the reduction in frequency of the impingement noise for the damage case against the baseline is directly proportional to mean flow velocity and the flow velocity does not affect spectral differences between the damage case and baseline.

The experiments were carried out using airfoil models but the conclusions derived from this study are expected to be valid when extend to rotating systems. This relies on the fact that the rotation does not essentially change the mechanisms of the noise generation [79]. However, in real applications, the blades may encounter more complicated situations, for example, the accretion of ice or pollution of the insects or dust on the leading edge. In this case, the noise spectra might be similar to the ones due to the leading edge erosion, which suggests that additional measurements or techniques may be needed for the damage recognition. Further investigations on the small wind turbines in the wind tunnel and in-service wind turbines in wind farms will be carried out in the future. It is worth noting that the experiment was conducted under low Reynolds numbers. In a real application, laminar boundary layer instability noise can be difficult to detect between the middle and tip sections of the blades. Thus, the conclusions derived

from the laminar boundary layer instability noise mechanism in this study may only be applied to the blade root section. On the other hand, the turbulence length scales of the turbulent inflow may affect the reduction frequency of the impingement noise. In this study, the turbulence length scales of the turbulent flow when two grids were mounted were of a similar magnitude (~ 10 mm) thus the effect of the turbulence length scale was not discussed in this thesis and is suggested to be investigated in the future.

REFERENCES

[1] Y. Zhang, F. Avallone, and S. Watson. Leading edge erosion detection for a wind turbine blade using far-field aerodynamic noise. *Applied Acoustics* **207** (2023), 109365.

[2] H. M. Slot, E. R. Gelinck, C. Rentrop, and E. Van der Heide. Leading edge erosion of coated wind turbine blades: Review of coating life models. *Renewable Energy* **80** (2015), 837–848.

[3] L. Bartolomé and J. Teuwen. Prospective challenges in the experimentation of the rain erosion on the leading edge of wind turbine blades. *Wind Energy* **22** (2019), 140–151.

[4] H. Law and V. Koutsos. Leading edge erosion of wind turbines: Effect of solid airborne particles and rain on operational wind farms. *Wind Energy* **23** (2020), 1955–1965.

[5] A. Sareen, C. A. Sapre, and M. S. Selig. Effects of leading edge erosion on wind turbine blade performance. *Wind Energy* **17** (2014), 1531–1542.

[6] W. Han, J. Kim, and B. Kim. Effects of contamination and erosion at the leading edge of blade tip airfoils on the annual energy production of wind turbines. *Renewable Energy* **115** (2018), 817–823.

[7] K. Latoufis, V. Riziotis, S. Voutsinas, and N. Hatziargyriou. Effects of Leading Edge Erosion on the Power Performance and Acoustic Noise Emissions of Locally Manufactured Small Wind Turbine Blades. *Journal of Physics: Conference Series* **1222** (2019).

[8] F. Papi, L. Cappugi, S. Perez-Becker, and A. Bianchini. Numerical modeling of the effects of leading-edge erosion and trailing-edge damage on wind turbine loads and performance. *Journal of Engineering for Gas Turbines and Power* **142** (2020), 1–12.

[9] N. Gaudern. A practical study of the aerodynamic impact of wind turbine blade leading edge erosion. *Journal of Physics: Conference Series* **524** (2014).

[10] R. Kyle, F. Wang, and B. Forbes. The effect of a leading edge erosion shield on the aerodynamic performance of a wind turbine blade. *Wind Energy* **23** (2020), 953–966.

[11] R. S. Ehrmann, E. B. White, D. C. Maniaci, et al. Realistic leading-edge roughness effects on airfoil performance. *31st AIAA Applied Aerodynamics Conference* (2013), 1–19.

[12] S. Watson, A. Moro, V. Reis, et al. Future emerging technologies in the wind power sector: A European perspective. *Renewable and Sustainable Energy Reviews* **113** (2019), 109270.

[13] D. Eisenberg, S. Laustsen, and J. Stege. Wind turbine blade coating leading edge rain erosion model: Development and validation. *Wind Energy* **21** (2018), 942–951.

[14] M. Al-Hadad, K. K. McKee, and I. Howard. Vibration characteristic responses due to transient mass loading on wind turbine blades. *Engineering Failure Analysis* **102** (2019), 187–202.

[15] J. Sierra-Pérez, M. A. Torres-Arredondo, and A. Güemes. Damage and nonlinearities detection in wind turbine blades based on strain field pattern recognition. FBGs, OBR and strain gauges comparison. *Composite Structures* **135** (2016), 156–166.

[16] J. Tang, S. Soua, C. Mares, and T. H. Gan. An experimental study of acoustic emission methodology for in service condition monitoring of wind turbine blades. *Renewable Energy* **99** (2016), 170–179.

[17] A. Manohar, J. Tippmann, and F. Lanza di Scalea. Localization of defects in wind turbine blades and defect depth estimation using infrared thermography. *Sensors and Smart Structures Technologies for Civil, Mechanical, and Aerospace Systems 2012* **8345** (2012), 83451O.

[18] J. Talbot, Q. Wang, N. Brady, and R. Holden. Offshore wind turbine blades measurement using Coherent Laser Radar. *Measurement: Journal of the International Measurement Confederation* **79** (2016), 53–65.

[19] C. Traylor, M. DiPaola, D. J. Willis, and M. Inalpolat. A computational investigation of airfoil aeroacoustics for structural health monitoring of wind turbine blades. *Wind Energy* **23** (2020), 795–809.

[20] J. Solimine, C. Niezrecki, and M. Inalpolat. An experimental investigation into passive acoustic damage detection for structural health monitoring of wind turbine blades. *Structural Health Monitoring* **19** (2020), 1711–1725.

[21] C. Beale, C. Niezrecki, and M. Inalpolat. An adaptive wavelet packet denoising algorithm for enhanced active acoustic damage detection from wind turbine blades. *Mechanical Systems and Signal Processing* **142** (2020), 106754.

[22] C. Beale, D. J. Willis, C. Niezrecki, and M. Inalpolat. Passive acoustic damage detection of structural cavities using flow-induced acoustic excitations. *Structural Health Monitoring* **19** (2020), 751–764.

[23] C. Beale, M. Inalpolat, and C. Niezrecki. Active acoustic damage detection of structural cavities using internal acoustic excitations. *Structural Health Monitoring* **19** (2020), 48–65.

[24] V. Arora, Y. H. Wijnant, and A. De Boer. Acoustic-based damage detection method. *Applied Acoustics* **80** (2014), 23–27.

[25] M. H. Keegan, D. H. Nash, and M. M. Stack. On erosion issues associated with the leading edge of wind turbine blades. *Journal of Physics D: Applied Physics* **46** (2013).

[26] B. M. Fazenda and D. Comboni. Acoustic condition monitoring of wind turbines: Tip faults. *9th International Conference on Condition Monitoring and Machinery Failure Prevention Technologies 2012, CM 2012 and MFPT 2012* **1** (2012), 109–123.

[27] B. Chen, S. Yu, Y. Yu, and Y. Zhou. Acoustical damage detection of wind turbine blade using the improved incremental support vector data description. *Renewable Energy* **156** (2020), 548–557.

[28] C. Q. Zhang, Z. Y. Gao, Y. Y. Chen, et al. Locating and tracking sound sources on a horizontal axis wind turbine using a compact microphone array based on beamforming. *Applied Acoustics* **146** (2019), 295–309.

[29] T. H. Tu, F. C. Lo, C. C. Liao, C. F. Chung, and R. C. Chen. Using wind turbine noise to inspect blade damage through portable device. *INTER-NOISE 2019 MADRID - 48th International Congress and Exhibition on Noise Control Engineering* (2019), 1–5.

[30] Q. Ye, F. Avallone, D. Ragni, M. Choudhari, and D. Casalino. Effect of Surface Roughness Geometry on Boundary-Layer Transition and Far-Field Noise. *AIAA Journal* (2021), 1–13.

[31] F. L. dos Santos, N. A. Even, L. Botero, C. Venner, and L. D. de Santana. Influence of Surface Roughness Geometry on Trailing Edge Wall Pressure Fluctuations and Noise (2021), 1–15.

[32] S. Oerlemans, P. Sijtsma, and B. Méndez López. Location and quantification of noise sources on a wind turbine. *Journal of Sound and Vibration* **299** (2007), 869–883.

[33] H. Gill and S. Lee. Effect of 2D ice accretion on turbulent boundary layer and trailing-edge noise. *International Journal of Aeroacoustics* **21** (2022), 260–285.

[34] R. Z. Szasz, M. Ronnfors, and J. Revstedt. Influence of ice accretion on the noise generated by an airfoil section. *International Journal of Heat and Fluid Flow* **62** (2016), 83–92.

[35] C. K. Tam. Discrete tones of isolated airfoils. *Journal of the Acoustical Society of America* **55** (1974), 1173–1177.

[36] T. F. Brooks, D. S. Pope, and M. A. Marcolini. *Airfoil self-noise and prediction.* Vol. 1218. National Aeronautics and Space Administration, 1989.

[37] M. J. Kingan and J. R. Pearse. Laminar boundary layer instability noise produced by an aerofoil. *Journal of Sound and Vibration* **322** (2009), 808–828.

[38] M. Kobayashi, M. Asai, and A. Inasawa. Experimental investigation of sound generation by a protuberance in a laminar boundary layer. *Physics of Fluids* **26** (2014).

[39] Q. Ye, F. Avallone, D. Ragni, M. Choudhari, and D. Casalino. Effect of surface roughness on boundary layer transition and far field noise. *25th AIAA/CEAS Aeroacoustics Conference, 2019* (2019).

[40] W. S. Saric, R. B. Carrillo, and M. S. Reibert. Leading-edge roughness as a transition control mechanism. *36th AIAA Aerospace Sciences Meeting and Exhibit* (1998).

[41] M. F. Kerho and M. B. Bragg. Airfoil boundary-layer development and transition with large leading-edge roughness. *AIAA Journal* **35** (1997), 75–84.

[42] D. Kim, G. S. Lee, and C. Cheong. Inflow broadband noise from an isolated symmetric airfoil interacting with incident turbulence. *Journal of Fluids and Structures* **55** (2015), 428–450.

[43] G.-S. Lee and C. Cheong. Frequency-domain prediction of broadband inflow noise radiating from a finite-thickness airfoil. *Journal of Wind Engineering and Industrial Aerodynamics* **213** (2021), 104618.

[44] S. Buck, S. Oerlemans, and S. Palo. Experimental characterization of turbulent inflow noise on a full-scale wind turbine. *Journal of Sound and Vibration* **385** (2016), 219–238.

[45] A. M. Faria, J. Y. Saab, S. Rodriguez, and M. de Mattos Pimenta. A rapid distortion theory-based airfoil turbulent inflow noise prediction method. *Journal of the Brazilian Society of Mechanical Sciences and Engineering* **42** (2020), 1–9.

[46] R. K. Amiet. Acoustic radiation from an airfoil in a turbulent stream. *Journal of Sound and Vibration* **41** (1975), 407–420.

[47] R. Paterson and R. Amiet. Acoustic radiation and surface pressure characteristics of an airfoil due to incident turbulence. *3rd Aeroacoustics Conference* (1976).

[48] S. Oerlemans and P. Migliore. Aeroacoustic wind tunnel tests of wind turbine airfoils. *Collection of Technical Papers - 10th AIAA/CEAS Aeroacoustics Conference* **3** (2004), 2758–2775.

[49] S. Zhong, X. Zhang, B. Peng, and X. Huang. An analytical correction to Amiet's solution of airfoil leading-edge noise in non-uniform mean flows. *Journal of Fluid Mechanics* **882** (2020), A291–A2932.

[50] J. K. Staubs. Real Airfoil Effects on Leading Edge Noise (2008), 1–328.

[51] J. Gill, X. Zhang, and P. Joseph. Symmetric airfoil geometry effects on leading edge noise. *The Journal of the Acoustical Society of America* **134** (2013), 2669–2680.

[52] R. Merino-Martínez, A. Rubio Carpio, L. T. Lima Pereira, et al. Aeroacoustic design and characterization of the 3D-printed, open-jet, anechoic wind tunnel of Delft University of Technology. *Applied Acoustics* **170** (2020).

[53] Y. Zhang, F. Avallone, and S. Watson. Wind turbine blade trailing edge crack detection based on airfoil aerodynamic noise: An experimental study. *Applied Acoustics* **191** (2022), 108668.

[54] W. A. Timmer and R. P. Van Rooij. Summary of the Delft University wind turbine dedicated airfoils. *Journal of Solar Energy Engineering, Transactions of the ASME* **125** (2003), 488–496.

[55] B. Moghadassian and A. Sharma. Designing wind turbine rotor blades to enhance energy capture in turbine arrays. *Renewable Energy* **148** (2020), 651–664.

[56] L. A. Joseph, A. Borgoltz, and W. Devenport. Infrared thermography for detection of laminar-turbulent transition in low—speed wind tunnel testing. *Experiments in Fluids* **57** (2016), 1–13.

[57] M. Drela. "XFOIL: An analysis and design system for low Reynolds number airfoils". In: *Low Reynolds number aerodynamics*. Springer, 1989, pp. 1–12.

[58] S. Oerlemans and B. M. López. Acoustic array measurements on a full scale wind turbine. *Collection of Technical Papers - 11th AIAA/CEAS Aeroacoustics Conference* **3** (2005), 2067–2075.

[59] P. Sijtsma. Phased Array Beamforming Applied to Wind Tunnel and Fly-Over Tests. *SAE Technical Papers* **2010-Octob** (2010), 17–19.

[60] P. Sijtsma, R. Merino-Martinez, A. M. Malgoezar, and M. Snellen. High-resolution CLEAN-SC: Theory and experimental validation. *International Journal of Aeroacoustics* **16** (2017), 274–298.

[61] R. Merino-Martínez, P. Sijtsma, M. Snellen, et al. *A review of acoustic imaging methods using phased microphone arrays: Part of the "Aircraft Noise Generation and Assessment" Special Issue*. Vol. 10. Springer Vienna, 2019, pp. 197–230.

[62] C. J. Bahr and W. C. Horne. Advanced background subtraction applied to aeroacoustic wind tunnel testing. *21st AIAA/CEAS Aeroacoustics Conference* (2015).

[63] P. Sijtsma and M. Snellen. Inverse integration method for distributed sound sources. *BeBeC* (2018), 9–17.

[64] S. Oerlemans. Detection of aeroacoustic sound sources on aircraft and wind turbines (2009), 1–173.

[65] J. Serpieri and M. Kotsonis. Flow visualization of swept wing boundary layer transition. *10th Pacific Symposium on Flow Visualization and Image Processing* (2015), 15–18.

[66] M. Serdar, l. Karasu, H. Hakan, and M. Turul. Low Reynolds Number Flows and Transition. *Low Reynolds Number Aerodynamics and Transition* (2012).

[67] S. Sudhakar, N. Karthikeyan, and P. Suriyanarayanan. Experimental studies on the effect of leading-edge tubercles on laminar separation bubble. *AIAA Journal* **57** (2019), 5197–5207.

[68] R. Patterson, P. Vogt, M. Fink, and G. Munch. Vortex noise of isolated airfoils (1972).

[69] H. Arbey and J. Bataille. Noise generated by airfoil profiles placed in a uniform laminar flow. *Journal of Fluid Mechanics* **134** (1983), 33–47.

[70] G. Desquesnes, M. Terracol, and P. Sagaut. Numerical investigation of the tone noise mechanism over laminar airfoils. *Journal of Fluid Mechanics* **591** (2007), 155–182.

[71] T. P. Chong and P. Joseph. "Ladder" structure in tonal noise generated by laminar flow around an airfoil. *The Journal of the Acoustical Society of America* **131** (2012), EL461–EL467.

[72] S. Pröbsting and S. Yarusevych. Laminar separation bubble development on an airfoil emitting tonal noise. *Journal of Fluid Mechanics* **780** (2015), 167–191.

[73] S. Pröbsting and S. Yarusevych. Airfoil flow receptivity to simulated tonal noise emissions. *Physics of Fluids* **33** (2021).

[74] T. Abo, A. Inasawa, and M. Asai. Experimental study on the feedback-loop mechanism generating tonal protuberance noise in boundary layers. *European Journal of Mechanics, B/Fluids* **85** (2021), 46–57.

[75] A. V. Dovgal, V. V. Kozlov, and A. Michalke. Laminar boundary layer separation: Instability and associated phenomena. *Progress in Aerospace Sciences* **30** (1994), 61–94.

[76] P. D. Lysakn, D. E. Capone, and M. L. Jonson. Prediction of high frequency gust response with airfoil thickness effects. *Journal of Fluids and Structures* **39** (2013), 258–274.

[77] S. Kim, D. E. Adams, H. Sohn, et al. Crack detection technique for operating wind turbine blades using Vibro-Acoustic Modulation. *Structural Health Monitoring* **13** (2014), 660–670.

[78] M. Lighthill. On Sound Generated Aerodynamically . II . Turbulence as a Source of Sound. *Proceedings of the Royal Society of London A, Mathematical and Physical Sciences* **222** (1953), 1–32.

[79] J. E. Ffowcs Williams and D. L. Hawkings. Sound generation by turbulence and surfaces in arbitrary motion. *Philosophical Transactions of the Royal Society of London. Serie A, Mathematical and Physical Sciences* **264** (1969), 321–342.

6

CONCLUSIONS AND OUTLOOK

This chapter summarizes the main findings of this thesis. Based on the analyses of the limitations of the present work, the outlook for the next step of work is presented to further advance and improve the proposed method. Finally, some recommendations for realistic applications are provided.

6.1. CONCLUSIONS

This thesis aims to develop and advance a new non-contact approach for wind turbine blade damage detection based on far-field aerodynamic noise measurements. To assess the feasibility of the proposed approach and investigate the physics of the noise generation mechanism, the experiments for trailing edge crack detection and leading edge erosion detection were carried out in the anechoic wind tunnel, as reported in the previous chapters. The research objectives were presented at the end of Chapter 1. With respect to each research objective, the main findings are summarized as follows:

1. **To identify the spectral differences in the sound generated by a damaged blade and by a healthy one.**

   Spectral differences can be seen in the sound generated by a damaged airfoil model and a healthy baseline case, which suggests the possibility of using aerodynamic noise information for blade damage detection, more specifically:

   (a) For trailing edge crack detection

   When a crack forms at the trailing edge of an airfoil, the thickness of the trailing edge increases. When the damage reaches a certain level, a tonal component can be observed in trailing edge noise, which is located around a trailing-edge-thickness-based Strouhal number, $St_h \sim 0.1$. Furthermore, with an increase in damage size, the tone shifts to a higher value of St_h and the intensity of the tone becomes stronger. In the presence of turbulent inflow or with an increase in angle of attack, the tonal peak tends to shift to a higher value of St_h. (Chapter 3)

   (b) For leading edge erosion detection

   For clean inflow conditions, the trailing edge noise does not show any significant difference between the baseline and minor erosion damage case, where the spectra show laminar instability noise features. As the damage increases to a moderate level, trailing edge noise on the pressure side changes with broadband characteristics; while that on the suction side still has tonal characteristics but the tones shift to higher frequencies. (Chapter 5)

   When the inflow is turbulent, the trailing edge noise spectra of all the tested cases with damage or baseline are broadband, and the differences between them cannot be distinguished, which suggests that trailing edge noise information is not enough for leading edge erosion detection under this condition. When looking at the leading edge noise spectra, as the damage level increases, the medium and high-frequency content decreases. The spectra of the sound pressure level relative to the baseline case, ΔL_p, are centered at a chord-length-based Strouhal number $St_C \sim 10$. (Chapter 5)

2. **To investigate the physics of change in blade noise in the presence of damage.**

   (a) For trailing edge crack detection

   As the crack size increases, the velocity gradient in the boundary layer at the trailing edge increases. This leads to coherent vortex structures with smaller relative

length scales and lower intensity, finally, making the crack-induced tone shift to higher values of St_h. (Chapter 4)

(b) For leading edge erosion detection

For clean inflow conditions, changes in the trailing edge noise spectrum in the presence of damage are mainly attributed to the changes in the transition process of the flow. For a moderate erosion case, as the damaged area on the pressure side is larger than that on the suction side, the boundary layer on the pressure side has already become turbulent at the trailing edge thus providing broadband turbulence noise features; on the suction side, the erosion alters the start-point of boundary layer transition and the size of the separation bubble in the boundary layer, causing a different acoustic feedback loop and a frequency shift of the tones. (Chapter 5)

When the inflow is turbulent, with respect to the non-damaged case, the decay of medium and high-frequency content in the leading edge noise spectra results from the larger stagnation region in front of the leading edge causing a larger distortion of the incoming turbulent eddies. (Chapter 5)

3. **To investigate how the operating conditions, such as inflow turbulence, velocity, and angle of attack, affect the noise spectra and damage detection.**

   (a) For trailing edge crack detection

   An increase in the velocity leads to a decrease in the displacement thickness of the boundary layer at the trailing edge (greater velocity gradient), thus slightly shifting the crack-induced tone to a higher value of St_h with a higher intensity. An increase in the angle of attack increases the average displacement thickness of the suction side and pressure side decreasing the amplitudes of tone, which affects the identification for a crack. An increase in turbulence intensity leads to a decrease in the length scale and the intensity of the coherent vortex structures. As a result, the crack-induced tone shifts to a higher St_h with lower amplitude. (Chapter 3 and 4)

   (b) For leading edge erosion detection

   For turbulent inflow conditions, increases in velocity and angle of attack do not seem to affect the relative spectral features induced by the erosion with respect to the baseline: the spectral peaks of the relative sound pressure level, ΔL_p, are located at almost the same St_C with equivalent amplitude. (Chapter 5)

4. **To determine the aerodynamic and aeroacoustic parameters that can be used for damage prediction.**

   For trailing edge crack detection, the located St_h of the crack-induced tone is associated with the ratio of the trailing edge thickness and the displacement thickness of the trailing edge, h/δ^*. The distribution of the tones from the measurements presented in this thesis agrees well with the trend of the semi-empirical model reported in [1]. In turn, for a real-world application, the semi-empirical model can be used to detect and predict the damage levels once the boundary layer displacement thickness and the frequency of the tone are known from the measurements. When the inflow is turbulent, the tonal peaks tend to shift to higher values, which

suggests an additional term regarding the turbulent inflow should be considered when using the suggested model for damage level prediction. (Chapter 4)

6.2. OUTLOOK

6.2.1. OUTLOOK FOR FUTURE WORK

This thesis presents an investigation of a new non-contact approach for blade damage detection at the airfoil level based on preliminary experiments and fundamental analyses. However, some important and key research questions still need to be looked into in the future for eventual application in wind turbine blade maintenance. This section provides a brief outlook for future work and recommendations for real-world applications.

DEVELOPMENTS FOR DAMAGE PREDICTION MODELS

In this thesis, the effects of the inflow turbulence on trailing edge crack detection have been investigated. The turbulent inflow shifts the tonal peaks to higher St_h. Since in this thesis, only two turbulence-generating grids were made which provided two turbulence intensity levels, the data is not enough to formulate semi-empirical models with an additional term considering the turbulence. In the future, it is suggested to create more turbulence intensity levels for the test conditions. By analyzing the variation under a wider range of turbulent conditions, a correction term considering turbulent inflow could be derived for the current model [1].

Aside from the geometry of the leading edge and the thickness of the airfoil, the frequency of leading edge impingement noise is also associated with the length scales of the inflow turbulence [2, 3]. This suggests that for an accurate estimation of the leading erosion size using leading edge noise information, the length scale of the inflow turbulence is needed. Furthermore, the relationship between the spectral differences in leading edge noise compared with the baseline and the ratio of inflow turbulence length scale to erosion size is worth investigation.

VALIDATION FOR ROTATIONAL SYSTEMS

Since the present work of this thesis is at a very early stage, the experiments were carried out using 2-D airfoil models. However, theoretically, the noise source generation mechanisms do not change when the blade is rotating [4]. As a matter of fact, many analytic formulations on full-scale wind turbine noise prediction are based on experiments carried out on 2-D airfoils by simply accounting for the corrections of the Doppler effect and directivity terms for rotating blades [1, 5–7]. When the blade is rotating, the resultant velocity that a blade section encounters is often higher (in particular the outer part of the blade), therefore, with a higher Reynolds number, than that in a 2D airfoil test. This will consequently lead to a higher level of turbulence in the boundary layer and an increase in turbulent noise, which possibly hides the spectral features induced by damage. Furthermore, for a 3D rotating wind turbine rotor, tip noise will be introduced. So in order to investigate if these factors can affect damage detection, the validation of the proposed method in this thesis for rotational systems is required.

To this end, a preliminary experimental investigation for a small wind turbine has been carried out in the Open Jet Facility (OJF) wind tunnel at Delft University of Technology. The wind turbine has a two-blade rotor with a diameter of 2 m, of which the

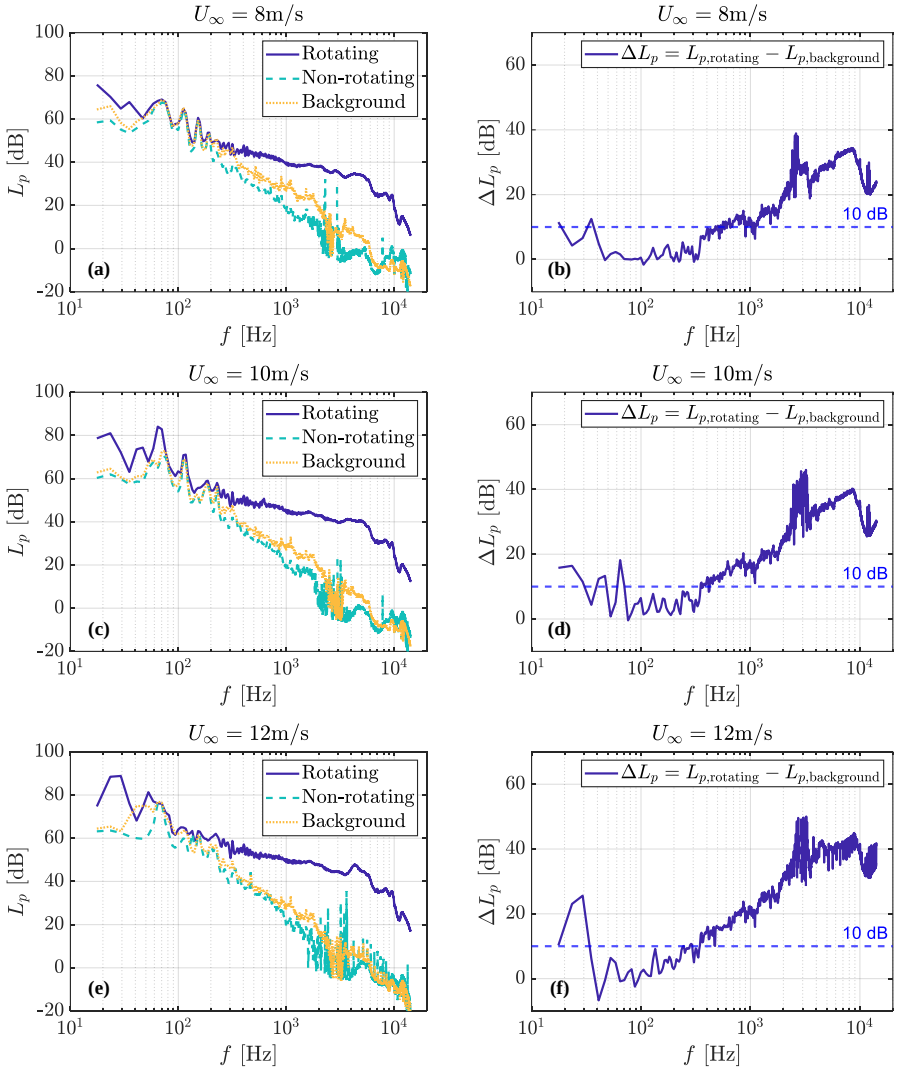

Figure 6.1: Sound pressure level, ΔL_p with the rotor rotating, stopped, and removed (background noise) and relative sound pressure level, ΔL_p, relative to the background noise, under different inflow velocities.

average chord length of the blade (DU96 W180 airfoil profile) is around 15 cm [8, 9]. The rotor worked at an optimal tip speed ratio, $\lambda_{\text{opt}} = 7$. A commercial microphone array with 112 microphones (Bionic M-112 microphone array, with a sampling frequency of 48 kHz) was used for noise measurements. The microphone array was placed on the ground in front facing the center of the rotor. For each measurement, the acoustic data were recorded for 30 s for further processing by Conventional Time Domain Beamforming (CTDBF) [10] and Rotational Sources Identifier (ROSI) [11].

Figure 6.1 shows the spectra of sound pressure level, L_p with the rotor rotating, stopped, and removed (background noise) and relative sound pressure level, ΔL_p, between the rotor rotating and removed, for different inflow velocities at 8, 10 and 12 m/s (with chord-length-based Reynolds numbers at a level of $Re_C \sim 5 \times 10^5$ for the blade tip section). The spectra of sound pressure level were calculated from the beamforming maps integrated within a circlar region swept by the rotor. The results show that when it is above 400 Hz, the relative sound pressure level of the rotor compared to the background noise is higher than 10 dB, which suggests the possibility of using the OJF wind tunnel for aeroacoustic measurements. The validation of the proposed method in this thesis for a rotating system can be performed in an OJF wind tunnel in the future.

6.2.2. RECOMMENDATIONS FOR APPLICATION

As was addressed previously, a good foundation for damage detection, especially for damage level estimation, requires additional aerodynamic information, such as inflow turbulence parameters, boundary layer properties, and information concerning flow transition over the blade surface. This suggests successful implementation of the proposed method, to some extent, needs to be combined with other instrumental devices measuring additional parameters for accurate damage identification.

Since the spatial resolution of a microphone array reduces as the distance between the rotor and the microphone array increases, the microphone array is better to be put as close as possible to the rotor. Furthermore, because of the limited spatial resolution, the exact location of damage might be difficult to identify. This suggests for a real-world engineering application, the installation and arrangement of the damage detection system need to be carefully designed.

REFERENCES

[1] T. F. Brooks, D. S. Pope, and M. A. Marcolini. *Airfoil self-noise and prediction*. Vol. 1218. National Aeronautics and Space Administration, 1989.

[2] E. Dogan, R. E. Hanson, and B. Ganapathisubramani. Interactions of large-scale free-stream turbulence with turbulent boundary layers. *Journal of Fluid Mechanics* **802** (2016), 79–107.

[3] D. Kim, G. S. Lee, and C. Cheong. Inflow broadband noise from an isolated symmetric airfoil interacting with incident turbulence. *Journal of Fluids and Structures* **55** (2015), 428–450.

[4] J. E. Ffowcs Williams and D. L. Hawkings. Sound generation by turbulence and surfaces in arbitrary motion. *Philosophical Transactions of the Royal Society of London. Serie A, Mathematical and Physical Sciences* **264** (1969), 321–342.

[5] C. A. Echeverri-Londoño and A. E. González-Fernández. Model for the prediction of noise from wind turbines. *Revista Facultad de Ingenieria* **2018** (2018), 55–65.

[6] V. B. Nukala and S. P. Maddula. Influence of rotor solidity on trailing edge noise from wind turbine blades. *Advances in Aerodynamics* **2** (2020).

[7] W. Z. Shen, N. Yunakov, J. F. Cao, and W. J. Zhu. Development of a general sound source model for wind farm application. *Renewable Energy* **198** (2022), 380–388.

[8] B. Akay, D. Ragni, C. S. Ferreira, and G. J. W. V. Bussel. Investigation of the root flow in a Horizontal Axis. *Wind Energy* (2013), 1–20.

[9] I. Herraéz, B. Akay, G. J. Van Bussel, J. Peinke, and B. Stoevesandt. Detailed analysis of the blade root flow of a horizontal axis wind turbine. *Wind Energy Science* **1** (2016), 89–100.

[10] B. D. Van Veen and K. M. Buckley. Beamforming: A Versatile Approach to Spatial Filtering. *IEEE ASSP Magazine* **5** (1988), 4–24.

[11] P. Sijtsma, S. Oerlemans, and H. Holthusen. Location of rotating sources by phased array measurements. *7th AIAA/CEAS Aeroacoustics Conference and Exhibit* (2001).

APPENDICES

A.1. STATISTICS AND SIGNAL PROCESSING

This appendix presents the definitions of the basic statistical metrics and the fundamental calculations of signal processing used in this thesis. In the entire thesis, the signals are assumed statistically stationary, which means the statistical properties of the signal do not change over time; and the discrete signals are sampled in equally-spaced time. It should be noted that in this appendix, the definitions for statistics and signal processing are not presented with a rigidly precise nature in mathematics. Alternatively, the completeness of these definitions is confined to the realms of physics and engineering applications.

A.1.1. MEAN AND STANDARD DEVIATION

Considering a discrete signal (samples), x_n (n is the index of the sample point), which is measured with a length of N, the mean value is defined as:

$$\bar{x} = \frac{1}{N}\sum_{n=1}^{N} x_n \tag{A.1}$$

And the standard deviation is calculated as:

$$\sigma_x = \sqrt{\frac{1}{N}\sum_{n=1}^{N}(x_n - \bar{x})^2} \tag{A.2}$$

A.1.2. ROOT MEAN SQUARE

Assuming there is a continuous signal, $x(t)$, varies in time, t, and the signal is observed in a time interval $[t_1, t_2]$ (usually with sufficient length, i.e., $t_1 \to -\infty$ and $t_2 \to +\infty$), the root-mean-square value of this signal is defined as:

$$x' = \sqrt{\frac{1}{(t_2 - t_1)}\int_{t_1}^{t_2} [x(t)]^2 \,\mathrm{d}t} \tag{A.3}$$

For the discrete signal, x_n, the root-mean-square value is given as:

$$x' = \sqrt{\frac{1}{N}\sum_{n=1}^{N}(x_n)^2} \tag{A.4}$$

A.1.3. CORRELATION

The cross-correlation of the continuous signals $x(t)$ and $y(t)$, defined in the same domain as $x(t)$, is calculated as:

$$R_{xy}(\tau) = \int_{t_1}^{t_2} \overline{x(t)} y(t+\tau) \mathrm{d}t \tag{A.5}$$

where $\overline{x(t)}$ is the complex conjugate of $x(t)$ and τ is the time lag between the two signals. By replacing $y(t)$ with $x(t)$, auto-correlation of $x(t)$ can be calculated as:

$$R_{xx}(\tau) = \int_{t_1}^{t_2} \overline{x(t)} x(t+\tau) \mathrm{d}t \tag{A.6}$$

For the ergodic discrete signals, x_n and y_n (with same length and sampling frequency as x_n), the cross-correlation is calculated as:

$$R_{xy}(\tau) = \frac{1}{N} \sum_{n=1}^{N} \overline{x_n} y_{n+\tau} \tag{A.7}$$

Similarly, the auto-correlation for x_n is given as:

$$R_{xx}(\tau) = \frac{1}{N} \sum_{n=1}^{N} \overline{x_n} x_{n+\tau} \tag{A.8}$$

A.1.4. FOURIER TRANSFORM AND POWER SPECTRAL DENSITY

For the continuous signal, $x(t)$, Fourier transform is calculated as:

$$X(f) = \int_{t_1}^{t_2} x(t) e^{-2\pi \mathrm{i} f t} \mathrm{d}t \tag{A.9}$$

where i is imaginary unit, $\mathrm{i} = \sqrt{-1}$; and $f \in (-\infty, +\infty)$ is the frequency. The time domain signal is converted to the representation in the frequency domain, $X(f)$, with phase information. The Power Spectral Density (PSD) is calculated as:

$$S'_{xx}(f) = X(f)\overline{X(f)} \tag{A.10}$$

In the real world, negative frequency does not have physical significance, so the two-side PSD is usually converted to one-side:

$$S_{xx}(f) = 2X(f)\overline{X(f)} \tag{A.11}$$

In practice, for the discrete signal, x_n, Discrete Fourier Transform (DFT) is applied:

$$X_k = \sum_{n=1}^{N} x_n e^{-2\pi \mathrm{i} \frac{k}{N} n} \tag{A.12}$$

where $k \in [0, N-1]$ is the frequency index. The corresponding frequency can be calculated as:

$$f = f_S \frac{k}{N} \tag{A.13}$$

where f_S is the sampling frequency. Therefore, the frequency resolution is:

$$\Delta f = \frac{f_S}{N} \tag{A.14}$$

The two-side PSD can be calculated as:

$$S'_{xx}(k) = \frac{X_k \overline{X_k}}{N f_S} \tag{A.15}$$

The one-side PSD can be determined by doubling one-side of $S'_{xx}(k)$, for non-zero frequency components, i.e.,

$$S_{xx}(k) = \frac{2X_k \overline{X_k}}{N f_S} \tag{A.16}$$

where $k \in [1, N/2-1]$ (if N is even) or $k \in [1, (N-1)/2]$ (if N is odd).

To mitigate energy leakage, a window function, w_n (with the same length with x_n), is usually applied to the sampled signal x_n, thus the DFT becomes,

$$X_k = \sum_{n=1}^{N} x_n w_n e^{-2\pi \mathrm{i} \frac{k}{N} n} \tag{A.17}$$

In this case, the PSD is corrected as:

$$S_{xx}(k) = \frac{2X_k \overline{X_k}}{W f_S} \tag{A.18}$$

where

$$W = \sum_{n=1}^{N} w_n \tag{A.19}$$

For the original DFT, there is essentially a rectangular window applied to the signal, i.e., $w_n = 1$ and $W = N$. In this thesis, a Hanning window is used, which is given as:

$$w_n = 0.5\left(1 - \cos\frac{2\pi n}{N}\right) \tag{A.20}$$

An example of a hann window applied to a sine signal is shown in Figure A.1.

A.1.5. SOUND METRICS

Sound pressure level (SPL), L_p, is used in the thesis to describe the noise spectrum, which can be calculated from PSD:

$$L_p(f) = 10\log\left(\frac{S_{pp}(k)\Delta f}{p_0^2}\right) \tag{A.21}$$

where S_{pp} is the PSD of measured sound pressure signal; k is the index corresponding to the frequency f; p_0 is the reference pressure, $p_0 = 2 \times 10^{-5}$ Pa. Overall sound pressure level (OSPL) is used to quantify the overall sound level integrated within a given frequency band $[f_1, f_2]$,

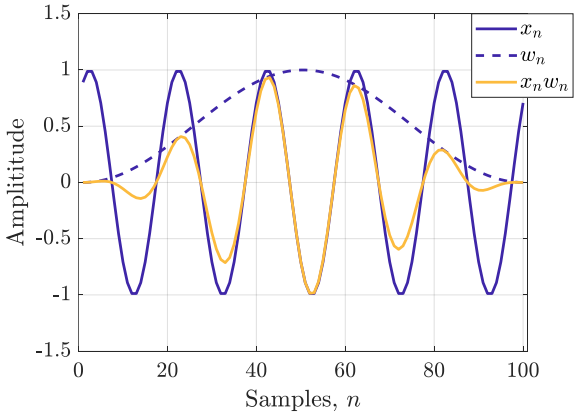

Figure A.1: A Hanning window applied to a sine signal.

$$\text{OSPL} = 10\log\left(\frac{\sum_{n=k_1}^{k_2} S_{pp}(n)\Delta f}{p_0^2}\right) \tag{A.22}$$

where index interval $[k_1, k_2]$ corresponds to the frequency band $[f_1, f_2]$. In this thesis, the sound pressure level of beamforming maps is given in one-third octave band:

$$L_{p,1/3} = 10\log\left(\frac{\sum_{n=k_{1,1/3}}^{k_{2,1/3}} S_{pp}(n)\Delta f}{p_0^2}\right) \tag{A.23}$$

where index interval $[k_{1,1/3}, k_{2,1/3}]$ corresponds to the frequency band $[f_{1,1/3}, f_{2,1/3}]$ of the center frequency, $f_{1/3}$. Table A.1 shows the one-third octave band from 20 Hz to 20 kHz.

Table A.1: One-third octave band from 20 Hz to 20 kHz.

Band No.	14	15	16	17	18	19	20	21	22	23
$f_{1/3}$	25	31.5	40	50	63	80	100	125	160	200
$f_{1,1/3}$	22	28	35	44	57	71	88	113	141	176
$f_{2,1/3}$	28	35	44	57	71	88	113	141	176	225

Band No.	24	25	26	27	28	29	30	31	32	33
$f_{1/3}$	250	315	400	500	630	800	1000	1250	1600	2000
$f_{1,1/3}$	225	283	353	440	565	707	880	1130	1414	1760
$f_{2,1/3}$	283	353	440	565	707	880	1130	1414	1760	2250

Band No.	34	35	36	37	38	39	40	41	42	43
$f_{1/3}$	2500	3150	4000	5000	6300	8000	10000	12500	16000	20000
$f_{1,1/3}$	2250	2825	3530	4400	5650	7070	8800	11300	14140	17600
$f_{2,1/3}$	2825	3530	4400	5650	7070	8800	11300	14140	17600	22500

A.2. COORDINATES OF THE MICROPHONE ARRAY

The positions of the microphones on the microphone array (on xoz plane, taken No. 41 as the reference) are shown in Table A.2.

Table A.2: Coordinates of microphone array.

No.	Position (x, z)	No.	Position (x, z)	No.	Position (x, z)	No.	Position (x, z)
1	(-0.525, -0.030)	17	(0.525, -0.030)	33	(-0.240, -0.120)	49	(-0.120, 0.180)
2	(-0.660, 0.030)	18	(0.630, 0.120)	34	(-0.345, -0.195)	50	(-0.195, 0.270)
3	(-0.720, -0.120)	19	(0.615, -0.105)	35	(-0.135, -0.315)	51	(-0.465, 0.150)
4	(-0.720, 0.135)	20	(0.765, 0.030)	36	(-0.525, -0.195)	52	(-0.495, 0.240)
5	(-0.075, -0.420)	21	(0.795, 0.210)	37	(-0.360, -0.330)	53	(-0.405, 0.345)
6	(-0.870, -0.030)	22	(0.855, -0.105)	38	(-0.615, -0.300)	54	(-0.720, 0.270)
7	(-0.810, -0.240)	23	(0.930, 0.105)	39	(0.345, -0.435)	55	(-0.225, 0.435)
8	(-0.945, 0.090)	24	(0.840, -0.210)	40	(-0.300, -0.435)	56	(-0.630, 0.375)
9	(0.240, -0.120)	25	(0.150, 0.105)	41	(0, 0) (Reference)	57	(0.180, 0.270)
10	(0.000, -0.165)	26	(0.240, 0.030)	42	(0, 0.135)	58	(-0.090, 0.345)
11	(0.360, -0.195)	27	(0.210, -0.045)	43	(-0.075, -0.105)	59	(0.345, 0.300)
12	(0.015, -0.255)	28	(0.075, -0.105)	44	(-0.210, -0.045)	60	(0.120, 0.390)
13	(0.315, -0.285)	29	(0.120, 0.180)	45	(-0.240, 0.030)	61	(0.570, 0.270)
14	(0.600, -0.225)	30	(0.315, 0.105)	46	(-0.150, 0.105)	62	(0.375, 0.420)
15	(0.150, -0.360)	31	(0.360, -0.015)	47	(-0.360, -0.015)	63	(0.600, 0.390)
16	(0.510, -0.345)	32	(0.465, 0.150)	48	(-0.315, 0.105)	64	(-0.015, 0.495)

A.3. DETAILS OF AIRFOIL MODELS

A.3.1. SIDE VIEW OF TRAILING EDGE INSERTS WITH CRACK

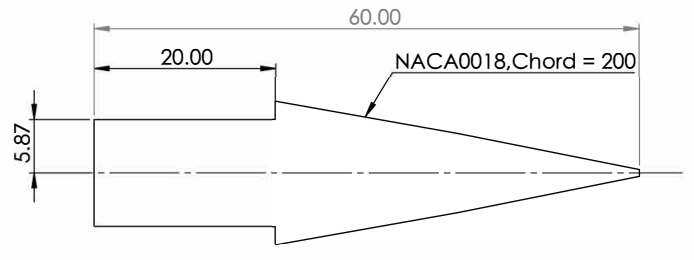

Base line

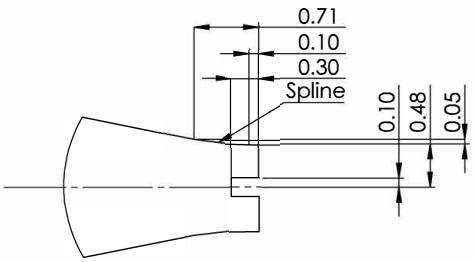

DETAIL A
SCALE 20 : 1

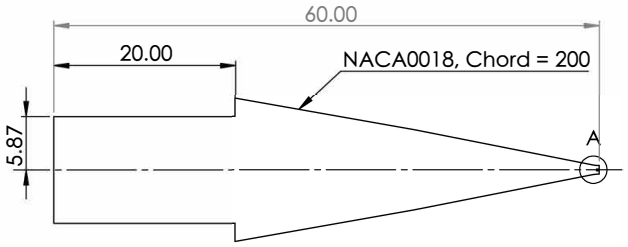

Damage level 1

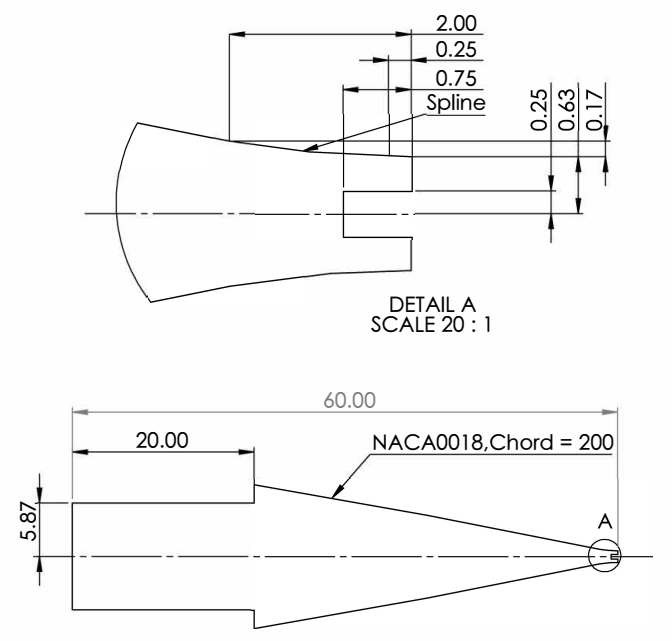

Damage level 2

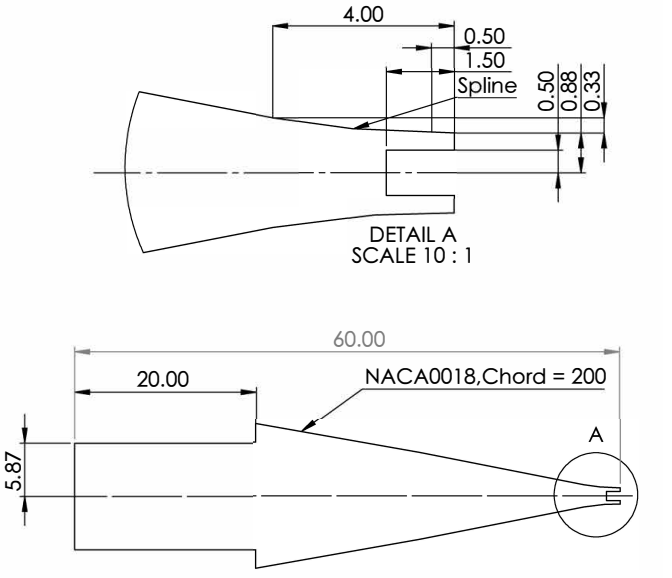

Damage level 3

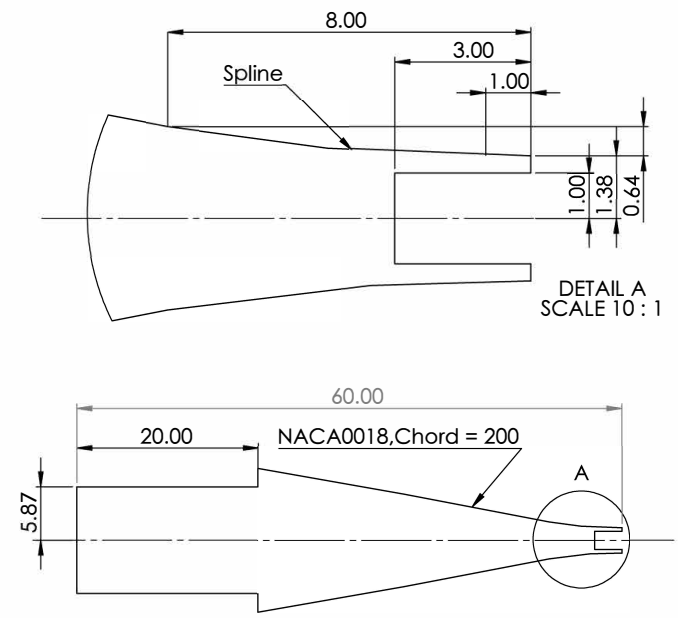

Damage level 4

A.3.2. SIDE AND TOP VIEWS OF LEADING EDGE INSERTS WITH EROSION

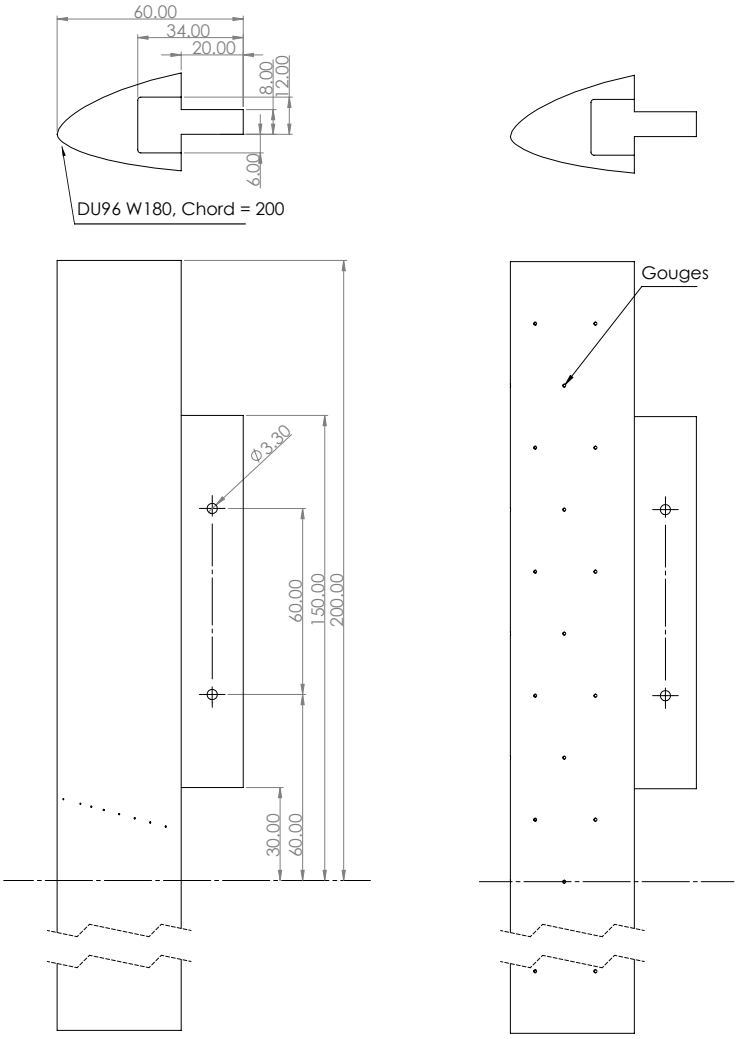

Baseline

Damage level 1

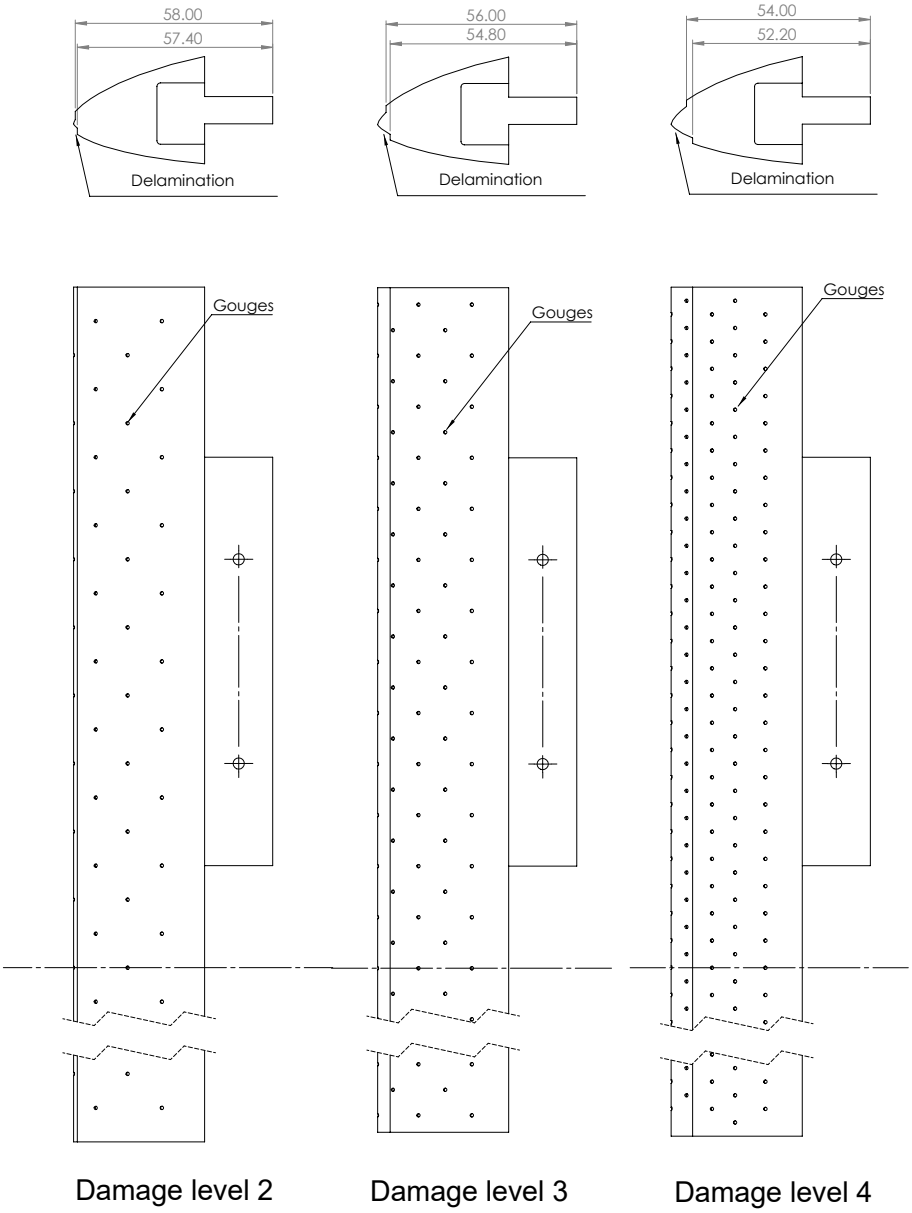
58.00
57.40
Delamination
56.00
54.80
Delamination
54.00
52.20
Delamination
Gouges
Gouges
Gouges
Damage level 2
Damage level 3
Damage level 4

A.3.3. COORDINATES OF PRESSURE TAPS

The coordinates of pressure taps for the airfoil models NACA 0018 and DU96 W180 are shown in Tables A.3 and A.4, respectively.

Table A.3: Pressure taps for NACA 0018 airfoil.

No.	1	2	3	4	5	6	7	8	9	10	11	12	13	14	15
X/C	-0.99	-0.965	-0.94	-0.89	-0.84	-0.79	-0.74	-0.69	-0.64	-0.59	-0.54	-0.49	-0.44	-0.39	-0.37

Table A.4: Pressure taps for DU96 W180 airfoil.

No.	1	2	3	4	5	6	7	8	9	10	11	12	13	14	15	16
X/C	-0.99	-0.9625	-0.945	-0.925	-0.9	-0.875	-0.85	-0.775	-0.7	-0.6	-0.5	-0.4	-0.325	-0.275	-0.225	-0.175

ACKNOWLEDGEMENTS

It is finally time to write the acknowledgments, which means I will close my PhD chapter very soon. Before I even thought about how to structure and write this thesis, I started thinking about how fancy my acknowledgments should be. However, I still do not know how to translate my thoughts into words now. The journey of life always seems to be like this: one may always look forward to doing something big, only to eventually accept that they are just an ordinary person among all living beings. There are many four years in my life but I think these four years of my PhD will be the most unique ones for me because they are also the time when I really grow mature. I am grateful for the gains in my PhD journey and the people who helped me during these four years.

Firstly, I would like to express my heartfelt thanks to my promotors, **Prof. Simon Watson** and **Prof. Francesco Avallone**. **Prof. Watson**, thank you for accepting me as a PhD student here and for your support in applying for the scholarship when I contacted you in the last year of my Master's study. I would say I was so lucky to join in Wind Energy Section, where I could carry out my PhD project with solid knowledge support in wind turbine condition monitoring and aeroacoustics fields. I appreciate your supervision styles and you always made the discussion with you enjoyable. You provided me with very much freedom in research and you were so kind and patient in discussing any possibilities I proposed though some of them might be imaginative and even stupid. **Francesco**, as my daily supervisor, thank you for providing me the dedicated and conscientious guidance for my PhD work and teaching me how to be an excellent researcher. You were strict and prudential with the research and always helped me figure out the reasons that led to the errors and then improve and solve them in proper ways. You were always on call when I had problems though you moved to Turin later and you even worked on weekends to revise the papers and reports. Without your contributions, I would not have gone so smoothly for my PhD work.

Special acknowledgments should be shown to my colleagues who worked closely with my PhD project. **Dani**, thank you always here for giving me a hand with the experiments and discussions for the experimental results, in particular when Francesco was not here; thank you for the daily management for the aeroacoustics group so that we can have an excellent environment working efficiently and accessing the resources freely. **Salil** and **Alejandro**, thank you for showing me how to perform the experiments in A-tunnel and sharing your CAD drawings for the airfoils as references in the first year of my PhD so that I could start my project quickly. **Riccardo**, thank you for your suggestions on the turbulence-generating grid design and wind tunnel background noise removal, and thank you for your help with the experimental setup in OJF. **Roberto**, thank you for your help with the acoustic measurements in OJF and processing acoustic data. **Marios**, thank you for your suggestions on the measurements for boundary layer transition and for helping me with the surface oil flow visualization. **Kaisheng**, thank you for always helping me change the airfoils when I did experiments in the low speed lab.

Carlos, firstly, I should apologize for ruining your wind turbine during the test and thank you for comforting me after the thing happened.

I would like to thank the support staff. **Sylvia**, thank you for your help with our daily activities and paperwork and you were always helpful in providing useful suggestions and any information you know when I had questions. Thank you, the technician team, **Stefan** and **Emiel** from low speed lab and **Peter** (Duyndam), **Dennis**, **Frits** (Donker Duyvis) and **Henk-Jan** from high speed lab, for your help with mounting the test models and operating the wind tunnels. Thank you, **Peter** (den Dulk), **Ed** and **Steve** from the DEMO team, for your professional manufacture of airfoil models and turbulence-generating grids.

I would like to express my appreciation to those academic staff who might not be directly involved in my PhD project but I have learnt a lot from you. **Michiel**, I enjoyed your Master's courses and your teaching style, and thank you for your lecture notes that I often read as a reference book. **Damiano**, thank you (together with Francesco) for your fundamental aeroacoustics course, where I understood how aerodynamic noise was generated more profoundly. **Mirjam**, thank you for your courses about signal processing where I learned how the phased array works. **Wim**, thank you for your initiative of sharing daily life during the pandemic which made the home-working life more colorful. **Frits** (de Prenter), thank you for organizing the activities and regular meetings for the aeroacoustics group, and thank you for helping me check the Dutch version thesis summary and propositions. **Donatella**, you were always friendly and encouraging, and thank you for sharing your research on wind turbine condition monitoring during the cluster meetings. **Dominic**, thank you for sharing the Chinese novels you read.

I also greatly appreciate the friendships with the PhD and postdoc fellows. Special thanks to my roommates in 6.15, **Livia**, **Sharif**, **Hafiz**, **Abhratej** and **Evert** and former roommates, **Delphine**, **Chihoon**, **Claudia** and **Helena**. I really enjoyed the time we spent in the office, where we could freely share different cultures, our daily lives and weekend plans. Thank you, the (former) PhDs/postdocs in aeroacoustics group and wind energy systems cluster, **Tercio**, **Hugo**, **Fernanda**, **Jatinder**, **Andrea**, **Manoel**, **Christopher**, **Lucas**, **Mehtab**, **Ali**, **Daniele** (Fiscaletti), **Yan**, **Sen**, **Dachuan**, **Sumit**, ..., for the insightful conversations and discussions in different topics on many occasions. I would also want to express my thanks to the rest of (former) PhDs in the Wind Energy Section, **Jingna**, **Guanqun**, **Adhyanth**, **Flavio**, **Mihir**, **Kiran**, **David**, **Ming**, **Jing**, ..., for the interesting conversations during free time and coffee breaks. Special thanks to my PhD friends, **Wencan**, **Yifu**, **Xiang**, **Xiaodong**, **Dong** for the happy parties and around-Europe trips with you.

Finally, I would like to thank **Jiashang**. Your love, kindness, and support have been the driving force behind my happiness and personal growth. In addition, many thanks go to my family for your unfailing love and support.

Yanan Zhang
Delft, March 2024

CURRICULUM VITÆ

Yanan ZHANG

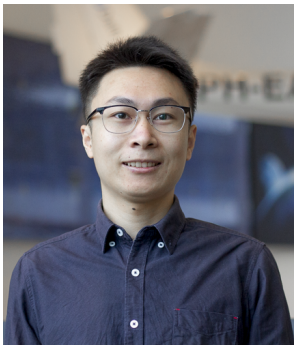

Yanan Zhang was born on December 1st 1993 in Shandong, China. Since Yanan was a child, he has shown great interest in physics and engineering. He liked to disassemble electrical appliances and toys to figure out how they worked (sometimes he made the whole house a mess and got blamed). He also liked to make some new gadgets with disassembled components, like a small electric ship and a pump-driven rocket, according to the knowledge he got from the science courses in school and the television. Due to the interest, he chose the major of sciences in the second year of high school.

In 2012, with the dream of being a scientist, Yanan entered Hohai University, Nanjing, China, for his Bachelor's degree in New Energy Science and Engineering (09/2012 – 06/2016). During this period he systematically studied the basic knowledge of wind energy. It was during this time that he first realized the critical significance of transitioning from conventional energy sources to sustainable and renewable alternatives. After his Bachelor's study, he went to Ocean University of China, Qingdao, China, for his Master's degree in Marine Mechanical and Electrical Equipment (09/2016 – 06/2019, first-level discipline in Control Science and Engineering). His area of study was signal and data processing and the development of instrumental devices. His Master's project involved a non-contact method for wind turbine blade damage detection using a single microphone and data-driven approaches, which was supervised by Prof. dr. Shengbo Qi.

Afterward, in 2019, Yanan got an opportunity to pursue his PhD (from 09/2019) at the Wind Energy Research Group of Delft University of Technology under the support of the Chinese Government Scholarship. Differently from his Master's project, the PhD project aimed to further investigate the possibility of using aerodynamic noise for wind turbine blade damage detection in a physics-based way. The project results in the outcomes of this thesis. His PhD work was supervised by Prof. dr. Simon Watson and Prof. dr. Francesco Avallone.

Additionally, Yanan likes playing table tennis and making seal carvings during his free time. However, he rarely engaged in these two hobbies since he came to the Netherlands. Now he enjoys going hiking, cycling and photography.

LIST OF PUBLICATIONS

JOURNAL PUBLICATIONS

3. **Y. Zhang**, S. Watson., D. Ragni, and F. Avallone, Towards the prediction of airfoil trailing edge crack size through aerodynamic noise measurements for both clean and turbulent inflow conditions. Submitted to *Journal of Sound and Vibration* (2023).

2. **Y. Zhang**, F. Avallone, and S. Watson. Leading edge erosion detection for a wind turbine blade using far-field aerodynamic noise. *Applied Acoustics* **207** (2023), p. 109365.

1. **Y. Zhang**, F. Avallone, and S. Watson. Wind turbine blade trailing edge crack detection based on airfoil aerodynamic noise: An experimental study. *Applied Acoustics* **191** (2022), p. 108668.

CONFERENCE CONTRIBUTIONS

3. **Y. Zhang**, F. Avallone, and S. Watson. Effect of airfoil trailing edge crack on aerodynamic noise under turbulent inflow conditions. *Wind Energy Science Conference (WESC 2023)*, May 2023, Glasgow, UK.

2. **Y. Zhang**, F. Avallone, and S. Watson. An aeroacoustics-based approach for wind turbine blade damage detection. *The Science of Making Torque from Wind Conference (TORQUE 2022)*, May 2022, Delft, the Netherlands. *Journal of Physics: Conference Series* **2265** (2022), p. 022088.

1. **Y. Zhang**, F. Avallone, and S. Watson. An experimental study on trailing edge crack detection for wind turbine blade using airfoil aerodynamic noise. *Wind Energy Science Conference (WESC 2021, online)*, May 2021, Hanover, Germany.

DATA REPOSITORY

2. **Y. Zhang**, F. Avallone, and S. Watson. Beamforming maps and noise spectra data of wind turbine blade leading edge erosion detection. *4TU.ResearchData*, 2023.

1. **Y. Zhang**, F. Avallone, and S. Watson. Beamforming maps and noise spectra data of wind turbine blade trailing edge crack detection. *4TU.ResearchData*, 2023.